Omnidirectional phase matching in zero-index media

By

Justin Gagnon

A master's thesis submitted to
the University of Ottawa
in partial fulfilment of the requirements for the MSc. degree of
MASTER OF SCIENCE in Physics

uOttawa

Under the supervision of Robert W. Boyd
Department of Physics
University of Ottawa
April 2021

ACKNOWLEDGMENTS

Fabrication in this work was performed in part at the Center for Nanoscale Systems (CNS). CNS is part of Harvard University. I acknowledge support from the Canada First Research Excellence Fund, the Canada Research Chairs Program, and the Natural Sciences and Engineering Research Council of Canada NSERC. Furthermore, I acknowledge the contributions of my co-authors in our publication of the material presented in this thesis "Relaxed phase-matching constraints in zero-index waveguides" [1]: Orad Reshef conceived the basic idea for this work. Myself, Orad Reshef, and Daniel H.G. Espinosa designed the experiment. Daryl I. Vulis and Eric Knall carried out the linear measurements establishing the refractive index profiles of the waveguides. Orad Reshef and Yang Li carried out the simulations of the refractive index profiles. Myself, Orad Reshef, Jeremy Upham, and Zahirul Alam analyzed the experimental results. Robert W. Boyd, Jeremy Upham, Eric Mazur, and Ksenia Dolgaleva supervised the research and the development of the manuscript.

Beyond work specifically contributed to this research, I must express my deepest gratitude to my advisor Dr. Robert Boyd for entrusting me with this amazing opportunity and guiding my along this journey which has helped me grow academically, professionally, and personally. Dr. Boyd has, without a doubt, made a great effort to create an amazing research environment that provides students with the atmosphere to attain their full potential. I must additionally express my sincerest thanks to Orad Reshef for making my Master's Degree a very enjoyable experience with his constant guidance. His patient, kind, and upbeat nature have without a doubt improved the atmosphere of the Boyd research group as a whole. I would also like to acknowledge the contributions of Jeremy Upham, Daniel Garcia-Espinosa, and Zahirul Alam whose knowledge and suggestions have helped me breach many obstacles I have encountered during my research. I would like to acknowledge all of my friends and colleagues: Naeemah, Sisira, Boris, Ryan, Sijyl, Yaryna, Theng Loo, Jeremy, Alex, Cheng, Maryam, Saad, Yaswant, Mohammad, Nicholas and more who have made my experience much more enjoyable, and made the Boyd group such a great working environment. Finally, I must thank my mother Lise, my father Eric, and my sister Bryanne for providing me either financial support through both my undergrad and my Master's degree, or unconditional moral support.

ABSTRACT

Since its inception, the field of nonlinear optics has only increased in importance as a result of a growing number of applications. The efficiency of all parametric nonlinear optical processes is limited by challenges associated with phase-matching requirements. To address this constraint, a variety of approaches, such as quasi-phase-matching, birefringent phase matching, and higher-order-mode phase matching have historically been used to phase-match interactions. However, the methods demonstrated to date suffer from the inconvenience of only being phase-matched for one specific arrangement of beams, typically co-propagating along the same axis. This stringency of the phase-matching requirement results in cumbersome optical configurations and large footprints for integrated devices. In this thesis, we show that phase-matching requirements in parametric nonlinear optical processes may be satisfied for all orientations of input and output beams when using zero-index media: a condition of omnidirectional phase matching. To validate this theory, we perform experimental demonstrations of phase matching for five separate FWM beam configurations to confirm this phenomenon. Our measurements constitute the first experimental observation of the simultaneous generation of a forward- and backward-propagating signal with respect to the pump beams in a medium longer than a free-space optical wavelength, allowing us to determine the coherence length of our four-wave-mixing process. Our demonstration includes nonlinear signal generation from spectrally distinct counter-propagating pump and probe beams, as well as the excitation of a parametric process with the probe beam's wave vector orthogonal to the wave vector of the pump beam. By sampling all of these beam configurations, our results explicitly demonstrate that the unique properties of zero-index media relax traditional phase-matching constraints, and provide strong experimental evidence for the existence of omnidirectional phase matching in zero-index media. This property can be exploited to facilitate nonlinear interactions and miniaturize nonlinear devices, and adds to the established exceptional properties of low-index materials.

Table of Contents

Page

List of Abbreviations and Symbols

List of Abbreviations

FWM	Four-wave mixing
SVAA	Slowly varying amplitude approximation
ENZ	Epsilon-near-zero
MNZ	Mu-near-zero
EMNZ	Epsilon-and-mu-near-zero
PBG	Photonic band gap
CW	Continuous-wave
OPO	Optical parametric oscillator
FWHM	Full-width half maximum
EDFA	Erbium-doped fiber amplifier
OSA	Optical spectrum analyzer

List of Constants

π	Pi	ϵ_0	Vacuum permittivity	μ_0	Vacuum permeability
η_0	Free-space impedance	c	Speed of light	i	Imaginary unit

List of Symbols

λ	Wavelength	k	Wave vector	n	Refractive index
ω	Angular frequency	$\mathbf{P}$	Polarization density	$\mathbf{E}$	Electric field
t	Time	ϵ	Relative permittivity	μ	Relative permeability
χ_e	Electric susceptibility	χ^n	nth-order susceptibility	$\mathbf{D}$	Elec. displacement field
$\mathbf{B}$	Magnetic induction field	$\mathbf{H}$	Magnetic intensity field	z	Distance
A	Amplitude	L	Length	L_{coh}	Coherence length
P	Pol. density / Power	v_p	Phase velocity	v_g	Group velocity
ϕ	Phase / Angle phi	θ	Angle theta	η	Impedance
R	Power reflection	ρ	xy wave vector	d	Thickness
a	Lattice spacing	r	Radius	β	Propagation constant
D	Dispersion parameter	α	Propagation loss	σ	Standard deviation

Chapter One
Introduction

Since the first proof of concept in 1960 [2], the laser has served innumerable applications in daily life. Many of the uses of lasers arise from the existence of nonlinear optics, an important field of physics describing the behavior of light in media that respond differently to light at distinct intensities. Perhaps the most well-known example of an application of nonlinear optics is the green laser pointer. Almost all green lasers use the nonlinear optical process of second-harmonic generation to convert otherwise invisible infrared light into intense, visible green light. Nonlinear optics occupies important roles in fields such as spectroscopy and microscopy, and has been crucial in the development of new laser sources, laser-material interactions, and the field of information technology [3, 4, 5, 6]. Nonlinear optics has additionally played a role in at least 9 Nobel Prizes in physics and chemistry [3].

In a parametric nonlinear optical interaction, there must be conservation of energy between the input and output light waves. Analogously, for a nonlinear optical interaction to be efficient, there must be conservation of momentum (or the wave vectors) between the input and output light waves. Phase mismatch is defined as the wave vector mismatch between the input and output light waves, and a nonlinear optical interaction is said to be phase-matched when the phase mismatch is equal to zero. The size of the phase mismatch is a quantity that governs the efficiency of all parametric nonlinear interactions: interactions that have no net transfer of energy, momentum, or angular momentum between the optical field and the physical system. It is therefore critical that phase matching be satisfied when using these nonlinear interactions, so that they may be optimally efficient. Achieving phase matching requires the careful selection of an optical medium with the correct dispersion characteristics, as well as the precise alignment of the constituent light waves. The challenges in satisfying these requirements impede new applications of nonlinear optics.

When a nonlinear interaction is phase-mismatched (i.e., possesses non-zero wave-vector mismatch), the difference in accumulated phase between the frequency components of the nonlinear interaction can build up as they propagate in a nonlinear medium. Eventually, this discrepancy leads to newly generated photons interfering destructively with the propagating beam. Consequently, in such interactions, a nonlinear wave can only be generated over the coherent buildup length, more simply known as the coherence length, where substantial destructive interference does not yet occur (Fig. 1.1). By contrast, in a nonlinear interaction with no phase mismatch, the signal wave amplitude may build up coherently with propagation distance. Achieving this coherent buildup of light without needing to compromise for the difficult-to-satisfy phase-matching requirement would facilitate many implementations of

nonlinear optics in modern science. For example, it would be possible to miniaturize devices making use of nonlinear optics in order to make them more convenient and commercially viable. An all-optical transistor, a device that would have to rely on nonlinear optical interactions, could greatly benefit from efficient nonlinear interactions and miniaturization [7, 8, 9].

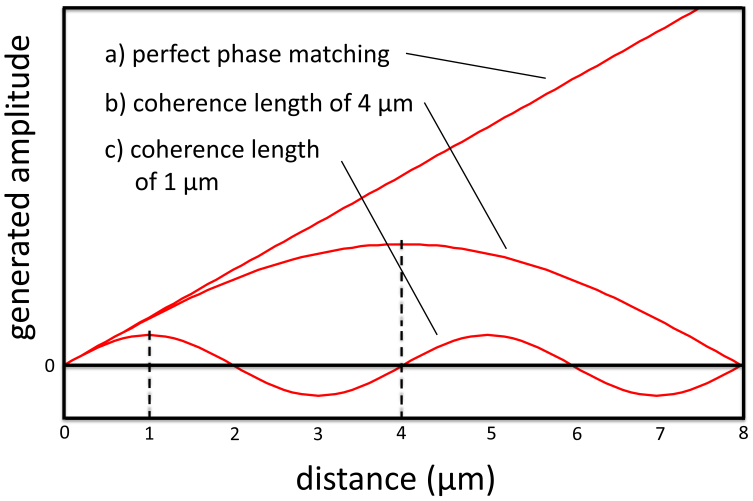

Figure 1.1 Amplitude of a generated nonlinear signal wave over distance propagated for different amounts of phase mismatch. In a), the interaction is perfectly phase-matched. In b), the coherence length is 4 µm, and in c), the coherence length is 1 µm. With perfect phase matching, the nonlinear signal wave builds up linearly. Otherwise, it builds up over a finite coherence length then reduces in amplitude.

1.1 Previous approaches to phase-matching

To tackle the phase-matching challenge and achieve the coherent buildup of light, a variety of approaches, such as quasi-phase-matching [10, 11], birefringent phase matching [12], and higher-order-mode phase matching [13, 14] have been developed. However, the methods demonstrated to date suffer from the inconvenience of only being phase-matched for one specific arrangement of beams, which is typically when they are co-propagating along the same axis. This means that when these methods are applied, the inevitable drawbacks are cumbersome optical configurations and large footprints for integrated devices [15].

Phase matching with non-conventional beam orientations has previously been investigated. In 2015, Lan *et al.* demonstrated the generation of a backward-propagating signal wave when using the nonlinear optical interaction of second-harmonic generation [16, 17, 18, 19]. To accomplish this, they used a negative-index metamaterial that exhibited a positive refractive index at the pump wavelength λ_p, and a negative refractive index equal in magnitude to the pump wave's index at the signal wavelength $\lambda_s = \lambda_p/2$. Due to the wave vector's dependence on the refractive index

$$k = \frac{2\pi n}{\lambda}, \tag{1.1}$$

where k is the wave vector, n is the refractive index, and λ is the wavelength, the phase difference for a backward-propagating signal wave, $\Delta k = 2k_p + k_s$, was equal to zero. Therefore, the interaction was perfectly phase-matched. Were the refractive index positive everywhere, phase matching a backward-propagating signal wave would not have been possible. However, phase-matching a backward-propagating signal wave in this manner means that a forward-propagating signal wave, whose phase mismatch is given by $\Delta k = k_p - 2k_s$, is not phase-matched.

In 2013, Suchowski *et al.* demonstrated the simultaneous generation of forward- and backward-propagating signal waves using the nonlinear optical interaction of four-wave mixing (FWM) [15]. To accomplish this, they used a zero-index fishnet metamaterial and placed the generated signal wave at a wavelength where the refractive index was zero. When $n = 0$, light has a vanishing wave vector $k = 0$, as per Eq. (1.1). This means that the sign in the phase mismatch dictated by the orientation of the signal wave becomes completely inconsequential to the value of the phase mismatch in this situation. As a result, the generated signal wave was free to be forward- or backward-propagating, without any directional restriction. This freedom in wave orientation eliminates one of the greatest restrictions of phase matching — the necessity for careful alignment and of a specific orientation for the input and output beams. However, while Suchowski *et al.* demonstrated the generation of forward- and backward-propagating idler beams for a particular arrangement of the pump and signal beams — co-propagation — they did not further corroborate this lack of directional restriction with any other arrangement of beams. Furthermore, the metamaterial that they used was shorter in thickness ($d = 800$ nm) than the free-space optical wavelength used in their experiment ($\lambda = 1510$ nm). It is well-known that phase mismatch is not a major concern over such small propagation lengths [20].

If we continue with this line of reasoning and arrange for all the components of our nonlinear interaction to have a near-zero refractive index, an interaction can be phase-matched irrespective of the orientation of all input and output beams — omnidirectional phase matching. Effectively, such a near-zero-index medium would allow for the generation of a nonlinear signal in any desired direction for any arbitrary direction of beams, for *all* parametric nonlinear processes.

1.2 Objectives of the thesis and our approach to phase matching

In this thesis, we address the phase-matching problem by using such near-zero-index media. These media exhibit a refractive index n of zero at a wavelength of 1600 nm, and a very small refractive index in a 100 nm range in the surrounding bandwidth [21]. We investigate the underlying theory and present calculations that reveal the potential for omnidirectional phase matching in zero-index materials by using the nonlinear optical process of FWM as an exemplar. Furthermore, we perform experimental demonstrations of phase matching for five separate FWM beam configurations to confirm this phenomenon, and compare our experimental results to theoretical predictions.

Our experiment features several notable modifications and additional results compared

to the report published by Suchowski *et al.* Our first and most substantial additional result is the demonstration of a lack of dimensional restriction for all beams involved in the interaction, as opposed to solely the generated signal beam. Our demonstration also features the generation of a spectrally distinct signal wave not only when the input pump and probe beams are co- and counter-propagating, but also when the input probe beam's wave vector is orthogonal to that of the pump and signal waves. Critically, both of these feats are previously unobserved phenomena. The latter demonstration is of particular importance, as it reveals that the components of the nonlinear interaction need not even be collinear for an interaction to be phase-matched. We additionally improve on Suchowski *et al.*'s previous demonstration by realizing our experiment in a nonlinear waveguide 14.8 µm in length, as opposed to the 800 nm fishnet metamaterial they employed. As stated above, in a shorter metasurface, phase mismatch is not a major concern due to the small propagation length not allowing the constituent waves to go out of phase [20]. In contrast, a 14.8 µm waveguide corresponds to almost 10 free-space optical wavelengths, and sets the lower bound on the coherence length at roughly 8 µm (See Appendix A.1), allowing us to better demonstrate that our interaction is phase-matched. Finally, our demonstration uses multiple spectrally distinct beams as opposed to a degenerate FWM process. By having spectrally distinct components in our FWM process, our measurements are capable of cleanly isolating the generated nonlinear pulse from the inputs, and, therefore, unambiguously demonstrate our effect. By validating the impressive phase-matching capabilities of zero-index materials in such a manner, we hope to expand upon the already established exceptional properties of zero-index materials, provide future researchers with an avenue to conveniently phase-match their processes when working with nonlinear optics, and provide a way to miniaturize nonlinear devices [22].

1.3 Thesis structure

The current chapter (Chapter 1) provides an overview of phase-matching in zero-index materials and underlines the importance of current research in this field. Chapter 2 provides the theory underlying this thesis, including an overview of nonlinear optics, the derivation of the phase-matching condition for nonlinear optical interactions, and an overview of zero-index materials. Chapter 3 describes the Dirac-cone zero-index waveguides utilized in this work, their modeling, and their subsequent fabrication. Chapter 4 models FWM and phase matching in the Dirac-cone zero-index waveguides used in the experiment and predicts experimental behavior. Chapter 5 provides an overview of the experiment, explains the structure of the experimental setup, shows the results obtained from performing FWM in Dirac-cone zero-index materials, and analyzes the obtained results. Chapter 6 assesses the final results and conclusions and explores future possibilities to build upon the experiment elaborated upon in this thesis.

Chapter Two

Theory

The work in this thesis focuses on phase matching nonlinear optical interactions. In this chapter, we will first look at the theory underlying nonlinear optics, and then, building upon this theoretical derivation, examine the theory surrounding four-wave mixing (FWM), as well as phase matching in FWM interactions. We will then demonstrate how zero-index materials can be used to alleviate the challenges surrounding phase matching in FWM, as well as all parametric nonlinear interactions. The theoretical material from Sections 2.1 and 2.2 of this chapter is derived by following the methods outlined in [23].

2.1 Nonlinear Optics

In introductory physics classes, it is commonly taught that when two waves interact, the result is a linear addition of both waves. This is known as the superposition principle. However, at very high powers, the superposition principle does not necessarily hold. Nonlinear optics is the study of such nonlinear phenomena specific to light. In nonlinear optics, interactions such as the combination of two lower-energy photons into a higher energy photon, known as second-harmonic generation (SHG, shown in Fig. 2.1), become possible. This particular interaction was first demonstrated in 1961 by Franken *et al.* after the invention of lasers, and its discovery is widely considered to be the beginning of the field of nonlinear optics [23, 24, 25].

The most common way to treat nonlinearities is to consider the situation where the polarization density, $\mathbf{P}$, responds nonlinearly to the electric field of the incident light, $\mathbf{E}$. Ordinarily, for a lossless and dispersionless material, the dependence is linear such that

$$\mathbf{P}(t) = \epsilon_0 \chi_e \mathbf{E}(t) \tag{2.1}$$

where ϵ_0 is the vacuum permittivity, χ_e is the electric susceptibility, and t is time. In a nonlinear medium, this expression can be expanded in a power series as a function of the electric field in the form

$$\begin{aligned} \mathbf{P}(t) &= \epsilon_0 \left(\chi^{(1)} \mathbf{E}(t) + \chi^{(2)} \mathbf{E}^2(t) + \chi^{(3)} \mathbf{E}^3(t) + ... \right) && (2.2) \\ &= \mathbf{P}^{(1)}(t) + \mathbf{P}^{(2)}(t) + \mathbf{P}^{(3)}(t) + ... && (2.3) \end{aligned}$$

and so on, where $\chi^{(1)}$ is the linear susceptibility, and $\chi^{(2)}$ and $\chi^{(3)}$ are the second- and third-order nonlinear susceptibilities, respectively. While generally the nonlinear susceptibilities

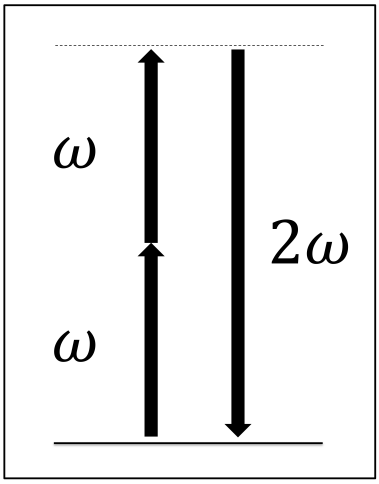

Figure 2.1 Energy conservation for a second-harmonic generation process. Two photons of energy ω combine to create a new photon of energy 2ω.

are quantities which vary based on the applied frequencies, in the approximation of a dispersionless material, they may be taken to be constants. As the values of the nonlinear susceptibilities are very small (on the order of 10^{-12} V/m for $\chi^{(2)}$, and 10^{-24} V^2/m^2 for $\chi^{(3)}$), these additional terms do not make significant contributions until the power of the electric field reaches sufficiently high values [26].

2.1.1 Second-order nonlinear optical interactions

The consequences of a nonlinear response from the polarization density $\mathbf{P}(t)$ of the form of Eq. (2.2) is not immediately clear. To better understand what this equation implies, we can begin by examining the first nonlinear term, given by

$$\mathbf{P}^{(2)}(t) = \epsilon_0 \chi^{(2)} \mathbf{E}^2(t) \tag{2.4}$$

in order to develop an intuition for the higher order terms. To do this, we can substitute a simple electric field with two frequency components ω_1 and ω_2 into this expression of the form

$$\mathbf{E}(t) = E_1 e^{-i\omega_1 t} + E_2 e^{-i\omega_2 t} + c.c. \tag{2.5}$$

where c.c. denotes the complex conjugate. The result of this substitution is an expression with 10 separate terms:

$$\begin{aligned}\mathbf{P}^{(2)}(t) = 2\epsilon_0\chi^{(2)}\left(E_1E_1^* + E_2E_2^*\right) + \epsilon_0\chi^{(2)}(E_1^2e^{-2i\omega_1 t} + E_2^2e^{-2i\omega_2 t} \\ + 2E_1E_2e^{-i(\omega_1+\omega_2)t} + E_1E_2^*e^{-i(\omega_1-\omega_2)t} + c.c.).\end{aligned} \tag{2.6}$$

From this expression, the implication of Eq. (2.2) is far clearer. Each of the individual terms contained in Eq. (2.6) represents its own second-order nonlinear interaction. The nonlinear interaction of second-harmonic generation occurs as a consequence of the terms

$$P(2\omega_1) = \epsilon_0 \chi^{(2)} E_1^2, \tag{2.7}$$

$$P(2\omega_2) = \epsilon_0 \chi^{(2)} E_2^2 \tag{2.8}$$

where we have introduced the notation

$$\mathbf{P}^{(2)}(t) = \sum_n P(\omega_n) e^{-i\omega_n t}. \tag{2.9}$$

These terms represent the second-harmonic generation of signal waves of energy $\omega = 2\omega_1$ and $\omega = 2\omega_2$ from pump waves of energy ω_1 and ω_2, respectively. We can also note terms corresponding to other second-order interactions. For example, sum-frequency generation (SFG) is a process wherein two photons of energy ω_1 and ω_2 combine to yield a photon of energy $\omega_3 = \omega_1 + \omega_2$. In difference-frequency generation (DFG), a higher energy photon of energy ω_1 splits into two new photons of energy ω_2 and $\omega_3 = \omega_1 - \omega_2$. Another process known as optical rectification (OR) occurs when the new frequency is the difference of one frequency with itself, generating a static electric field. These interactions, shown in Fig. 2.2, are represented by the terms

$$P(\omega_1 + \omega_2) = 2\epsilon_0 \chi^{(2)} E_1 E_2, \quad \text{(SFG)} \tag{2.10}$$

$$P(\omega_1 - \omega_2) = 2\epsilon_0 \chi^{(2)} E_1 E_2^*, \quad \text{(DFG)} \tag{2.11}$$

$$P(0) = 2\epsilon_0 \chi^{(2)} (E_1 E_1^* + E_2 E_2^*). \quad \text{(OR)} \tag{2.12}$$

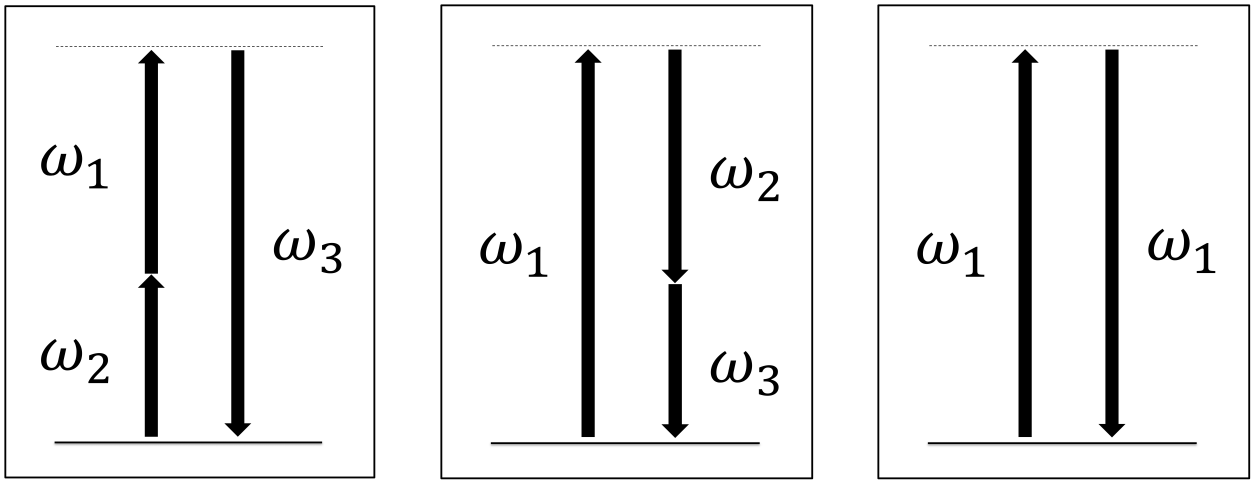

(a) Sum-frequency generation

(b) Difference-frequency generation

(c) Optical rectification

Figure 2.2 Energy conservation for sum-frequency generation, difference-frequency generation, and optical rectification processes.

These equations can also be represented by their negative frequency equivalents, which can be obtained by using the complex conjugate terms contained in Eq. (2.6). However, this simply yields the complex conjugates of equations (2.10) to (2.12), and as a result, taking both the positive and negative frequency components into account is not necessary [23].

2.1.2 Four-wave mixing

Having now treated second-order nonlinear optical interactions in Section 2.1.1, we can now follow the same procedure to define FWM by expanding the third term in the perturbative expansion $\epsilon_0\chi^{(3)}\mathbf{E}^3(t)$, and into it substituting an electric field with three distinct frequency components

$$\mathbf{E}(t) = E_1 e^{-i\omega_1 t} + E_2 e^{-i\omega_2 t} + E_3 e^{-i\omega_3 t} + c.c. \tag{2.13}$$

This substitution yields a very long expression with 44 distinct frequency terms. In this work, we use the third-order nonlinear optical process of *pump-degenerate four-wave mixing*. This FWM interaction is given by the term

$$P(2\omega_1 - \omega_2) = 3\epsilon_0\chi^{(3)}E_1^2E_2^*. \tag{2.14}$$

In a pump-degenerate FWM nonlinear optical process, two photons of energy ω_1, known as the *pump* photons, are converted into a photon of energy ω_2, known as the *signal* photon, and a photon of frequency $\omega_3 = 2\omega_1 - \omega_2$, known as the *idler* photon [23]:

$$\omega_p + \omega_p = (\omega_p + \delta\omega) + (\omega_p - \delta\omega), \tag{2.15}$$

$$= \omega_s + \omega_i. \tag{2.16}$$

Here, pump degeneracy refers to the fact that both pump photons possess the same energy. However, as pump-degenerate FWM is the most commonly used FWM process [27, 28], it is widely referred to in literature as simply FWM. In the remainder of this work, all mentions of FWM will refer to the pump-degenerate variant. FWM has a variety of uses, such as in optical parametric amplifiers and oscillators [29], as well as in generating entangled photon pairs in quantum optics [30, 31].

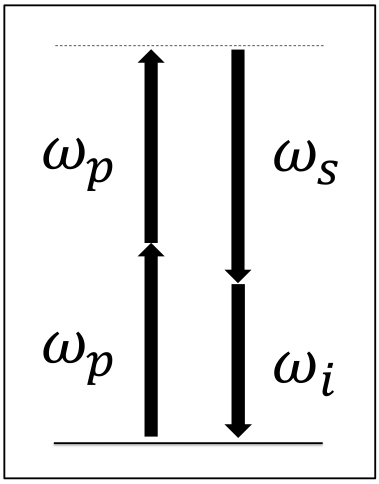

Figure 2.3 Energy conservation for a FWM process. Two pump photons of energy ω_p combine to create two new photons of energy ω_s and ω_i, known as the signal and idler photons, respectively.

2.2 Wave-equation in nonlinear optics

Now that we have defined FWM, it can be more thoroughly understood when interpreted with the electromagnetic wave equation, a second-order partial differential equation describing the propagation of electromagnetic waves. The electromagnetic wave equation, which we will now derive, can be obtained from Maxwell's equations. When assuming no free charges are present such that the electric charge density $\rho = 0$, and no free currents exist such that the electric current density $\mathbf{J} = 0$, Maxwell's equations are of the form

$$\nabla \cdot \mathbf{D} = 0, \tag{2.17}$$

$$\nabla \cdot \mathbf{B} = 0, \tag{2.18}$$

$$\nabla \times \mathbf{E} = -\frac{\partial \mathbf{B}}{\partial t}, \tag{2.19}$$

$$\nabla \times \mathbf{H} = \frac{\partial \mathbf{D}}{\partial t} \tag{2.20}$$

where $\mathbf{B}$ is the magnetic induction field, $\mathbf{D}$ is the electric displacement field, and $\mathbf{H}$ is the magnetic intensity field. We can additionally assume a lossless, dispersionless, isotropic nonlinear material. Under these conditions, the fields $\mathbf{B}$ and $\mathbf{H}$, as well as the fields $\mathbf{E}$ and $\mathbf{D}$, are associated by the equations

$$\mathbf{B} = \mu_0 \mu \mathbf{H}, \tag{2.21}$$

$$\mathbf{D} = \epsilon_0 \epsilon \mathbf{E} + \mathbf{P}^{NL} \tag{2.22}$$

where $\mathbf{P}^{NL}$ is the nonlinear component of the polarization density, μ_0 is the vacuum permeability, ϵ is the relative permittivity, and μ is the relative permeability. The nonlinear optical wave equation can be derived from these equations. To obtain it, we substitute Eq. (2.21) into Eq. (2.19). We then take the curl of both sides of this equation, and substitute Eq. (2.20) in the resulting expression to obtain

$$\nabla \times \nabla \times \mathbf{E} + \epsilon_0 \mu_0 \epsilon \mu \frac{\partial^2 \mathbf{E}}{\partial t^2} + \mu_0 \mu \frac{\partial^2 \mathbf{P}^{NL}}{\partial t^2} = 0, \tag{2.23}$$

which, after making use of the substitution $\mu_0 \epsilon_0 = 1/c^2$, where c is the speed of light, can alternatively be expressed as

$$\nabla \times \nabla \times \mathbf{E} + \frac{\epsilon \mu}{c^2} \frac{\partial^2 \mathbf{E}}{\partial t^2} + \frac{\mu}{\epsilon_0 c^2} \frac{\partial^2 \mathbf{P}^{NL}}{\partial t^2} = 0. \tag{2.24}$$

This is the most general form of the wave equation, but in most cases when working in nonlinear optics, it can be further simplified. A vector calculus identity states that the first term of the equation can be represented as

$$\nabla \times \nabla \times \mathbf{E} = \nabla(\nabla \cdot \mathbf{E}) - \nabla^2 \mathbf{E}. \tag{2.25}$$

While $\nabla^2 \mathbf{E}$ is generally non-vanishing, in cases of interest, such as an electric field in the form of a transverse, infinite plane wave, $\nabla \cdot \mathbf{E}$ vanishes, and can more generally be shown

to be very small in most other cases. This is especially true when the slowly varying amplitude approximation is valid (explained in more detail in Section 2.2.1). By making this approximation, we can write the wave equation in the form

$$\nabla^2 \mathbf{E}_n - \frac{\epsilon_n \mu_n}{c^2} \frac{\partial^2 \mathbf{E}_n}{\partial t^2} = \frac{\mu_n}{\epsilon_0 c^2} \frac{\partial^2 \mathbf{P}_n^{NL}}{\partial t^2} \tag{2.26}$$

for each frequency component of the field, and for which ϵ_n and μ_n are understood to vary as a function of frequency. Here, the subscript n is used to denote an individual component of the field (i.e. pump, signal or idler). This form of the wave equation will be the form we use for all subsequent analysis of FWM interactions.

2.2.1 Coupled-amplitude equations

With Eq. (2.26), we now have the tools to describe and more thoroughly understand a FWM interaction. We consider the standard case of a FWM process where all components are co-propagating, as shown in Fig. 2.4.

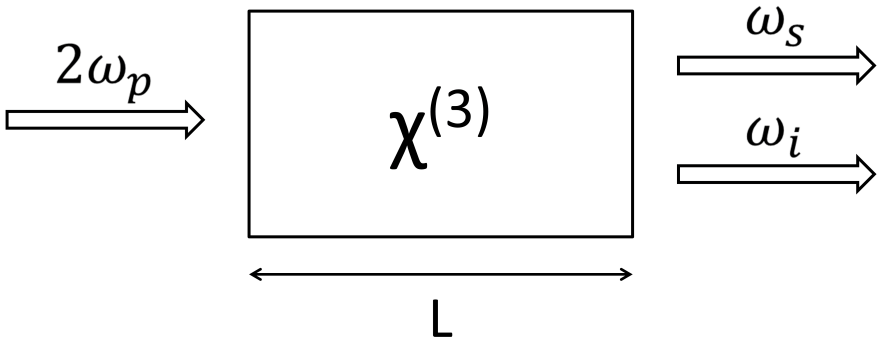

Figure 2.4 Schematic of a FWM process with co-propagating beams in a nonlinear medium with $\chi^{(3)}$ of length L.

When the nonlinear source term in Eq. (2.26) is zero ($\mathbf{P}_n^{NL} = 0$), the solution to this equation is a plane wave of angular frequency ω_n propagating in the z direction that is represented by the expression

$$\mathbf{E}_n(z,t) = A_n e^{i(k_n z - \omega_n t)} + c.c. \tag{2.27}$$

where A_n is the scalar amplitude of the electric field, and k_n is the wave vector. Given the scalar field approximation, we have the dispersion relation

$$k_n = \frac{n_n \omega_n}{c}, \tag{2.28}$$

$$n_n^2 = \epsilon_n \mu_n \tag{2.29}$$

where n_n is the refractive index. When the nonlinear source term is not very large, it is expected that the solution to Eq. (2.26) will be of the same form as Eq. (2.27), but with A_n varying as a function of z. We can therefore use Eq. (2.27) with $A_n(z)$ as our trial solution

for Eq. (2.26) with the nonlinear source term included. We can represent this nonlinear source term as

$$\mathbf{P}_n(z,t) = P_n e^{-i\omega_n t} + c.c. \tag{2.30}$$

where P_n is the scalar amplitude of the nonlinear component of the polarization density. The pump, signal, and idler wave terms for P_n, of the form of Eq. (2.14), are given by

$$P_p = 3\epsilon_0 \chi^{(3)} A_p^* A_s A_i e^{i(k_s z + k_i z - k_p z)} + c.c. \tag{2.31}$$

$$P_s = 3\epsilon_0 \chi^{(3)} {A_p}^2 A_i^* e^{i(2k_p z - k_i z)} + c.c. \tag{2.32}$$

$$P_i = 3\epsilon_0 \chi^{(3)} {A_p}^2 A_s^* e^{i(2k_p z - k_s z)} + c.c. \tag{2.33}$$

Here, we use p, s, and i as subscripts to denote the pump, signal, and idler waves respectively. From here, for each frequency component of the field, we substitute our trial solution Eq. (2.27) and nonlinear source term Eq. (2.30) into the final form of the wave equation Eq. (2.26). This expression can then be simplified to yield equations governing the propagation and evolution of the pump, signal, and idler fields. Without loss of generality, we here follow the derivation for the idler wave. Since the fields only depend on z, ∇^2 can be replaced by d^2/dz^2. As the inclusion of the complex conjugate terms would simply yield the complex analogue of the same equation, we here drop them for simplicity of derivation. When substituting our trial solution and nonlinear source term for the idler wave into Eq. (2.26), we obtain

$$\frac{d^2}{dz^2}\left(A_i e^{i(k_i z - \omega_i t)}\right) - \frac{\epsilon_i \mu_i}{c^2}\frac{\partial^2}{\partial t^2}\left(A_i e^{i(k_i z - \omega_i t)}\right) = \frac{\mu_i}{\epsilon_0 c^2}\frac{\partial^2}{\partial t^2}\left(3\epsilon_0 \chi^{(3)} A_p^2 A_s^* e^{i(2k_p z - k_s z - \omega_i t)}\right). \tag{2.34}$$

After performing the derivatives, this expression simplifies to

$$\left(\frac{d^2 A_i}{dz^2} + 2ik_i \frac{dA_i}{dz} - k_i^2 A_i + \frac{\epsilon_i \mu_i \omega_i^2}{c^2} A_i\right) e^{i(k_i z - \omega_i t)} = \frac{-3\mu_i \omega_i^2 \chi^{(3)}}{c^2} A_p^2 A_s^* e^{i(2k_p z - k_s z - \omega_i t)}. \tag{2.35}$$

Due to Eq. (2.29), the third and fourth terms of the right-hand side of the equation cancel out. Furthermore, we can group all the exponential terms on one side. This yields

$$\frac{d^2 A_i}{dz^2} + 2ik_i \frac{dA_i}{dz} = \frac{-3\mu_i \omega_i^2 \chi^{(3)}}{c^2} A_p^2 A_s^* e^{i(2k_p z - k_s z - k_i z)}. \tag{2.36}$$

This equation is the most general form of the idler's coupled-amplitude equation. However, in the majority of cases of interest, the second derivative can be dropped after using the slowly varying amplitude approximation (SVAA), which states

$$\left|\frac{d^2 A_i}{dz^2}\right| \ll \left|k_i \frac{dA_i}{dz}\right|. \tag{2.37}$$

The SVAA asserts that the envelope of a pulse varies slowly in space on the scale of a wavelength [32]. We can additionally designate a new parameter named the wave-vector mismatch of the FWM process, defined as the quantity

$$\Delta k \equiv 2k_p - k_s - k_i. \tag{2.38}$$

This expression for the wave-vector mismatch is known as the phase-matching condition. By incorporating Eq. (2.37) and Eq. (2.38) into our current result, and thereafter making use of Eq. (2.28), we obtain

$$\frac{dA_i}{dz} = \frac{3i\mu_i\chi^{(3)}\omega_i}{2n_ic}A_p^2A_s^*e^{i\Delta kz}. \tag{2.39}$$

Which is known as the coupled-amplitude equation of the idler frequency. It is known as a coupled-amplitude equation because it describes how the amplitude of the idler wave varies as a function of the amplitude of the other two waves. By following an analogous procedure to the idler wave, we can also obtain coupled-amplitude equations for both the pump and signal waves:

$$\frac{dA_p}{dz} = \frac{3i\mu_p\chi^{(3)}\omega_p}{2n_pc}A_p^*A_sA_ie^{-i\Delta kz}, \tag{2.40}$$

$$\frac{dA_s}{dz} = \frac{3i\mu_s\chi^{(3)}\omega_s}{2n_sc}A_p^2A_i^*e^{i\Delta kz}. \tag{2.41}$$

These coupled-amplitude equations are a set of three coupled differential equations that may be solved together as a function of propagation distance in a nonlinear medium. In effect, these equations completely describe our FWM interaction. In general, these equations cannot be solved analytically. Nevertheless, an analytical solution can be obtained when certain approximations are made. In the next section, we investigate how these equations can be solved when using the *undepleted pump approximation*.

2.2.2 Phase matching

In order to facilitate solving Eqs. (2.39) to (2.41), we use the undepleted pump approximation. This approximation states that the input fields (i.e., the pump and signal waves in our case) are not depleted by the nonlinear process, and that as a result, the pump and signal wave amplitudes A_p and A_s remain constant. While in our eventual system radiative losses will be too high for this approximation to be valid, using this approximation still gives us some valuable intuition. When this is true, and when we also have the condition of *perfect phase matching* $\Delta k = 0$, Eq. (2.39) can be easily solved:

$$A_i = \frac{3i\mu_i\chi^{(3)}\omega_i}{2n_ic}A_p^2A_s^*L. \tag{2.42}$$

where L is the length of the waveguide, over which we have integrated (Fig. 2.4). With perfect phase matching, the amplitude of the idler wave A_i will grow linearly with the interaction length. The power P of a wave (not to be confused with the polarization density) exhibits a quadratic dependence on the modulus of the amplitude given by

$$\frac{P}{S} = 2n\epsilon_0c|A|^2 \tag{2.43}$$

where S is the surface area. Therefore, a linear increase in the idler amplitude A_i leads to a quadratic increase in the idler power P_i over distance. When the condition of perfect

phase matching is not satisfied, but the undepleted pump approximation remains valid, the solution to Eq. (2.39) becomes

$$A_i = \frac{3i\mu_i\chi^{(3)}\omega_i}{2n_ic}A_p^{*2}A_s\int_0^L e^{i\Delta kz}dz \tag{2.44}$$

$$= \frac{3i\mu_i\chi^{(3)}\omega_i}{2n_ic}A_p^{*2}A_s\left(\frac{e^{i\Delta kL}-1}{i\Delta k}\right). \tag{2.45}$$

When the modulus of the amplitude is squared as in Eq. (2.43), we obtain

$$|A_i|^2 = \frac{9{\mu_i}^2{\chi^{(3)}}^2\omega_i^2}{4n_i^2c^2}|A_p|^4|A_s|^2\left|\frac{e^{i\Delta kL}-1}{i\Delta k}\right|^2. \tag{2.46}$$

The square of the modulus of the phase-matching term in Eq. (2.46) can be expressed in terms of the sinc. function via

$$\left|\frac{e^{i\Delta kL}-1}{i\Delta k}\right|^2 = L^2\left(\frac{e^{i\Delta kL}-1}{\Delta kL}\right)\left(\frac{e^{-i\Delta kL}-1}{\Delta kL}\right) = 2L^2\frac{(1-\cos\Delta kL)}{(\Delta kL)^2} \tag{2.47}$$

$$= L^2\frac{\sin^2(\Delta kL/2)}{(\Delta kL/2)^2} \equiv L^2\,\mathrm{sinc}^2(\Delta kL/2). \tag{2.48}$$

Additionally, it can be very useful to think of phase matching in terms of the coherence length [33], which is a quantity given by

$$L_{\mathrm{coh}} = 2/\Delta k. \tag{2.49}$$

This parameter indicates the length over which a nonlinear interaction remains coherent, i.e. where there is constructive interference of a generated idler wave. With perfect phase matching, this quantity approaches infinity and, therefore, light can continue building coherently for the entire length of the nonlinear medium. This quantity is very useful, because a long coherence length means that the interaction can occur over a longer distance L. As a result, its power may keep accruing over this longer distance. We later use L_{coh} to quantify when our interactions are well phase-matched. When L_{coh} is substituted into Eq. (2.48), the modulus squared term in Eq. (2.46) can be represented as

$$\left|\frac{e^{i\Delta kL}-1}{i\Delta k}\right|^2 = L^2\,\mathrm{sinc}^2\left(L/L_{\mathrm{coh}}\right) \tag{2.50}$$

From this expression, it can be seen that the power, given by Eq. (2.46), in part varies sinusoidally with the interaction length L. Here, the sinusoidal dependence arises from the fact that the waves go into and out of phase with one another as they propagate in the medium. Initially, when the waves are in phase, there is constructive interference of a generated idler wave. However, as the waves move out of phase, the generated idler wave begins to interfere destructively with itself. The modulus of the amplitude squared can finally be written as

$$|A_i|^2 = \frac{9{\mu_i}^2{\chi^{(3)}}^2\omega_i^2}{4n_i^2c^2}|A_p|^4|A_s|^2L^2\,\mathrm{sinc}^2\left(L/L_{\mathrm{coh}}\right). \tag{2.51}$$

As the sinc. function peaks when its argument is zero, an increase in the wave-vector mismatch leads to a decrease in the generated idler power (Fig. 2.5). Therefore, perfect phase matching allows for the optimal strength of a FWM interaction. While, here, we have obtained and solved the coupled-amplitude equations for FWM, the wave equation can also be solved for other nonlinear interactions to yield equations with their respective phase-matching conditions. This phase-matching condition, just as above, is always given by the difference in momentum between the input and output waves of a given interaction. Given that achieving perfect phase matching by having the phase-matching condition equal to zero is critical for the strength and coherence length of a nonlinear optical interaction, as determined in this section, it is therefore critical to satisfy this condition. In the next section, we look at zero-index materials, and analyze the properties that these materials exhibit which can be used to achieve phase matching in FWM, and also in other related nonlinear interactions.

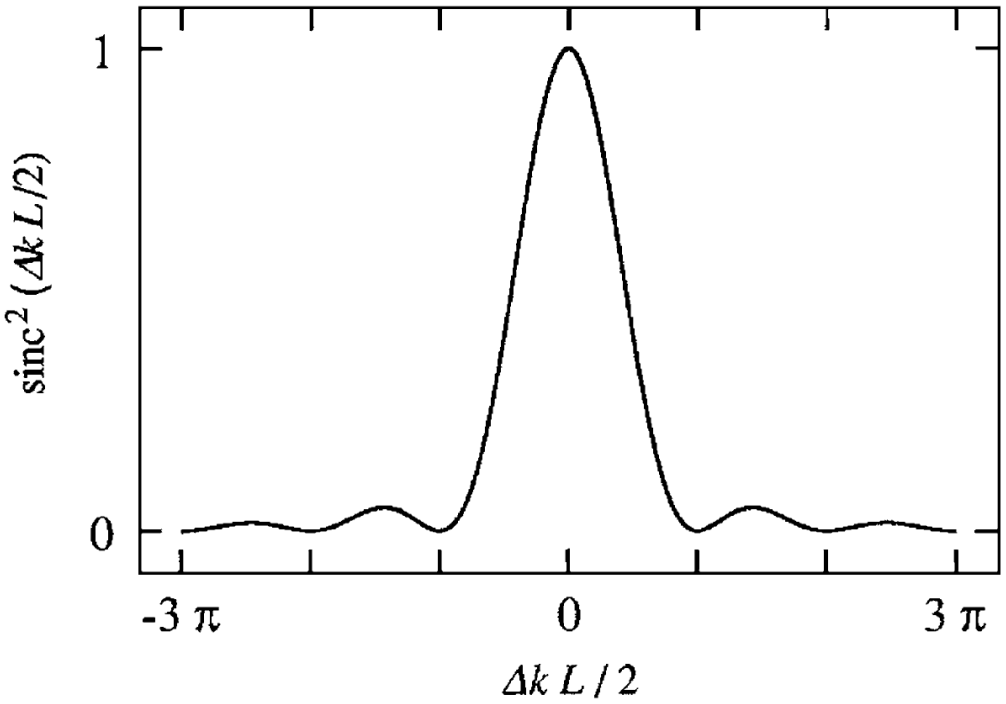

Figure 2.5 Value of the sinc. function as a function of its argument $\Delta kL/2$. When the argument is equal to zero, the sinc. function peaks at unity. As the argument grows larger, the value the sinc. function returns grows smaller and smaller. Reproduced from [23].

2.3 Zero-index materials

Much like how the superposition principle is commonly taught in introductory physics classes, so is the notion that a refractive index may not be lower than one. As the vacuum is defined as having a refractive index of one, a lesser refractive index would imply very strange phe-

nomena, such as a phase velocity exceeding that of light. However, while materials with such refractive indices are uncommon in naturally occurring materials, it is possible to engineer materials with refractive indices lower than one. This includes not only materials with positive refractive indices lower than unity, but also materials with negative refractive indices (known as negative-index materials) [34, 35, 36, 37], and materials with refractive indices of zero (known as zero-index materials) [22, 38, 39]. Here, we will focus on the properties of zero-index materials, and their implications in facilitating phase-matching constraints.

2.3.1 Properties of zero-index materials

Zero-index materials possess a variety of interesting properties, the most notable of which are an infinite phase velocity resulting in phaseless propagation, and an enhancement of the electric field [22, 36, 40, 41, 42]. Verifying that the phase velocity is infinite can be done rather simply by observing the relation

$$v_p = c/n \tag{2.52}$$

where v_p is the phase velocity of the wave. When $n = 0$, v diverges to an infinite value. How could it be possible that the phase velocity exceed that of light and seemingly violate special relativity? The answer to this is that special relativity mandates that the *signal velocity* (i.e., the speed of information) not exceed that of light, and that the phase velocity may take any value [43]. Consider the group velocity of light. In most common cases, including this case, the signal velocity is equal to the group velocity. The group velocity can be expressed as:

$$v_g = \frac{c}{n + \omega\frac{\partial n}{\partial \omega}}. \tag{2.53}$$

In the absence of any dispersion (i.e., $\partial n/\partial\omega = 0$), the group velocity is equal to the phase velocity. It logically follows as a result that any zero-index medium must have some amount of dispersion. This also means that the refractive index can only be zero at a single point without incurring very large losses. This zero-crossing wavelength is known as the zero-index crossing wavelength, or more simply, the *zero-index wavelength*.

Using the relation $\lambda = \lambda_0/n$, where λ_0 is the free-space wavelength, it can also be seen that the effective wavelength λ is infinite inside a zero-index material. This results in a phenomenon known as *phase-free propagation* [21, 40, 44]. As shown in Subsection 2.2.1, the solution to the wave equation without a nonlinear source term is a plane wave given by

$$\mathbf{E}(z,t) = Ae^{i(kz-\omega t+\phi)} + c.c. \tag{2.54}$$

where A is a constant, and ϕ is the initial phase of the plane wave and also a constant. However, in a zero-index material, the momentum $k = 2\pi n/\lambda_0$ becomes zero. As a result, the kz term in the argument of the exponential vanishes, and the expression for the plane wave becomes

$$\mathbf{E}(z,t) = Ae^{i(\omega t+\phi)} + c.c. \tag{2.55}$$

In this expression, the electric field is no longer a function of z. Consequently, this means that once the wave enters the zero-index material, it propagates in space without undergoing

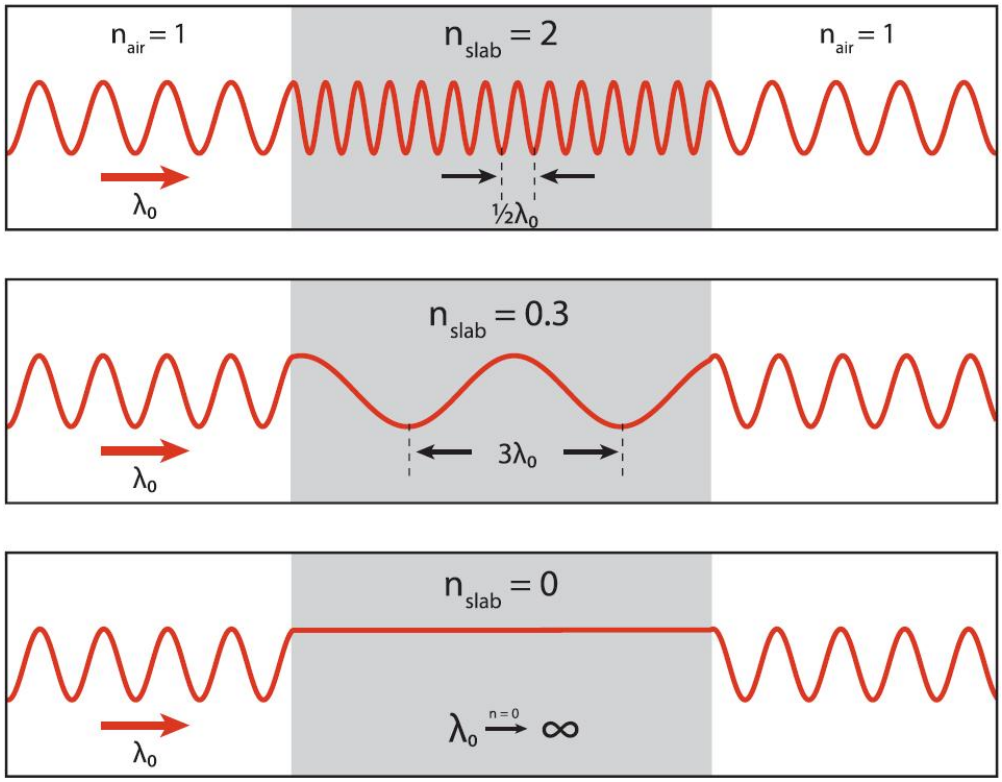

Figure 2.6 A light wave in air where $n = 1$, enters and exits a lossless slab with $n = 2$. When the wave enters the zero-index medium, the wavelength is compressed. If the light wave enters and exits a slab with $n = 0.3$, the wavelength is stretched. If the medium has $n = 0$, the wavelength is infinitely stretched, and its phase remains "paused"; it propagates without accruing any additional phase. Reproduced from [45]

.

any further spatial variation, retaining the phase and amplitude it had once it entered the material. This phaseless propagation can be seen in Fig. 2.6.

We can derive two further conclusions regarding the direction of propagation in zero-index materials by observing Snell's law. Snell's law is given by the relation

$$n_1 \sin\theta_1 = n_2 \sin\theta_2. \tag{2.56}$$

Here, n_1 and n_2 are the refractive indices of two distinct media, while θ_1 and θ_2 are the angles of light relative to normal incidence (shown in Fig. 2.7). Snell's law states that a ray of light in a medium with n_1 impinging on a medium with n_2 at an incident angle θ_1 will take an angle θ_2 in the new medium.

Consider the case where n_1 is unity, and the second medium is our zero-index material with $n_2 = 0$. These two refractive indices engender two unique properties from the incident angles. The first consequence is that, as $\sin\theta_1 = 0$, the incident angle of the first beam must be at normal incidence ($\pi/2$), and therefore any light impinging on the zero-index material that is not normal to the surface will be totally reflected. The second consequence is that,

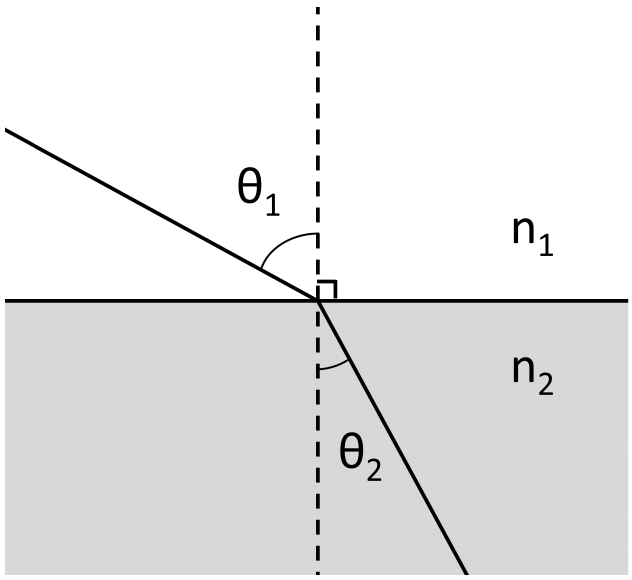

Figure 2.7 A light ray at an incident angle θ_1 in a medium with refractive index n_1 enters a medium with a refractive index n_2. Its incident angle changes to θ_2 as a consequence. In this case, $n_1 > n_2$. In a zero-index material where $n_2 = 0$, θ_2 may take any desired value, while θ_1 must be zero for Snell's law to be satisfied.

as $n_2 \sin\theta_2 = 0$, θ_2 is free to assume any value. As a result, when light enters the zero-index medium, it is physically free to assume any angle. This results in light traveling in all directions within the material.

2.3.2 Phase matching in zero-index materials

In addition to the various properties described in Subsection 2.3.1, zero-index materials possess very special properties when applied to phase matching [15, 46]. As determined in Subsection 2.2.1, the phase-matching condition for a FWM interaction when all beams are co-propagating is given by the difference in momenta between the input and output beams $\Delta k = 2k_p - k_s - k_i$. From the previous subsection, we also know that the momenta are proportional to the refractive index, and vanishing when $n = 0$. At first glance, this would seem to indicate that the phase mismatch completely disappears! However, unless the process is degenerate (i.e., the pump, signal, and idler waves have the same frequency), only one component of the interaction may be localized at the zero-index wavelength. Nevertheless, zero-index materials can eliminate the phase-matching contribution of whichever wave located at the zero-index wavelength, and as a result, possess the ability to make the phase-matching contribution *independent* of the orientation of this particular wave.

For example, suppose we wanted a configuration where the signal wave was orthogonal to pump and idler waves, as shown in Fig. 2.8. If we make the judicious choice of placing the signal wave at $n(\lambda_s) = 0$, we obtain $\Delta k = 2k_p - k_i$ after the disappearance of k_s. If the phase-matching condition for FWM is satisfied when all beams are co-propagating, then it is also satisfied when the signal beam is orthogonal to the pump and idler waves. In

Chapter 4, we will theoretically describe FWM and phase matching for non-conventional beam orientations like that of Fig. 2.8.

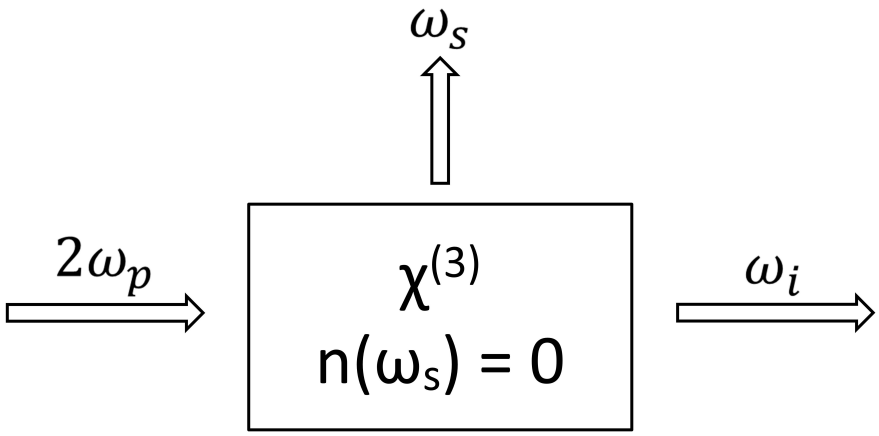

Figure 2.8 A pump wave produces an idler wave conventionally co-propagating with the pump wave, and a signal wave propagating orthogonal to the pump and idler waves. However, as the signal wave's momentum is $k_s = 0$ due to the vanishing refractive index, the direction of propagation of the signal wave is inconsequential to how well the interaction is phase-matched.

2.3.3 EMNZ materials

While zero-index materials possess very interesting properties, one may wonder how a refractive index of zero can be achieved. As the refractive index is given by

$$n = \sqrt{\epsilon\mu}, \tag{2.57}$$

any material engineered such that the permittivity ϵ or permeability μ cross zero will possess a near-zero refractive index nearby the crossing point. Such materials are known as *epsilon-near-zero* (ENZ) materials and *mu-near-zero* (MNZ) materials respectively. ENZ materials in particular have attracted much attention recently due to their increased nonlinear response [47, 48, 49].

The wave impedance of an electromagnetic wave is defined as [50]

$$\eta = \sqrt{\frac{\mu_0\mu}{\epsilon_0\epsilon}} = \eta_0\sqrt{\frac{\mu}{\epsilon}} = \eta_0\sqrt{\frac{\mu^2}{\epsilon\mu}} = \eta_0\frac{\mu}{n} \tag{2.58}$$

where $\eta_0 = \sqrt{\mu_0/\epsilon_0}$ is the free-space impedance. In the case of an ENZ material, the impedance will be infinite, while in the case of an MNZ material, the impedance will be zero. As Eq. (2.39) contains a μ/n term, it can also be expressed as

$$\frac{dA_i}{dz} = \frac{3i\chi^{(3)}\omega_i}{2c}\sqrt{\frac{\mu}{\epsilon}}A_p^2A_s^*e^{i\Delta kz} \tag{2.59}$$

$$= \frac{3i\chi^{(3)}\omega_i}{2c}\frac{\eta}{\eta_0}A_p^2A_s^*e^{i\Delta kz}. \tag{2.60}$$

This equation implies that an MNZ material will experience no nonlinearity due to its vanishing impedance, while an ENZ material will experience a nonlinear enhancement due to its diverging impedance value, in agreement with the prior assertion that ENZ materials experience increased nonlinear responses. This equation also asserts that materials with very high permeability values will be very nonlinear. However, the impedance also very critically determines the reflectivity of a surface. In the case of a plane wave in a medium with impedance η_1 incident on the boundary of another medium with impedance η_2, the power reflection is defined as

$$R = \left(\frac{\eta_2 - \eta_1}{\eta_2 + \eta_1} \right)^2 . \tag{2.61}$$

For a material that is either ENZ or MNZ, R is equal to unity. This means that both ENZ and MNZ materials are extremely reflective, which is a significant downside for both materials. However, Eq. (2.58) tells us that if both ϵ and μ simultaneously cross zero, the impedance will remain finite. Therefore, such a material would be able to impedance match with other materials (i.e., satisfy the condition $\eta_1 = \eta_2$) and attain $R = 0$. This is an expedient trait which makes such *epsilon-and-mu-near-zero* (EMNZ) materials very practical to use.

Another desirable quality of EMNZ materials is the possession of a finite group velocity, as opposed to ENZ and MNZ materials, which have vanishing group velocities when the imaginary part of epsilon tends towards zero [43, 35]. By contrast, the group velocity is finite in EMNZ materials, allowing for efficient transmission of information [45].

Dirac-cone metamaterials, a type of *photonic crystal*, are a prominent EMNZ material that can achieve the simultaneous zero-crossing of ϵ and μ. This photonic crystal can be constructed from a large selection of common dielectric materials. In Chapter 3, we investigate how Dirac-cone metamaterials achieve this simultaneous zero-crossing, and how we fabricate one for use in our experiment.

Chapter Three
Dirac-cone metamaterials

As discussed in Chapter 2, Dirac-cone metamaterials are EMNZ metamaterials, media which achieve a refractive index of zero via the simultaneous zero-crossing of the permittivity ϵ and permeability μ. The first such structure was experimentally realized at microwave frequencies in 2011, using a square array of aluminum oxide rods [51]. Shortly thereafter, in 2013, this was achieved for optical frequencies [52]. While achieving a zero-crossing of the permittivity is not too difficult, achieving a zero-crossing of the permeability is comparatively much harder, as magnetic responses are weak in the visible and infrared regimes for naturally occurring materials [53]. Satisfying this requirement, as well as simultaneously satisfying the permittivity zero-crossing requirement, is not a trivial task, and requires a medium whose construction is very specific to resolving this problem. In this chapter, we present the theory behind EMNZ materials, as well as describe the Dirac-cone zero-index materials used in this work. The theoretical material from Section 3.1 of this chapter is derived by following the methods outlined in [54].

3.1 Theory

To satisfy the permittivity and permeability zero-crossing requirements, we make use of a photonic crystal [55, 56]. In a conventional solid-state crystal, atoms or molecules are arranged periodically, forming a crystal lattice. However, in a photonic crystal, there are instead a periodic dielectric function $\epsilon(x, y, z)$ and periodic magnetic function $\mu(x, y, z)$. Such a periodic dielectric can induce a photonic band structure that dictates the allowed energies (i.e., operating wavelengths) for given modes of light propagating in the crystal. By shaping this band structure, we can achieve an effective simultaneous zero-crossing of ϵ and μ in the crystal on a macroscopic scale.

3.1.1 Photonic crystals and band structure

The band structure of photonic crystals originates from Maxwell's equations. We can represent Maxwell's equations in terms of only the electric and magnetic intensity fields $\mathbf{E}$ and $\mathbf{H}$. We also assume a nonmagnetic, non-charged, and current-free material as in Subsection 2.2.

In this case, Maxwell's equations are of the form:

$$\nabla \cdot [\epsilon(\mathbf{r})\mathbf{E}(\mathbf{r},t)] = 0, \tag{3.1}$$
$$\nabla \cdot [\mu(\mathbf{r})\mathbf{H}(\mathbf{r},t)] = 0, \tag{3.2}$$
$$\nabla \times \mathbf{E}(\mathbf{r},t) = -\mu_0\mu(\mathbf{r})\frac{\partial \mathbf{H}(\mathbf{r},t)}{\partial t}, \tag{3.3}$$
$$\nabla \times \mathbf{H}(\mathbf{r},t) = \epsilon_0\epsilon(\mathbf{r})\frac{\partial \mathbf{E}(\mathbf{r},t)}{\partial t} \tag{3.4}$$

where $\mathbf{r}$ is the spacial vector. Here, we have explicitly noted the dependence on time and position of the electric and magnetic intensity fields. Because Maxwell's equations are linear, we can separate the time and spatial dependence of the fields $\mathbf{E}(\mathbf{r},t)$ and $\mathbf{H}(\mathbf{r},t)$ by expanding them into a set of *harmonic modes* $\mathbf{E}(\mathbf{r})$ and $\mathbf{H}(\mathbf{r})$. These modes constitute spatial patterns of the fields. The dependence on time can simply be represented by a complex exponential, as in the previous chapter. We obtain expressions of the form:

$$\mathbf{E}(\mathbf{r},t) = \mathbf{E}(\mathbf{r})e^{-i\omega t}, \tag{3.5}$$
$$\mathbf{H}(\mathbf{r},t) = \mathbf{H}(\mathbf{r})e^{-i\omega t}. \tag{3.6}$$

We substitute these expressions into Maxwell's equations. When introduced into the scalar product equations Eq. (3.1) and Eq. (3.2), we obtain:

$$\nabla \cdot [\epsilon(\mathbf{r})\mathbf{E}(\mathbf{r})] = 0, \tag{3.7}$$
$$\nabla \cdot [\mu(\mathbf{r})\mathbf{H}(\mathbf{r})] = 0. \tag{3.8}$$

When introduced into Maxwell's curl equations Eq. (3.3) and Eq. (3.4), we obtain:

$$\nabla \times \mathbf{E}(\mathbf{r}) = i\omega\mu_0\mu(\mathbf{r})\mathbf{H}(\mathbf{r}), \tag{3.9}$$
$$\nabla \times \mathbf{H}(\mathbf{r}) = -i\omega\epsilon_0\epsilon(\mathbf{r})\mathbf{E}(\mathbf{r}). \tag{3.10}$$

From here, we can divide Eq. (3.10) by $\epsilon(\mathbf{r})$, take the curl of both sides of the resulting equation, and then into the resulting expression substitute Eq. (3.9). In the end, we obtain

$$\frac{1}{\mu(\mathbf{r})}\nabla \times \left(\frac{1}{\epsilon(\mathbf{r})}\nabla \times \mathbf{H}(\mathbf{r})\right) = \epsilon_0\mu_0\omega^2\mathbf{H}(\mathbf{r}). \tag{3.11}$$

This equation is known as the *master equation*, which alongside Eq. (3.8), allows us to solve for our harmonic mode $\mathbf{H}(\mathbf{r})$. For a given $\mu(\mathbf{r})$ and $\epsilon(\mathbf{r})$, we can find the allowed modes $\mathbf{H}(\mathbf{r})$ and the corresponding allowed eigenfrequencies for these modes ω. This is even easier when $\mu(\mathbf{r}) \approx 1$, such as in the case of silicon. The electric field can then be determined by using Eq. (3.9). While we here obtained an equation in terms of the magnetic intensity field, it is also possible to do this for the electric field by following the same procedure.

Let us now consider an infinitely long plane of glass as our medium (See Fig. 3.1a). This medium is invariant under translation in the xy-plane. In such a medium, it can be shown that the modes must have the form [54]:

$$\mathbf{H}_k(\mathbf{r}) = \mathbf{h}(z)e^{ik\rho}, \tag{3.12}$$

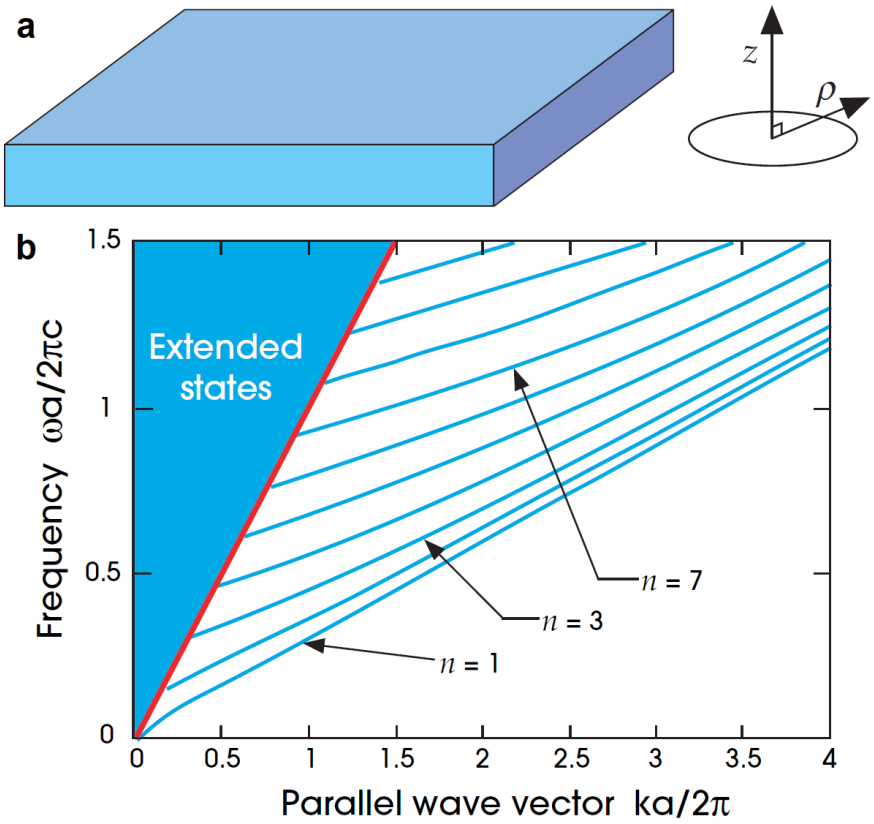

Figure 3.1 a) A plane of glass with thickness d, $\epsilon = 11.4$, and $\mu = 1$ stretching infinitely far in the xy-plane. b) The glass plane's corresponding photonic band structure when $\mathbf{H}$ is polarized perpendicular to z and k, computed using Eq. (3.11). The blue lines correspond to the allowed frequencies $\omega d/2\pi c$ for a given wave vector corresponding to a mode $kd/2\pi$. The red line is the *light line* $\omega = ck$, above which the extended states are not totally internally reflected and light escapes the material. Reproduced from [54].

known as *Bloch waves*. Here, ρ denotes a vector in the xy-plane, $\mathbf{h}(z)$ is a function denoting the modular dependence on z, and $k = k_x\hat{x}+k_y\hat{y}$ is the in-plane wave vector. In this equation, the modes can be classified by their value of k. However, they can also be classified by their *band number*, n. The band numbers line up the allowed modes and their respective wave vectors k in order of the increasing frequency values ω, which are determined for every mode by the master equation. Lining up the modes in this way results in what is known as the *band structure* of the material. In Fig. 3.1b, we show a computation of the band structure of our infinitely long plane of glass, assuming a thickness d, $\epsilon = 11.4$, and $\mu = 1$ [54]. When a certain set of frequencies is not allowed for any mode, the material is said to have a *bandgap* for this set of frequencies (not pictured here).

3.1.2 Dirac-cone waveguides

In a periodic structure, the Brillouin zone is defined as the set of points in the reciprocal lattice (k-space, as opposed to a spatial lattice) which are closest to $k = 0$. In a 2-dimensional square lattice, three points of interest can be defined within the Brillouin zone: the Γ-point, χ-point (not to be confused with the nonlinear susceptibility), and M-point. The coordinates of these points in a periodic square lattice with separation a are (0,0) for the Γ-point, ($\frac{\pi}{a}$,0) for the χ-point, and ($\frac{\pi}{a}$,$\frac{\pi}{a}$) for the M-point. These coordinates can be seen in Fig. 3.2, and define the center, the edge, and the corner of the unit cell respectively. Usually, most interesting phenomena in the photonic band structure of a material occur at these three points. As the Γ-point is located at (0,0) in momentum space, this means that $n = 0$ at this point due to the relation $k = 2\pi n/\lambda$. As a result, a zero-index material must operate at this point in momentum space.

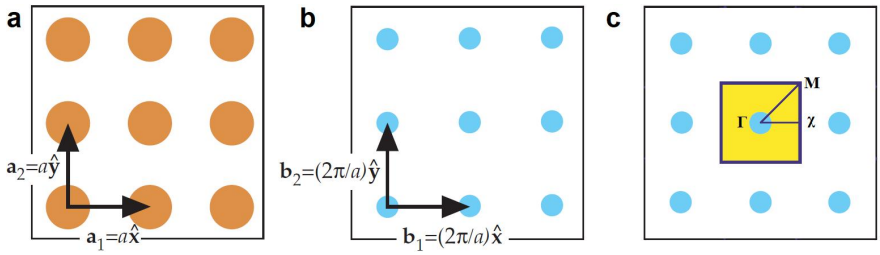

Figure 3.2 a) A periodic spatial, two-dimensional square lattice of dielectric pillars with separation a, and b) its corresponding reciprocal lattice. The Brillouin zone is shown in c), in addition to the location of the Γ-, χ-, and M-points. Adapted from [54].

We can expand upon the above example of an infinitely long plane of glass by considering an infinitely long slab of silicon, perforated by a square array of holes. We give this slab a height of 220 nm, a pitch of $a = 728$ nm, and a radius of $r = 222$ nm for the unit cell (See Fig. 3.3a,b). This structure again possesses translational symmetry, though in this case, it is discrete as opposed to continuous. Analogously to how the band structure was calculated in the plane of glass as a function of the wave vectors of the modes k, we can calculate the band structure of this perforated silicon slab as a function of the position in the Brillouin zone of the modes in k-space. We calculate the bands for a transverse-electric polarization, defined as when the electric field is confined to the xy-plane. The computation of the band structure can be seen in Fig. 3.3c. In the perforated slab, the lowest order solutions are a quadrupole mode and two dipole modes. In the quadrupole mode, two positive and two negative components of the field are arranged on the four sides of the unit cell, while the dipole mode has one positive and one negative component of the field on each side of its unit cell (See Fig. 3.3d). The band structure contains the bands corresponding to these three modes. For the perforated silicon slab, we observe that at the Γ-point of the Brillouin zone, the three bands intersect. The intersection of the top and bottom bands in this manner is what is known as a **Dirac cone**. Achieving such a Dirac cone in the band structure of this lattice is what enables the permittivity and permeability to simultaneously cross zero [51, 57, 58, 59, 60]. A Dirac cone for a similar structure can be seen in Fig. 3.3e, here in a 3D

plot as a function of k_x and k_y.

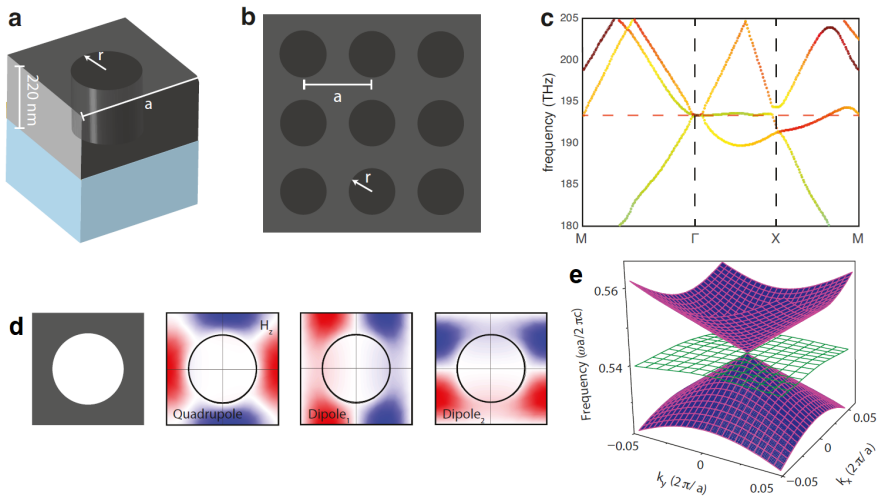

Figure 3.3 a) Unit cell of a square lattice where air cylinders are inserted into an infinite slab of silicon sitting on glass (a silicon-on-insulator platform), with a pitch a and radius r. b) Representation of 9 unit cells in the silicon slab. c) Band structure of the perforated silicon slab, with the bands of its 3 lowest order modes spanning the Γ-, χ-, and M-points. At the Γ-point, these bands intersect. d) Representation of the three lowest-order modes whose band structure is given in c). Blue symbolizes a region where the electric field is negative, while red symbolizes a region where the electric field is positive. There is one quadrupole mode and two dipole modes. e) Graphical representation of a Dirac cone as a function of k_x and k_y for a similar photonic crystal used in [51]. Adapted from [61, 51]

When these modes do not intersect to form a Dirac cone as in Fig. 3.4a, the permittivity ϵ and permeability μ do not simultaneously cross zero. Instead, in the region of the bandgap between the two modes, we obtain a positive permittivity and a negative permeability or vice versa (Fig. 3.4b). As per Eq. (2.58), this results in an imaginary refractive index, plotted in Fig. 3.4c. While it would appear that this would allow for a continuous real refractive index of zero in this region, this also results in very high losses and a diverging group velocity in the region of the bandgap, as plotted in Fig. 3.4d. On the contrary, in the case where these bands intersect, ϵ and μ simultaneously cross zero, resulting in a much smaller imaginary refractive index and a finite group index (Fig. 3.4e – h).

The waveguide used in this thesis is similar to the structure just explored. However, instead of an infinite 2D-array, it consists of a line of single unit cells, shown in Fig. 3.5a. For the one-dimensional analog, the Dirac cone becomes a pair of two bands, corresponding to a dipole and quadrupole mode shown in Fig. 3.5b, and the central band, corresponding to the longitudinal dipole mode, is no longer present. When using parameters of $a = 760$ nm for the pitch and $r = 212$ nm for the radius in simulations, we can again form a Dirac cone with these 2 bands [62, 61].

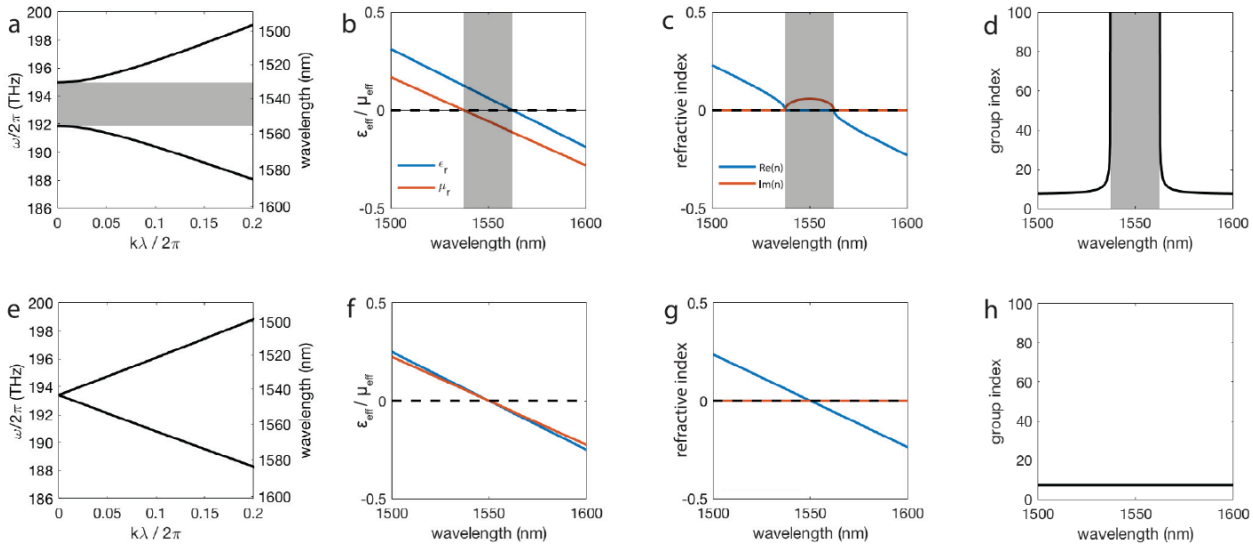

Figure 3.4 a) A bandgap between the quadrupole and dipole modes results in b) the permittivity ϵ and permeability μ not crossing zero at the same wavelength. This results in c) an imaginary refractive index and d) an infinite group index, with a resulting null group velocity. The bandgap region is shown in grey. e) A Dirac cone unison of the quadrupole and dipole modes results in f) the permittivity ϵ and permeability μ crossing zero at the same wavelength. This results in g) a finite refractive index and h) a finite group index, with a resulting non-diverging group velocity. Adapted from [45].

3.2 Fabrication and characterization

To fabricate the waveguides used in this experiment, a pattern is written using electron-beam lithography into a negative-tone resist. We subsequently apply this pattern to a silicon substrate using inductively-coupled plasma reactive ion etching [21, 61]. On either side of the waveguide, we also etch a photonic-band-gap material (PBG). These PBG materials are not necessary to shape the refractive index profile; however, they help confine light into the waveguide and as a result minimize losses. The PBG materials are also photonic crystals, and are designed such that they possess a bandgap at the zero-index wavelength of the zero-index waveguide. As the waveguides are designed to work in the near-infrared (NIR), the bandgap of the PBG materials occurs in this region. Due to the bandgap, the PBG materials reflect light in this spectral region back into the waveguide. As light coupling out of the zero-index waveguide does so at 90° (see Subsection 2.3.1), the PBG material is placed at a distance from the waveguide corresponding to a 2π phase shift. This cancels out exiting radiation while maintaining an effective phase advance of zero. More information on the PBG materials can be found in [61]. To facilitate coupling into the waveguides with free-space beams, polymer coupling pads with large cross-sectional areas are constructed on the ends of the waveguide. These polymer pads are used to couple into silicon waveguides, which then lead to the zero-index waveguides. While the waveguides used here are constructed from silicon, it must be noted that Dirac-cone zero-index materials can be constructed from any

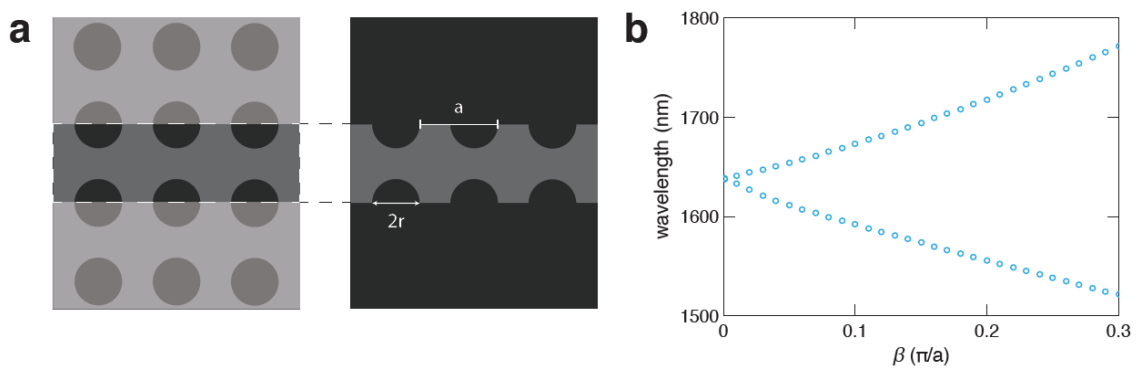

Figure 3.5 a) The one-dimensional equivalent of a silicon slab with a square array of air holes, with a pitch a and radius r. It consists of an infinite line of unit cells, each containing a partial hole on each side. b) The band structure of this material as a function of the propagation constant $\beta = \frac{2\pi n_{\text{eff}}}{\lambda}$, where n_{eff} is the effective refractive index. The two bands intersect at the Γ-point ($\beta = 0$).

base material. Here, we have used silicon for the simplicity of fabrication. However, any material, including materials with a larger $\chi^{(3)}$, can be used in the fabrication process. The size of the device can also be scaled such that the zero-index wavelength occurs wherever desired. Here, we use 1600 nm, as it is located within a range of frequencies of interest in the telecommunications industry [63].

The waveguides consist of a 1D row of zero-index Dirac-cone metamaterial. The parameters used were a lattice constant of $a = 728$ nm and a cylindrical hole of radius $r = 222$ nm. These parameters were selected due to simulations indicating they result in a perfect modal degeneracy at 1550 nm [62]. However, due to fabrication imperfections, the zero-index wavelengths are located at slightly longer wavelengths [62, 61]. This fluctuation is within the expected fabrication tolerances of electron-beam lithography [61]. The ridge silicon waveguides that lead to and from the zero-index waveguide are 500 nm wide by 220 nm thick, and are designed such that they have normal dispersion and as a result do not generate any FWM [21]. Identically to the perforated silicon slab, the zero-index waveguides operate using a transverse-electric polarization. Two zero-index waveguides are used: a waveguide with a length 14.8 µm and a zero-index wavelength of 1600 nm, and a zero-index waveguide with a length of 11.1 µm and a zero-index wavelength of 1625 nm. The refractive index and loss profiles of the waveguide crossing at 1600 nm can be seen in Fig. 3.7a,b. When the wavelength is longer than 1600 nm, the refractive index is negative, while when it is shorter than 1600 nm, the refractive index is positive. While the loss of the waveguides used in the experiment has not been measured, the loss curve is adapted from a similar waveguide [21]. As the modes of the zero-index waveguide operate above the light line, losses in this waveguide are quite high, peaking shortly before the zero-index wavelength at 1 dB/µm. These waveguides possess low and anomalous dispersion, plotted in Fig. 3.7c. This dispersion allows us to phase-match for a large variety of wavelengths [27]. The waveguide also has a wavelength-dependent quantity μ/n, which is proportional to the impedance, plotted in Fig. 3.7d. In subsequent analysis, we will use these data sets to model phase matching in these zero-index waveguides.

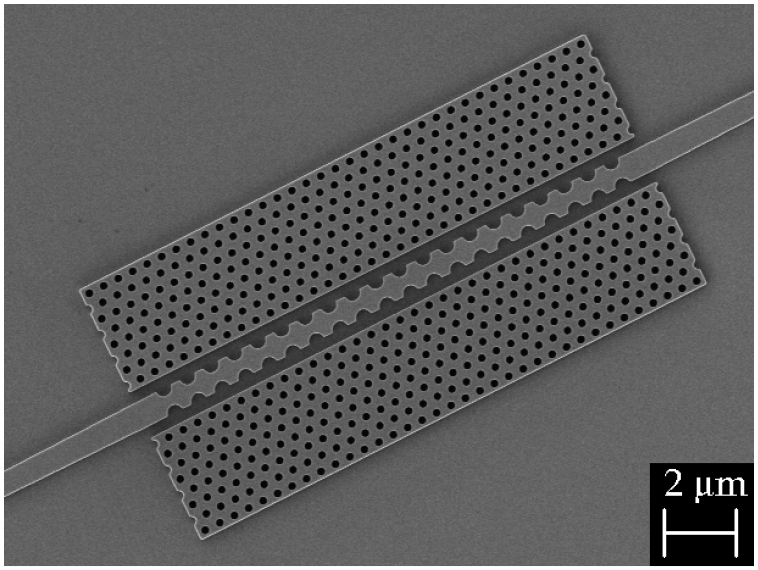

Figure 3.6 Scanning electron microscope image of a 14.8 µm long Dirac-cone zero-index waveguide. A PBG material is located on either side of the waveguide to aid in the confinement of light. A regular silicon waveguide is located on both ends of the zero-index waveguide to facilitate coupling into it.

Fabrication in this work was performed in part at the Center for Nanoscale Systems (CNS), a member of the National Nanotechnology Coordinated Infrastructure Network (NNCI), which is supported by the National Science Foundation under NSF award no. 1541959. CNS is part of Harvard University.

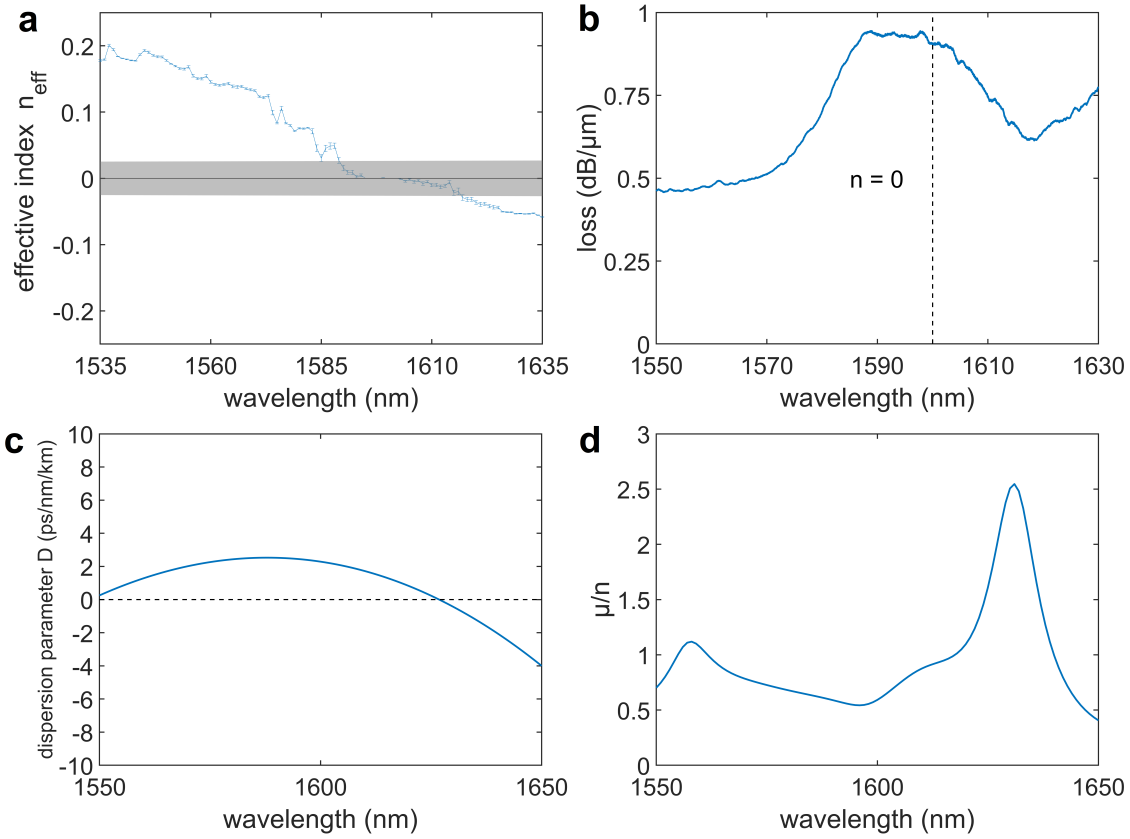

Figure 3.7 a) Refractive index profile of one of the waveguides used in our experiment, which has its zero-index wavelength at roughly 1600 nm. The error bars are determined by repeating the measurement of each data point 50 times. The region shaded in grey delineates a region where the method used to determine the refractive index [21] is no longer reliable. However, it is known that the magnitude of the refractive index is below 0.02 throughout this region. b) Loss profile of a similar waveguide in dB/μm. The loss peaks shortly below the zero-index wavelength (dashed black line). c) Simulated dispersion parameter D of a similar waveguide as a function of wavelength. D is positive, corresponding to anomalous dispersion over the 80 nm surrounding the zero-index wavelength. d) Simulated μ/n, a quantity proportional to the impedance, plotted as a function of wavelength (Eq. 2.58). As μ is the relative permeability, μ/n is dimensionless.

Chapter Four

Model for phase matching in a FWM process

In Chapter 2, we derived the coupled-amplitude equations for a standard FWM process, where all beams were co-propagating. We also investigated the resulting phase-matching condition and its effect on the growth of the generated idler wave. In this chapter, we will do the same using other beam configurations. In particular, we will treat the generation of idler waves that are forward-propagating and backward-propagating with respect to the pump beam in a waveguide when all constituent waves are collinear. This encompasses the cases of co- and counter-propagating pump and signal beams. We will additionally investigate how these geometries are affected in the case of a medium with loss. Finally, we will examine the case of a signal beam coupling into the waveguide from outside the beam plane, as well as the more general case of phase matching with an arbitrary beam configuration.

4.1 Phase matching with co-propagating pump and signal beams

In this section, we will investigate the generation of a forward- and backward-propagating idler wave when using co-propagating pump and signal beams, as depicted in Fig. 4.1. In this thesis, whenever we state something is forward- or backward-propagating, we are referring to the direction with respect to the pump beam. In the lossless forward-propagating case, this derivation is identical to the derivation in Subsection 2.2.1. However, when the idler wave is backward-propagating, the initial conditions of our derivation as outlined in Subsection 2.2.1 undergo an important alteration to account for the idler wave's new orientation. As opposed to the prior derivation, where the electric field of the idler wave possessed a positive momentum term k_i, a backward-propagating beam, will possess a negative momentum $-k_i$, changing sign due to the idler wave's new orientation:

$$\mathbf{E}_i(z,t) = A_i e^{i(-k_i z - \omega_i t)} + c.c. \tag{4.1}$$

The subsequent derivation is otherwise identical and the ultimate result is nearly identical to the one previously obtained in Subsection 2.2.2:

$$|A_i|^2 = \frac{9{\mu_i}^2{\chi^{(3)}}^2\omega_i^2}{4n_i^2c^2}|A_p|^4|A_s|^2L^2\,\mathrm{sinc}^2\left(\Delta k_b L/2\right). \tag{4.2}$$

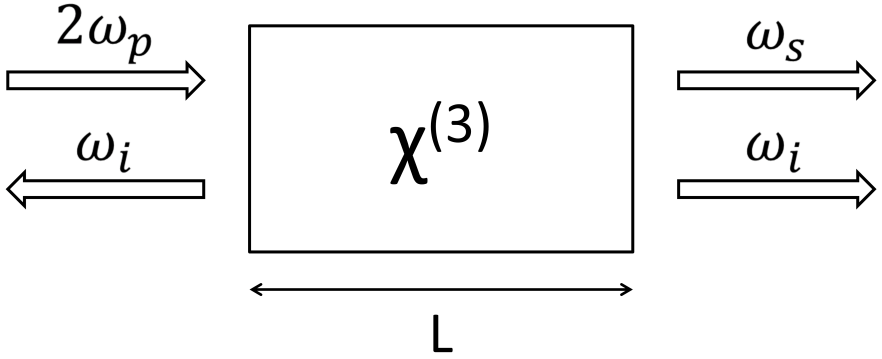

Figure 4.1 Schematic of a FWM process with co-propagating beams in a nonlinear medium with $\chi^{(3)}$ of length L. In contrast to the derivation in Subsection 2.2.1, an idler wave is generated in both the forward- and backward-propagating directions.

While the final result appears identical, the critically important difference lies in the phase-matching condition Δk. As opposed to a forward-propagating idler wave, where the phase-matching condition is given by $\Delta k_{\mathrm{f}} = 2k_p - k_s - k_i$, the backward-propagating idler wave possesses the phase-matching condition

$$\Delta k_{\mathrm{b}} = 2k_p - k_s + k_i. \tag{4.3}$$

In Eq. (4.3), the sign of the idler momentum is *positive*, as opposed to negative. This is due to the inverted orientation of the idler beam.

To investigate the consequences arising from the difference between the forward and backward phase-matching conditions, we can imagine a FWM interaction where the pump, signal, and idler waves are all very close to one another, i.e. $\lambda_p \approx \lambda_s \approx \lambda_i$. In this case, the momentum of all of the waves is approximately equal to a single value k ($k = k_p = k_s = k_i$). With this approximation, the phase-matching conditions for forward- and backward-propagating idler waves are equal to

$$\Delta k_{\mathrm{f}} = 2k - k - k = 0, \tag{4.4}$$
$$\Delta k_{\mathrm{b}} = 2k - k + k = 2k \tag{4.5}$$

and the forward-propagating idler light will be phase-matched, while the backward-propagating idler light will not be. This is the usual case for FWM interactions in standard nonlinear media with positive refractive indices. However, in the case where the idler wave is located at the zero-index wavelength, it has a vanishing momentum $k_i = 0$. Now, the phase-matching conditions for forward- and backward-propagating light will both be equal to

$$\Delta k_{\mathrm{f}} = 2k_p - k_s, \tag{4.6}$$
$$\Delta k_{\mathrm{b}} = 2k_p - k_s. \tag{4.7}$$

When $k_i = 0$, the phase-matching conditions for forward- and backward-propagating idler waves become identical. This suggests that when the idler wavelength is localized at the wavelength where $n = 0$, a backward-propagating idler wave should be just as well phase-matched as a forward-propagating idler wave. If we also have a situation where $k_s = 2k_p$

(as is the case in our waveguide, as well as any low-dispersion zero-index medium), we will have achieved simultaneous phase matching of the forward- and backward-propagating idler waves.

Using the refractive index profile of our Dirac-cone zero-index waveguide with a zero-index wavelength of 1600 nm shown in Fig. 3.7, we can find the coherence length L_{coh} of forward- and backward-propagating idler waves as a function of the pump and signal wavelengths to judge the quality of phase matching in both of these interactions. To compare how this waveguide fares in comparison to a standard silicon ridge waveguide, we also plot the coherence length of forward- and backward-propagating idler waves in such a waveguide for comparison. The obtained coherence lengths are shown in Fig. 4.2.

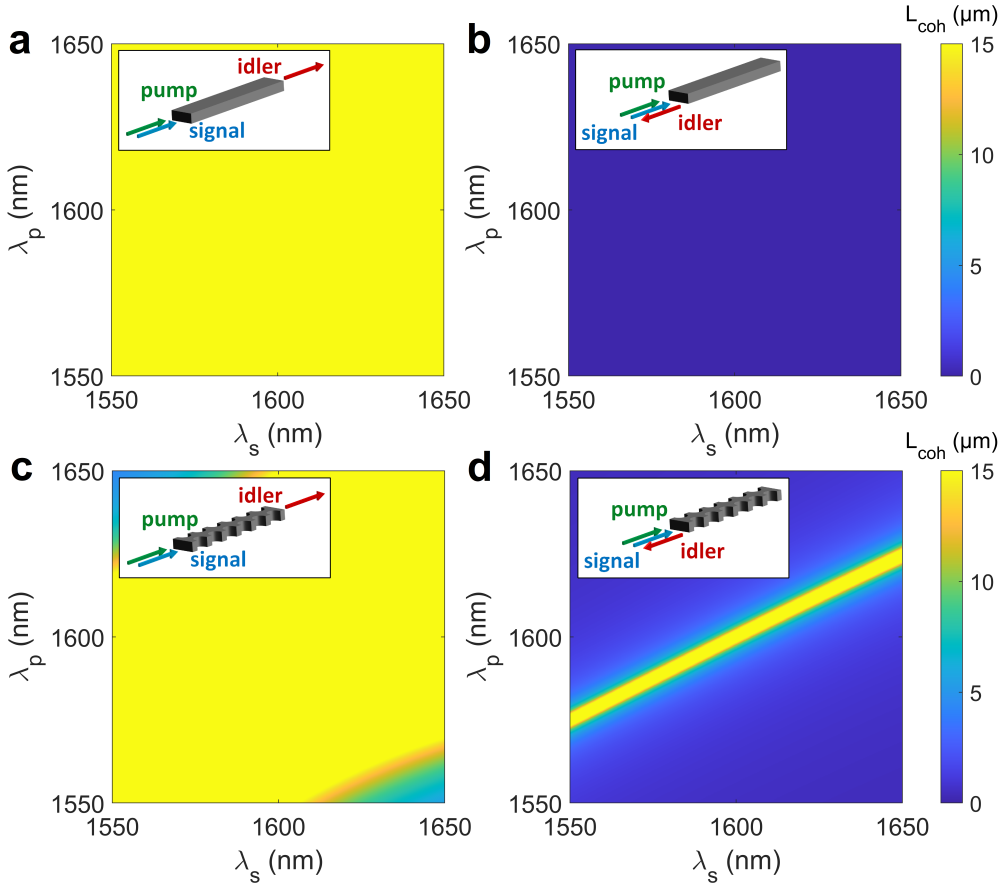

Figure 4.2 Numerical predictions of the coherence length, calculated using Eq. 2.49, for a) forward- and b) backward-propagating idler waves in a standard silicon ridge waveguide with co-propagating pump and signal beams, and c) forward- and d) backward-propagating idler waves in a zero-index waveguide with the same configuration. L_{coh} is plotted as a function of the pump wavelength λ_p and the signal wavelength λ_s. Bright yellow indicates a region where the coherence length exceeds 15 μm, the length of the zero-index waveguide studied.

We see that in the case of a standard silicon waveguide, the forward-propagating idler wave is always well phase-matched over the spectrum of interest. This is due to the low and

anomalous dispersion profile of the waveguides, which permits phase matching to occur [27]. In contrast, a backward-propagating idler wave is never phase-matched. In the case of a zero-index waveguide, the forward-propagating idler wave remains phase-matched due to the same low and anomalous dispersion profile, with any variance arising only as a result of a difference in dispersion. However, in contrast to the standard waveguide, the backward-propagating idler wave is phase-matched when it lies on a particular curve. This particular phase-matching curve in the backward-propagating idler wave plot corresponds to the idler wave being located at the zero-index wavelength. This result supports our prediction that, when the idler wave is located at the zero-index wavelength, the phase-matching conditions for the forward- and backward-propagating idler waves become identical, and that at this wavelength, the idler's orientation becomes inconsequential to phase-matching considerations. Furthermore, as we can see in Fig. 3.7, we also have $k_s \approx 2k_p$ in this region, meaning that beyond the phase-matching conditions being identical, they are also near zero.

4.1.1 Co-propagating pump and signal beams in lossy media

While the coherence length provides us with some strong intuition as to when an interaction is phase-matched, it is alone insufficient to predict the generated power of a nonlinear process when radiative losses are taken into account. For example, consider a material with a wavelength-dependent loss profile that features a significant loss peak. One would not expect a generated idler wave to be particularly powerful at the spectral location of that peak, regardless of phase-matching considerations. Therefore, to adequately analyze experimental results, we require a model that takes losses into account.

We derive this model just as in Chapter 2, by solving the wave equation for each component of the field and obtaining the coupled-amplitude equations. However, in the final result, we add a loss term to account for amplitude depletion as the waves propagate through the waveguide. For a forward-propagating idler wave, these new coupled-amplitude equations take the form:

$$\frac{dA_p}{dz} = \frac{3i\mu_p\chi^{(3)}\omega_p}{2n_pc}A_p^*A_sA_ie^{-i\Delta k_{\mathrm{f}}z} - \alpha_pA_p, \tag{4.8}$$

$$\frac{dA_s}{dz} = \frac{3i\mu_s\chi^{(3)}\omega_s}{2n_sc}A_p^2A_i^*e^{i\Delta k_{\mathrm{f}}z} - \alpha_sA_s, \tag{4.9}$$

$$\frac{dA_i}{dz} = \frac{3i\mu_i\chi^{(3)}\omega_i}{2n_ic}A_p^2A_s^*e^{i\Delta k_{\mathrm{f}}z} - \alpha_iA_i. \tag{4.10}$$

Here, α is the *propagation loss*, which dictates how rapidly a wave decreases in amplitude. We again use p, s, and i as subscripts to denote the pump, signal, and idler waves, and $\Delta k_{\mathrm{f}} = 2k_p - k_s - k_i$. Note that, in this derivation, we have again used the slowly varying amplitude approximation, and ignored the second derivative of A_i. One can obtain the parameter α from the propagation loss in dB/µm in Fig. 3.7b by converting it to meters and using the formula [63]

$$\alpha_{1/\mathrm{m}} = \frac{\ln 10}{20}\alpha_{\mathrm{dB/m}}. \tag{4.11}$$

Unlike in Chapter 2, we here cannot apply the undepleted pump approximation, as it evidently does not hold: the amplitudes are subject to losses and therefore cannot be treated as constant. This means that there is no closed analytic solution, and that the coupled-amplitude equations must be solved numerically. However, we are here able to use a relaxed version of the undepleted pump approximation, which we name the *nonlinearly undepleted pump approximation*. This approximation states that while the amplitude of the pump and signal waves are not constant, they are only ever subject to radiative losses. In other words, this approximation states that the fraction of the pump and signal waves converted into the idler wave and vice versa is very small, and may be neglected. Our approximation can be justified in our experiment, as the generated idler is always approximately four orders of magnitude less powerful than the pump beam. Using this approximation, we can reduce Eqs. (4.8-4.10) to the form

$$\frac{dA_p}{dz} = -\alpha_p A_p, \tag{4.12}$$

$$\frac{dA_s}{dz} = -\alpha_s A_s, \tag{4.13}$$

$$\frac{dA_i}{dz} = \frac{3i\mu_i\chi^{(3)}\omega_i}{2n_i c} A_p^2 A_s^* e^{i\Delta k_{\mathrm{f}} z} - \alpha_i A_i, \tag{4.14}$$

where the nonlinear terms for the pump and signal waves are no longer taken into account. These equations, as opposed to the previous ones, *do* possess an analytical solution. This is because, having made this approximation, the pump and signal equations are no longer coupled to any amplitude but their own. To solve these equations, we can first solve Eqs. (4.12) and (4.13) to obtain an expression for the pump and signal wave amplitudes as a function of z. To do this, we can simply reorganize the amplitude terms on one side:

$$\frac{1}{A_p} dA_p = -\alpha_p dz, \tag{4.15}$$

$$\frac{1}{A_s} dA_s = -\alpha_s dz \tag{4.16}$$

and thereafter integrate this expression on both sides to obtain

$$A_p(z) = A_{\mathrm{p0}} e^{-\alpha_p z}, \tag{4.17}$$

$$A_s(z) = A_{\mathrm{s0}} e^{-\alpha_s z} \tag{4.18}$$

where A_{p0} and A_{p0} are the initial amplitudes of the pump and signal waves, obtained by finding the integration constants by using the initial conditions $A_p(0) = A_{\mathrm{p0}}$ and $A_s(0) = A_{\mathrm{s0}}$. Now, we can substitute these expressions into Eq. (4.14) to obtain

$$\frac{dA_i}{dz} = \frac{3i\mu_i\chi^{(3)}\omega_i}{2n_i c} A_{\mathrm{p0}}^2 A_{\mathrm{s0}}^* e^{i\Delta k_{\mathrm{f}} z} e^{-\Delta\alpha z} - \alpha_i A_i \tag{4.19}$$

where we have defined $\Delta\alpha \equiv 2a_p + a_s$. We are now left with a single linear differential equation which can be solved. For simplicity, we can rewrite Eq. (4.19) by placing the terms

which do not depend on z under the variable

$$\Omega \equiv \frac{3\mu_i \chi^{(3)} \omega_i}{2n_i c} A_{\mathrm{p0}}^2 A_{\mathrm{s0}}^* \tag{4.20}$$

and reorganize the terms of Eq. (4.19) so that

$$\frac{dA_i}{dz} + \alpha_i A_i = i\Omega e^{(i\Delta k_{\mathrm{f}} - \Delta\alpha)z}. \tag{4.21}$$

This expression can be solved by multiplying both sides by $e^{\alpha_i z}$. Having multiplied by this factor, the left side, by virtue of the chain rule, can be expressed as

$$\frac{d(A_i e^{\alpha_i z})}{dz} = i\Omega e^{(i\Delta k_{\mathrm{f}} - \Delta\alpha)z}. \tag{4.22}$$

We can then integrate on both sides of this equation to obtain

$$A_i e^{\alpha_i z} = \frac{i\Omega e^{(i\Delta k_{\mathrm{f}} - \Delta\alpha + \alpha_i)z}}{i\Delta k_{\mathrm{f}} - \Delta\alpha + \alpha_i} + C, \tag{4.23}$$

where C is the integration constant. From this point, we can find the value of C by using the initial condition $A_i(0) = 0$, and find that

$$C = \frac{-i\Omega}{i\Delta k_{\mathrm{f}} - \Delta\alpha + \alpha_i}. \tag{4.24}$$

When we substitute this value into Eq. (4.23), we obtain the final expression for the idler wave amplitude as a function of z

$$A_i(z) = \frac{i\Omega(e^{(i\Delta k_{\mathrm{f}} - \Delta\alpha)z} - e^{-\alpha_i z})}{i\Delta k_{\mathrm{f}} - \Delta\alpha + \alpha_i} \tag{4.25}$$

$$= \frac{3i\mu_i \chi^{(3)} \omega_i}{2n_i c} A_{\mathrm{p0}}^2 A_{\mathrm{s0}}^* \left(\frac{e^{(i\Delta k_{\mathrm{f}} - \Delta\alpha)z} - e^{-\alpha_i z}}{i\Delta k_{\mathrm{f}} - \Delta\alpha + \alpha_i} \right). \tag{4.26}$$

This equation completely describes the forward-generated idler wave, and can be used to calculate its power as a function of the propagated length z in the waveguide.

We can follow an analogous procedure to obtain the expression for a backward-propagating idler wave. As in the lossless case, beginning our derivation from the wave equation yields the phase-matching condition $\Delta k_{\mathrm{b}} = 2k_p - k_s + k_i$. As before, the idler wave begins building at $z = 0$, and is detected at $z = L$. However, as the idler wave is counter-propagating against the pump and signal, we instead arrange for our pump and signal waves to begin at $z = L$. This effectively inverts the frame of reference of the waveguide. To symbolically represent a wave that begins at $z = L$, say the pump wave, we cause the wave to begin at $z = 0$ with an amplitude $A_p e^{-\alpha_p L}$. We then increase the amplitude throughout the waveguide, such that it ends with an amplitude A (Fig. 4.3). In cases where the nonlinearly undepleted pump approximation holds, this approach of inverting the waveguide is always theoretically valid.

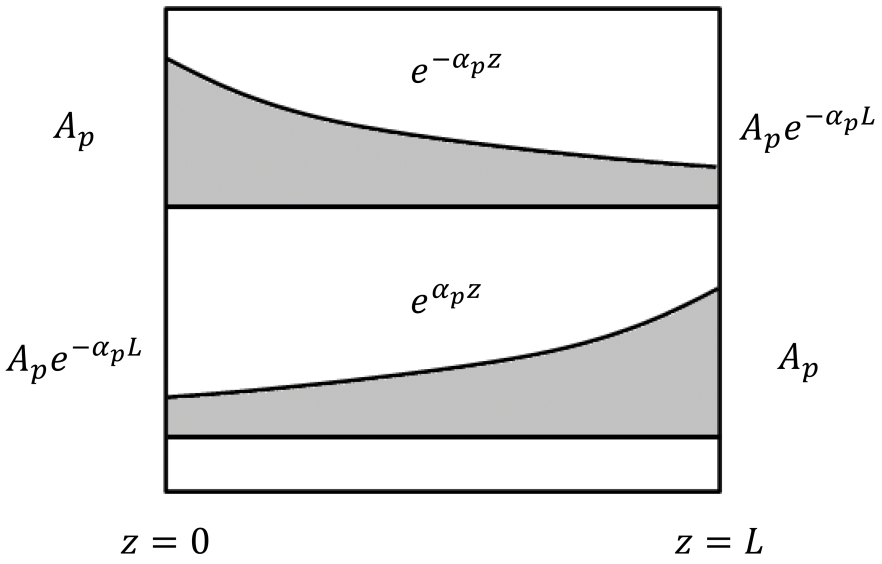

Figure 4.3 A pump wave propagating from $z = 0$ to $z = L$ is represented by a wave with an initial amplitude A_p that suffers loss $e^{-\alpha_p z}$ as it propagates through the waveguide, exiting it with an amplitude $A_p e^{-\alpha_p L}$. To represent this same wave as propagating from $z = L$ to $z = 0$, we define the wave as beginning with amplitude $A_p e^{-\alpha_p L}$, and increasing in amplitude as it travels through the waveguide, exiting with final amplitude A_p. We also appropriately invert the momentum k_p of the pump wave.

Having inverted the frame of reference, we also appropriately invert the signs of the pump, signal, and idler wave momentum terms. Under these assumptions, the coupled-amplitude equations take the form

$$\frac{dA_p}{dz} = \alpha_p A_p, \tag{4.27}$$

$$\frac{dA_s}{dz} = \alpha_s A_s, \tag{4.28}$$

$$\frac{dA_i}{dz} = \frac{3i\mu_i \chi^{(3)} \omega_i}{2n_i c} A_p^2 A_s^* e^{-i\Delta k_\mathrm{b} z} - \alpha_i A_i. \tag{4.29}$$

Note that the phase-matching term is now negative. Using the initial conditions $A_p(0) = A_{\mathrm{p}0} e^{-\alpha_p L}$ and $A_s(0) = A_{\mathrm{s}0} e^{-\alpha_s L}$, we can obtain the pump and signal amplitudes as a function of z just as in the forward-propagating case, obtaining

$$A_p(z) = A_{\mathrm{p}0} e^{-\alpha_p L} e^{\alpha_p z}, \tag{4.30}$$

$$A_s(z) = A_{\mathrm{s}0} e^{-\alpha_s L} e^{\alpha_s z}. \tag{4.31}$$

By substituting these expressions for the pump and signal wave amplitudes into Eq. (4.29), and subsequently solving the resulting linear differential equation, we obtain the result

$$A_i(z) = \frac{3i\mu_i \chi^{(3)} \omega_i}{2n_i c} A_{\mathrm{p}0}^2 A_{\mathrm{s}0}^* e^{-(2\alpha_p + \alpha_s)L} \left(\frac{e^{(\Delta\alpha - i\Delta k_\mathrm{b})z} - e^{-\alpha_i z}}{\Delta\alpha - i\Delta k_\mathrm{b} + \alpha_i} \right). \tag{4.32}$$

We later use Eqs. (4.26) and (4.32) to analyze our experimental results in Chapter 5. In both cases, we can easily convert the idler wave amplitudes to powers using Eq. (2.43). In the power equation, we use the refractive index of the surrounding silicon waveguide, and not that of the zero-index waveguide. We also simply assume S to be 1, as we normalize the results to unity and its value is inconsequential.

4.2 Phase matching with counter-propagating pump and signal beams

Having treated the configuration of co-propagating pump and signal beams in a FWM interaction, we can now look at the case of counter-propagating pump and signal beams (Fig. 4.4). Similarly to how treating a backward-propagating idler wave led us to invert the sign of the idler wave's momentum in the previous subsection, we can here model a counter-propagating beam arrangement by inverting the sign of the signal wave's momentum. The plane wave equation for the signal beam now becomes

$$\mathbf{E}_s(z,t) = A_s e^{i(-k_s z - \omega_s t)} + c.c. \tag{4.33}$$

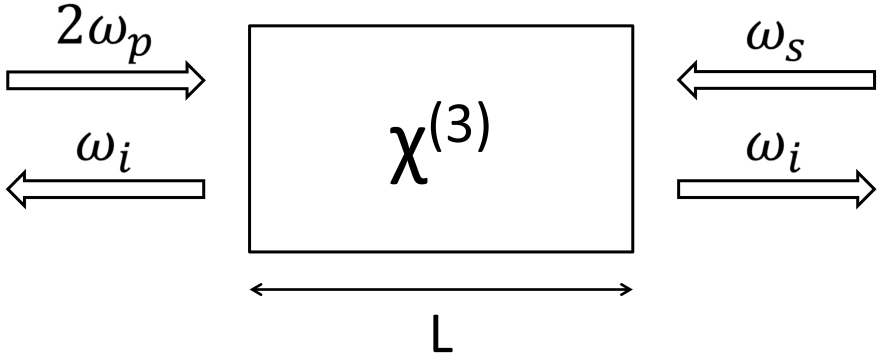

Figure 4.4 Schematic of a FWM process with counter-propagating beams in a nonlinear medium with $\chi^{(3)}$ of length L. An idler wave is generated in both the forward- and backward-propagating directions.

Just as in the previous subsection, this changes very little in the derivation for the idler amplitude equation. However, identically to how the phase-matching condition changed for a backward-propagating idler wave in the co-propagating pump and signal beam case, having a counter-propagating signal beam also changes the phase-matching condition. After performing the derivation, we end up with the final result

$$|A_i|^2 = \frac{9{\mu_i}^2{\chi^{(3)}}^2\omega_i^2}{4n_i^2c^2}|A_p|^4|A_s|^2L^2\,\mathrm{sinc}^2\left(\Delta k_{\mathrm{f/b}}L/2\right), \tag{4.34}$$

$$\Delta k_{\mathrm{f}} = 2k_p + k_s - k_i, \tag{4.35}$$

$$\Delta k_{\mathrm{b}} = 2k_p + k_s + k_i, \tag{4.36}$$

where the subscripts f and b again denote forward- and backward-propagating idler waves. We see that by making the signal beam counter-propagating, we have again altered the phase-matching condition by inverting the sign of the signal wave's momentum. Just as we did in the case of co-propagating beams, we can now again plot the coherence lengths L_{coh} for counter-propagating beams using the refractive index data of our zero-index silicon waveguide. We plot the coherence length for a forward- and a backward-propagating idler wave resulting from counter-propagating pump and signal beams. The calculated coherence lengths can be seen in Fig. 4.5.

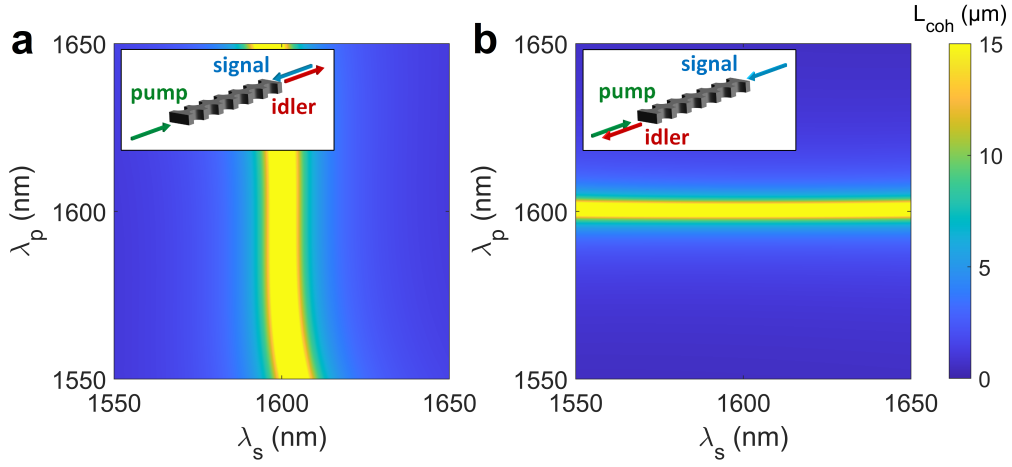

Figure 4.5 Numerical predictions of the coherence length, calculated using Eq. 2.49, for a) forward- and b) backward-generated idler waves in a zero-index waveguide with counter-propagating pump and signal beams. L_{coh} is plotted as a function of the pump wavelength λ_p and the signal wavelength λ_s. Bright yellow indicates a region where the coherence length exceeds 15 µm, the length of the zero-index waveguide studied.

The coherence length calculations for counter-propagating beams reveal that for a forward-propagating idler wave, the FWM interaction will remain coherent as long as the signal beam is located at the zero-index wavelength. On the other hand, a backward-propagating idler wave will remain coherent as long as the pump beam is located at the zero-index wavelength. This is similar to the result for a backward-propagating idler wave with co-propagating pump and signal beams, where the interaction remained coherent as long as the idler wave was located at the zero-index wavelength. This is because in all of these cases, eliminating the momentum contribution of those waves restores the phase-matching condition, just as in the situation investigated in Section 2.3.2. This phenomenon is investigated in greater detail in Subsection 4.3.2.

4.2.1 Counter-propagating pump and signal beams in lossy media

While the calculated coherence lengths for a FWM interaction with counter-propagating pump and signal beams provide us valuable insight, their use is again limited when treating the case of a lossy medium. This is especially true of counter-propagating beams. In an

interaction with co-propagating pump and signal beams, the pump and signal waves have the benefit of possessing a large power overlap between them. However, when the beams are counter-propagating, the pump and signal waves will both be the most powerful on their respective ends of the waveguide, and gradually deplete as they move towards the opposing facets. This means that the strongest portion of the pump wave intersects with the weakest portion of the signal wave, and vice versa. As a result, the power overlap is not nearly as large, and whatever overlap that is present is greatly dictated by the loss of the waveguide. Therefore, it is critical even more so in the case of counter-propagating pump and signal beams to develop a model that takes radiative losses into account. Our method to derive a model is largely identical to the method used for co-propagating pump and signal beams. For a forward-propagating idler wave, we have the coupled-amplitude equations

$$\frac{dA_p}{dz} = -\alpha_p A_p, \tag{4.37}$$

$$\frac{dA_s}{dz} = \alpha_s A_s, \tag{4.38}$$

$$\frac{dA_i}{dz} = \frac{3i\mu_i\chi^{(3)}\omega_i}{2n_i c} A_p^2 A_s^* e^{i\Delta k_{\mathrm{f}} z} - \alpha_i A_i, \tag{4.39}$$

for which we have $\Delta k_{\mathrm{f}} = 2k_p + k_s - k_i$. Note that here, we have defined the signal wave as entering the waveguide at $z = L$, and exiting the waveguide at $z = 0$, just as previously. Using the initial conditions $A_p(0) = A_{\mathrm{p0}}$ and $A_s(0) = A_{\mathrm{s0}} e^{-\alpha_s L}$, we find the pump and signal amplitudes

$$A_p(z) = A_{\mathrm{p0}} e^{-\alpha_p z}, \tag{4.40}$$

$$A_s(z) = A_{\mathrm{s0}} e^{-\alpha_s L} e^{\alpha_s z}. \tag{4.41}$$

When these expressions are introduced into Eq. (4.39), we can solve and obtain the final expression for the forward-propagating idler wave amplitude as a function of z

$$A_i(z) = \frac{3i\mu_i\chi^{(3)}\omega_i}{2n_i c} A_{\mathrm{p0}}^2 A_{\mathrm{s0}}^* e^{-\alpha_s L} \left(\frac{e^{(i\Delta k_{\mathrm{f}} - \Delta\alpha)z} - e^{-\alpha_i z}}{i\Delta k_{\mathrm{f}} - \Delta\alpha + \alpha_i} \right). \tag{4.42}$$

Note that, in the counter-propagating pump and signal beam case, $\Delta\alpha = 2\alpha_p - \alpha_s$. In the case of a backward-propagating idler wave, we again use our method of inverting the waveguide such that the idler wave exits the waveguide at $z = L$. In this case, the coupled-amplitude equations take the form

$$\frac{dA_p}{dz} = \alpha_p A_p, \tag{4.43}$$

$$\frac{dA_s}{dz} = -\alpha_s A_s, \tag{4.44}$$

$$\frac{dA_i}{dz} = \frac{3i\mu_i\chi^{(3)}\omega_i}{2n_i c} A_p^2 A_s^* e^{-i\Delta k_{\mathrm{b}} z} - \alpha_i A_i, \tag{4.45}$$

for which we have $\Delta k_{\mathrm{b}} = 2k_p + k_s + k_i$. Using the initial conditions $A_p(0) = A_{\mathrm{p0}}e^{-\alpha_p L}$ and $A_s(0) = A_{\mathrm{s0}}$, we find the pump and signal amplitudes

$$A_p(z) = A_{\mathrm{p0}}e^{-\alpha_p L}e^{\alpha_p z}, \tag{4.46}$$
$$A_s(z) = A_{\mathrm{s0}}e^{-\alpha_s z}. \tag{4.47}$$

When these expressions are introduced into Eq. (4.39), we can solve and obtain the final expression for the backward-propagating idler wave amplitude as a function of z

$$A_i(z) = \frac{3i\mu_i\chi^{(3)}\omega_i}{2n_i c}A_{\mathrm{p0}}^2 A_{\mathrm{s0}}^* e^{-2\alpha_p L}\left(\frac{e^{(\Delta\alpha - i\Delta k_{\mathrm{b}})z} - e^{-\alpha_i z}}{\Delta\alpha - i\Delta k_{\mathrm{b}} + \alpha_i}\right). \tag{4.48}$$

4.3 Non-collinear beams

Up to this point, we have always treated the pump, signal, and idler beams as propagating on the same beam plane, whether they be co- or counter-propagating against one another. However, in this section, we treat the case of an orthogonal signal beam as in Fig. 4.6, and then generalize this for the case of an arbitrary beam configuration.

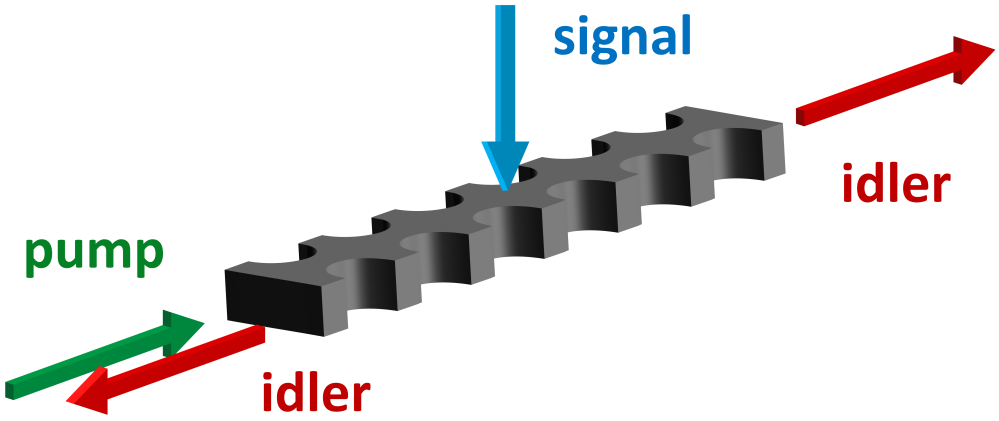

Figure 4.6 Beam configuration for a signal beam coupling into the zero-index waveguide orthogonal to the pump beam. From this configuration, forward- and backward-propagating idler waves are generated.

4.3.1 Orthogonal pump and signal beams

In previous sections, we began our analysis by considering the initial fields of the pump, signal, and idler beams, and then substituted these expressions into the wave equation to obtain differential equations that we could solve to make predictions. In the case of an orthogonal signal beam, this approach cannot be used, as it depends on the collinearity of the beams, and the signal beam cannot be as simply defined as in the collinear cases. However, we can make the reasonable assumption that, as in the co- and counter-propagating pump and signal beam cases, the phase relationship between the constituent beams is the

principal governing factor in the generation of a powerful idler wave. Therefore, to judge the phase-matching properties of this beam configuration, we can calculate the coherence length L_{coh} by generalizing the phase-matching relation for an orthogonal signal beam. To do this, we use the Pythagorean theorem to split up the phase-matching relation into its x and y components

$$|\vec{\Delta k}| = \sqrt{{\Delta k_x}^2 + {\Delta k_y}^2}. \tag{4.49}$$

For a forward- or backward-propagating idler wave, these components of Δk take the form

$$\Delta k_x = 2k_p \mp k_i, \tag{4.50}$$

$$\Delta k_y = k_s. \tag{4.51}$$

After substituting these terms into Eq. (4.49), we obtain the expression

$$|\vec{\Delta k}| = \sqrt{4k_p^2 + k_s^2 + k_i^2 \mp 4k_p k_i}. \tag{4.52}$$

While this equation is not as intuitive as previous phase-matching expressions, we can discern some important information from it at first glance. Notably, if we substitute $k_s = 0$, as in Chapter 2, this equation reduces to the value of Δk_x

$$|\vec{\Delta k}| = 2k_p \mp k_i. \tag{4.53}$$

In this case, a forward-propagating idler wave will be trivially phase-matched for $k_p = 2k_i$. However, it is not so trivial to phase-match a backward-propagating idler wave. Here, the usual trick of placing the pump or idler waves at the zero-index to remove their directional dependence does not work, as the signal wave already occupies this position.

To resolve under what conditions forward- and backward-propagating idler waves would be phase-matched with this configuration, we plot L_{coh} for a selection of pump and signal wavelengths in Fig. 4.7, investigating both forward- and backward-propagating light. We again use the dispersion profile of our zero-index waveguide.

In the case of forward-propagating idler light, we can see that the interaction is phase-matched so long as the signal wave is located at the zero-index wavelength. This is because, as the pump and idler waves would be co-propagating in this case, the interaction can be phase-matched by ignoring the momentum contribution of the signal wave and placing it at the zero-index wavelength. In the case of a backward-propagating idler beam, the phase-matching condition is more restricting. This interaction is only phase-matched if all constituent beams of the interaction are located near the zero-index wavelength. We also see that when an interaction is phase-matched for a backward-propagating idler wave, it is additionally phase-matched for a forward-propagating idler wave. In the next section, by establishing a general phase-matching condition, we will investigate the reason behind this cluster for the backward-propagating beam.

4.3.2 Omnidirectional phase matching with an arbitrary beam configuration

To obtain the coherence length for an arbitrary beam configuration, we can take the method applied in Subsection 4.3.1 and generalize it for pump, signal, and idler waves traveling in all

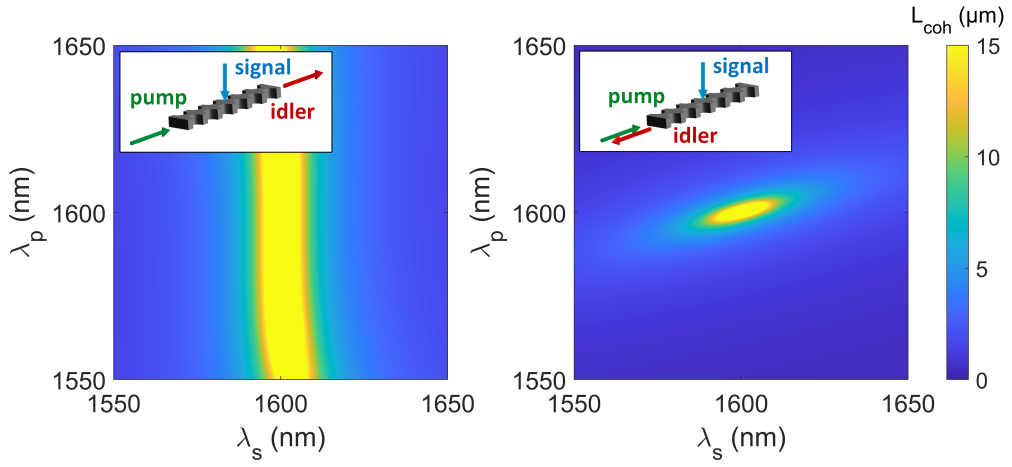

Figure 4.7 Numerical predictions of the coherence length, calculated using Eq. 2.49, for an a) forward-propagating (relative to the pump) and b) backward-propagating idler wave. In the case of a forward-propagating idler wave, the process is phase-matched when the signal beam is located at the zero-index wavelength. In the case of a backward-propagating idler wave, the process is phase-matched when all the beams are clustered near the zero-index wavelength. L_{coh} is plotted as a function of the pump wavelength λ_p and the signal wavelength λ_s. Bright yellow indicates a region where the coherence length exceeds 15 µm, the length of the zero-index waveguide studied.

directions. To judge the phase-matching properties of this beam configuration, we can again calculate the coherence length L_{coh}. Analogously to the previous section, we can define

$$|\vec{\Delta k}| = \sqrt{{\Delta k_x}^2 + {\Delta k_y}^2 + {\Delta k_z}^2} \tag{4.54}$$

and define the angles of the pump, signal, and idler waves in 3D coordinates. We define Δk_x, Δk_y, and Δk_z by using the angles of the pump, signal, and idler waves as in Fig. 4.8. At first glance, it may seem like characterizing these 3 arbitrary beams would require six angles (two for each wave respectively). However, we only require three. Without loss of generality, we may define the pump wave as being at $\phi, \theta = 0$, where ϕ and θ are the usual spherical coordinates. We can then define the signal wave as being on the xy-plane, and describe its position with respect to the pump wave with a single angle ϕ_s. Finally, we can describe the position of the idler wave using two angles: ϕ_i, the angle of the idler wave with respect to the pump wave on the xy-plane, and θ_i, the angle of the idler wave with respect to the pump and signal waves on the z-axis. Using the above definition for the angles, we can define the k_x, k_y, and k_z components of the phase-matching constraint as

$$\Delta k_x = 2k_p - k_s \cos\phi_s - k_i \cos\phi_i \cos\theta_i, \tag{4.55}$$

$$\Delta k_y = k_s \sin\theta_s + k_i \sin\phi_i \cos\theta_i, \tag{4.56}$$

$$\Delta k_z = k_i \sin\phi_i. \tag{4.57}$$

Where the signs are chosen in accordance with Fig. 4.8.

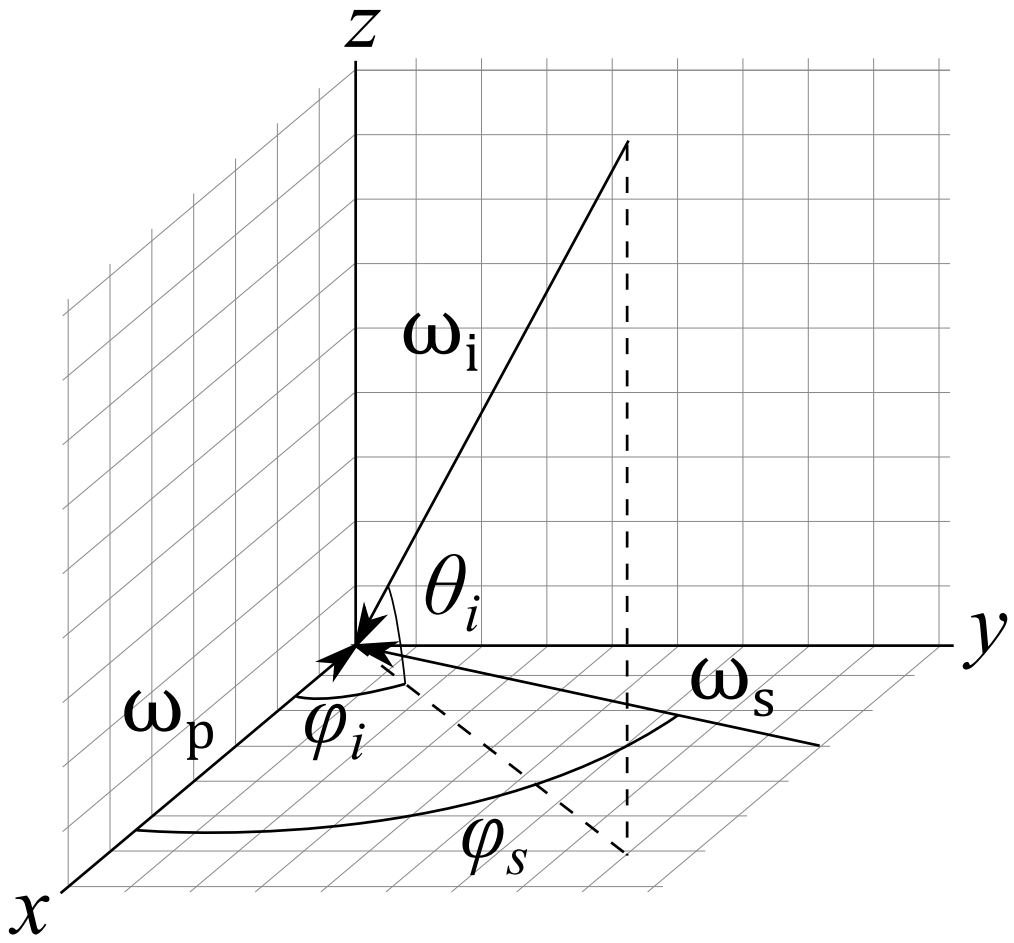

Figure 4.8 Representation of the three angles ϕ_s, ϕ_i, and θ_i for arbitrary signal and idler waves relative to the pump wave. Here, the pump wave is located on the x-axis, and the signal wave is located on the xy-plane. Note that here θ_i is defined as coming up from the xy-plane, contrary to the regular definition with spherical coordinates.

After substituting these terms into Eq. (4.54), we obtain an expression which simplifies to

$$|\vec{\Delta k}| = \sqrt{4k_p^2 + k_s^2 + k_i^2 - 4k_p(k_s\cos\phi_s + k_i\cos\phi_i\cos\theta_i) + 2k_sk_i\cos\theta_i(\cos\phi_s\cos\phi_i + \sin\phi_s\sin\phi_i)}. \tag{4.58}$$

From this expression, we can determine the phase-matching constraint for an arbitrary set of beams. This phase-matching condition, as a result, is a generalization of all previous phase-matching conditions. To get some intuition as to the results of this equation, we can plot a small subset of all the possible angles using the dispersion profile of our zero-index waveguide. In Fig. 4.9, we plot the angles ϕ_s and ϕ_i in intervals of $\frac{\pi}{2}$ all the way up to $\frac{3\pi}{2}$, for the angles $\theta_i = 0$, $\frac{\pi}{2}$ (including π and $3\pi/2$ would repeat the same information). This angular size is chosen due to the large volume of graphs that are generated when using smaller angles. However, the code used to generate these plots can be found in Appendix A.2 and can be

run with smaller angular values. The FWM process always remains phase-matched even for small angles.

While not comprehensive of all the angle combinations, the 20 generated plots give us an idea of the coherence for most likely beam configurations. The small subset of angles in Fig. 4.9 provides some interesting intuition on the nature of Eq. (4.58), and confirmation on our previous ideas regarding phase matching when $n = 0$. In the case where all angles are equal to zero, corresponding to co-propagation of all waves, we have phase matching everywhere. When only ϕ_s changes, we can achieve phase matching by simply placing the signal wave at the zero-index wavelength, and thereby eliminate the directional dependence of the displaced signal wave. We can analogously do the same when there is a variation in ϕ_i or θ_i for the idler wave. When both ϕ_s and ϕ_i are altered by an equal amount, we can achieve phase matching by placing the *pump* wave at the zero-index wavelength. This is because, if the other two waves are displaced by the same amount, the pump wave effectively becomes the displaced wave; placing the pump wave at the zero-index wavelength, therefore, solves this problem. These two situations where the signal and pump waves can be placed at the zero-index wavelength to obtain a phase-matched interaction can be observed in the counter-propagating case.

There are cases where placing one of the components of the FWM interaction at the zero-index wavelength to effectively "restore the collinearity" and enable phase matching cannot be done. This occurs when all three constituent beams travel in separate directions. In such cases, we see that L_{coh} is large when all the waves are clustered near the zero-index wavelength, with some variation. The conclusion that can be drawn from this is that in cases where two components of the FWM interaction are co-propagating, phase matching can be achieved as long as the non-co-propagating beam is placed at the zero-index wavelength. However, when this is not the case, phase matching is achieved when all the waves are clustered near the zero-index wavelength. An example of these phenomena can be seen in the previous subsection, where, in the case of a backward-propagating idler beam, all components of the FWM interaction propagate in different directions. While the phase-matching condition does vary with beam configuration, a FWM interaction for an arbitrary beam configuration is always phase-matched under some condition. This is effectively a theoretical demonstration of omnidirectional phase matching in zero-index media.

In this chapter, we have developed models that allow us to theoretically predict the power of a generated idler wave with respect to the initial conditions of the pump and signal beams. We have additionally theoretically demonstrated that zero-index materials always allow us to phase-match a nonlinear optical interaction irrespective of beam orientation. Having established this prediction, we may now experimentally generate idler waves under these different conditions and therefore verify our theory. In the next chapter, we describe our experiment, and the methods used to realize it.

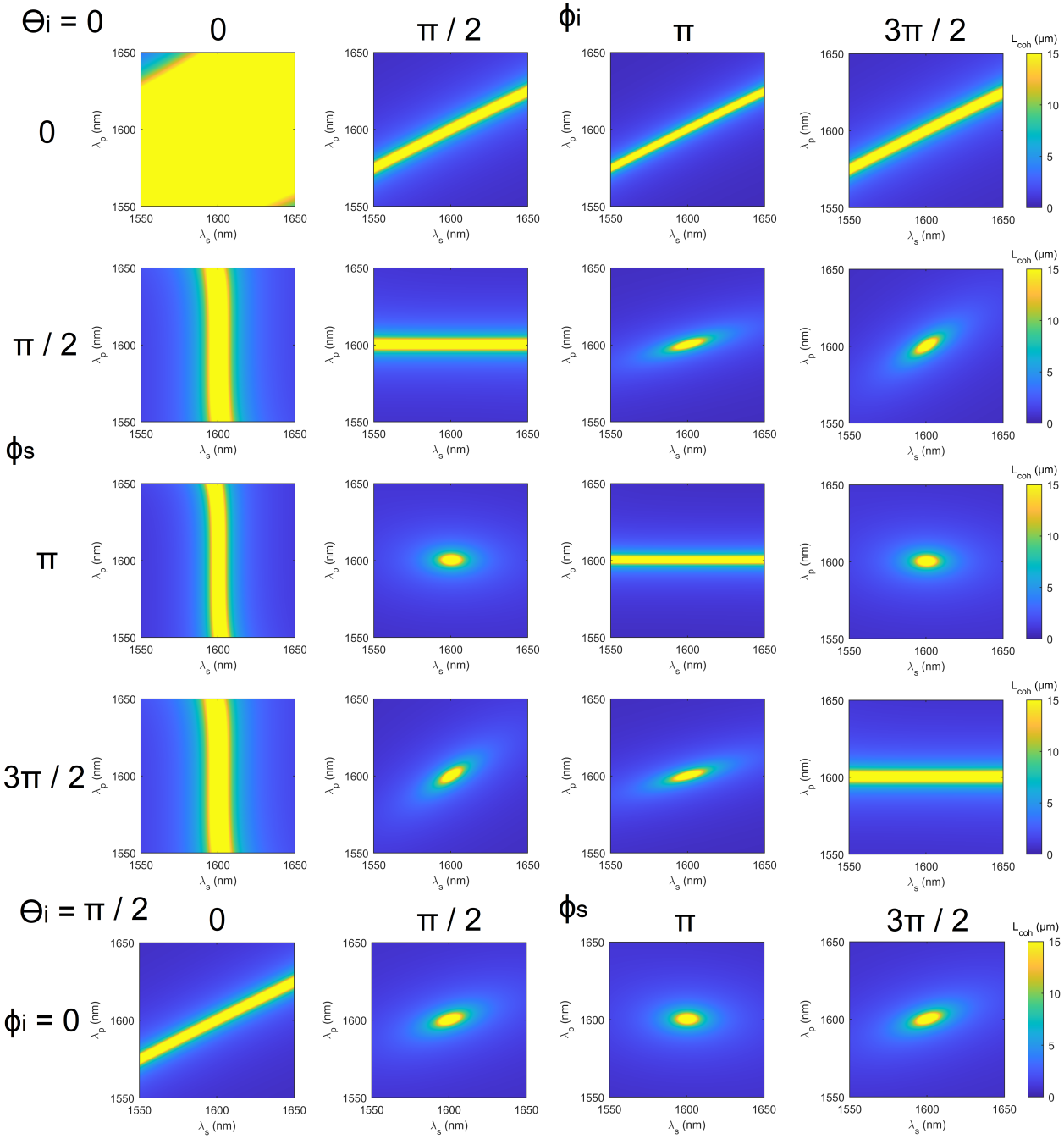

Figure 4.9 Numerical predictions of the coherence length, calculated using Eq. 2.49, for 20 separate combinations of the angles ϕ_s, ϕ_i, and θ_i. As ϕ_i's value is inconsequential when $\theta_i = \frac{\pi}{2}$ (when $\theta_i = \frac{\pi}{2}$, the idler wave is entirely in the z-direction and rotating it therefore changes nothing), we only include $\phi_i = 0$ for this case to avoid repetition. L_{coh} is plotted as a function of the pump wavelength λ_p and the signal wavelength λ_s. L_{coh} is plotted from 0 µm up to a maximum value of 15 µm, and the angles are given in radians. The code used to generate these plots can be found in Appendix A.2, and can be modified to include a broader range of angles.

Chapter Five
Experiment and methods

To experimentally verify the results presented in the previous chapter, we must choose lasers to act as the pump and signal beams, and couple these lasers into our zero-index waveguide to generate an idler wave. In this chapter, we describe the methodology of our experiment, as well as the experimental setup with which we obtain our results. Once the methodology and experimental setup have been described, we then present our experiment as well as the obtained results and compare our results with our theoretical predictions.

5.1 Method

In Chapter 4, we determined which pump and signal wavelengths were predicted to generate the most powerful idler waves. In our experiment, our goal is to verify whether or not these predictions are accurate. We do this by sampling a subset of data points and comparing the experimentally obtained idler wave powers to those that are theoretically predicted. To generate an idler wave in the lab, we simultaneously apply a pump beam at ω_p and a signal beam at ω_s in our zero-index waveguide. The pump beam supplies the photons necessary for the nonlinear interaction, while the signal beam promotes the generation of a particular signal and idler photon pair, ω_s and $\omega_i = 2\omega_p - \omega_s$. The signal beam promotes this particular pair through the linear dependence of the idler amplitude on that of the signal in its coupled-amplitude equation.

5.2 Experimental setup

Below, we describe and justify our choice of laser sources for our experimental setup. As the power of the idler beam is expected to exhibit a quadratic dependence on the power of the pump wave $P_i \propto {P_p}^2$, it is critical that the pump laser be as powerful as possible to generate the strongest idler wave. To satisfy this requirement, we use a powerful pulsed laser as the pump beam. As opposed to a continuous-wave (CW) laser, which has a constant power output, a pulsed laser instead emits periodic pulses with comparatively very high peak powers (i.e., 1000 W vs. 1 W).

Pulsed lasers can be characterized by several parameters. The repetition rate dictates how often pulses are fired. The pulse width indicates the elapsed time between the rising and falling edges of an optical pulse. This value can vary considerably depending on laser

choice: femtosecond, picosecond, and nanosecond lasers, for example, are all very common and have a variety of applications. Other useful parameters are the peak power of the pulse, as well as its optical bandwidth, the range of frequencies over which the pulse is distributed. As the spectral bandwidth of the pulse scales with the inverse of the pulse width, the short pulses produced by pulsed lasers typically end up spanning a considerable bandwidth.

The pulsed laser used to act as the pump in this experiment consists of three separate components: a *Verdi 10* 532 nm CW laser, a Mira Optima Titanium-Sapphire (Ti:Sapph) laser, and a Mira-OPO optical parametric oscillator (OPO). The Ti:Sapph laser intakes the CW input generated by the Verdi 10 laser and uses the process of mode-locking to create a pulsed output that can reach up to 840 nm [64]. Subsequently, the OPO uses the process of difference-frequency generation to generate its own signal and idler pulses (not to be confused with those involved in the FWM process), yielding infrared wavelengths of up to 1600 nm for use in our experiment. This combined setup fields pulses with a repetition rate of 76 MHz, a pulse width of 3 ps, a peak power of 1300 W, and a spectral bandwidth of roughly 5 nm in its FWHM.

As the generated idler wave exhibits a linear dependence on the power of the signal wave, it would also be ideal for the signal beam to be as powerful as possible. Therefore, it would seem reasonable for the signal beam to also be a pulsed laser. However, when two pulsed lasers are used, both pulses must overlap in space — if one pulse lags behind the other, there will be no power overlap between both beams, and FWM will not occur. To avoid the problem of aligning these pulses with one another, we instead use a CW laser. As opposed to pulsed lasers, CW lasers feature an extremely narrow bandwidth. The CW laser used in this experiment consists of a Santec TSL-710 CW laser, which is subsequently amplified by an erbium-doped fiber amplifier (EDFA). The TSL-710 is a tunable CW laser that is capable of accessing wavelengths from 1480 nm to 1640 nm, with peak powers of up to 1 mW and a bandwidth of 0.1 pm. Subsequently, the EDFA intakes the CW output and amplifies it. Two separate amplifiers are used during the course of the experiment to cover different wavelength ranges. An AEDFA-33-B-FA amplifier is capable of amplifying a 1 mW CW input ranging from 1535 nm to 1565 nm up to 2.25 W in power. An L-band EDFA by JDS Uniphase with model number OAB1594+20SC0 is capable of amplifying a 1 mW CW input ranging from 1565 nm to 1610 nm up to 100 mW in power.

In our theoretical derivation in Chapter 4, we assume that the pump and signal beams are plane waves. In this experiment, we use a pulsed laser and a CW laser. While CW lasers emit plane waves, pulsed lasers emit individual pulses. One may therefore wonder whether or not the theoretical treatment in the previous chapter can still be applied. Were the pump and signal lasers both pulsed lasers, the equations in the previous chapter would not take overlap into account, and the theoretical derivation in the previous chapter would no longer be well-founded. However, if we remain in the frame of reference of the pulsed pump wave, the equations remain equally valid when using a CW signal source. This is because, in the frame of reference of the pump pulse, the pump and signal waves always overlap with one another.

There is a large amount of background light surrounding the laser spectrum of both the pump and signal lasers. With the pump laser, this occurs due to the large optical bandwidth, while in the case of the signal laser, this occurs due to spontaneous emission

by the EDFA. While this background light is far weaker than the peak power of either of these lasers, it is strong enough to potentially obfuscate any generated idler wave. To attenuate this background light, we pass each laser through a band-pass filter centered on the wavelength of the pump or signal waves. Three separate band-pass filters are used for different wavelengths: two filters with peak center filtering wavelengths of 1650 nm and 1600 nm with optical densities of 4, and a filter with a peak center filtering wavelength of 1570 nm with an optical density of 6. All three filters can be tuned to lower peak center filtering wavelengths by tilting them. These three filters are alternated between the pump and signal beams to provide the best beam attenuation given the wavelengths in use.

Now that our lasers have been chosen, we must build a setup capable of polarizing these lasers to the required transverse-electric polarization, modulating their power, and coupling them into our zero-index waveguide. A schematic of the complete setup can be seen in Fig. 5.1. Both beams must be collimated with roughly the same spot size (0.5 cm in diameter) so that co-propagating beams can be coupled into the zero-index waveguide via the same lens. We use a system of lenses to collimate the beams, and we use a telescope composed of two lenses to adjust the spot size while retaining the collimation. To polarize the lasers, we use the combination of a half-wave plate and polarizing beam-splitter for each laser to both achieve the desired transverse-electric polarization and provide a means with which we can modulate the power of the pump and signal beams. While the OPO already possesses a transverse-electric polarization, the function of the half-wave plate is to then rotate the polarization of the beams to an arbitrary angle, before the polarizing beam-splitter recorrects it to the original one. Therefore, the power can be maximized by rotating the half-wave plate to the polarization aligned with that of the polarizing beam-splitter, and it can be minimized by rotating the half-wave plate to the polarization at a 90-degree angle with respect to the polarizing beam-splitter.

Following polarization, the pump and signal beams are coupled into the zero-index waveguide. In the case of co-propagating beams, we combine the pump and signal beams using a beamsplitter cube (beam cube). To ensure that both beams are perfectly collinear, we employ a system of mirrors before the beam cube for the signal beam so that it may be aligned with the pump beam (not shown in Fig. 5.1). The fraction of the power that is not used to couple into the waveguide is then directed towards a detector to determine the power of the pump and signal beams when performing measurements. Once combined, the pump and signal beams can be coupled into the waveguide through its coupling pads. These pads each have a 5 dB loss at the input and exit facets.

To determine the generated output, we collect the light using multi-mode optical fibers on both sides of the waveguide. On the side of the input facet, we set up a non-polarizing beam cube to allow the input light to travel through while redirecting the output light to our detector. On the opposite side of the waveguide, we simply focus the output light on our multi-mode fiber. Once the light has been collected, it is spectrally decomposed by an AQ-6315E optical spectrum analyzer (OSA) for subsequent analysis. To find the spectrum of the light, the OSA uses a diffraction grating to spectrally separate light and collects all power within a certain bandwidth of the area it is measuring for each data point (in our case, this bandwidth is 2 nm). This results in features with slight spectral broadening. An example spectrum of a FWM interaction measured by the OSA is shown in Fig. 5.2. With

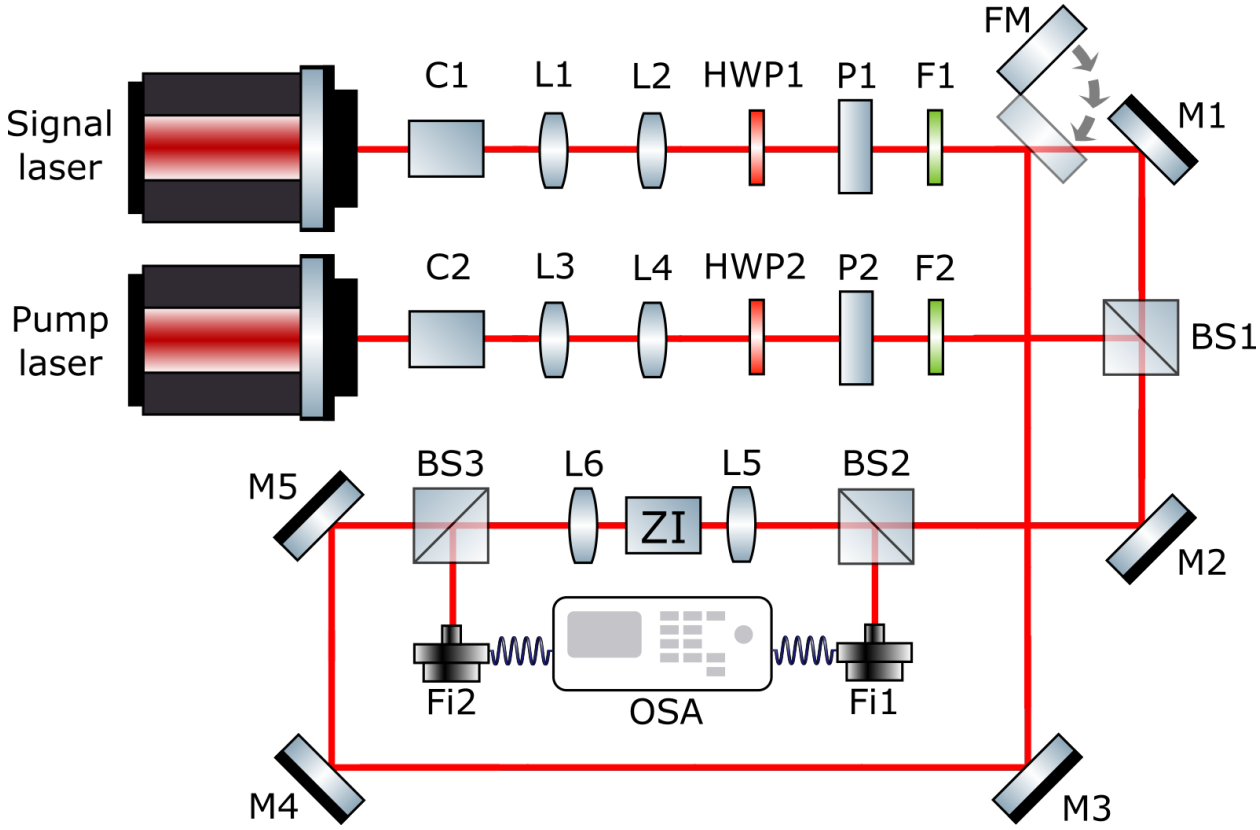

Figure 5.1 Schematic of the setup used to couple the pump and signal beams into the zero-index waveguide. The pump and amplified signal beams pass through lens systems to collimate the beams (C1 and C2), and have their spot sizes matched using telescopes (L1, L2, L3, L4). The beam subsequently has its power modulated using a half-wave plate and polarizing beam-splitter (HWP1, HWP2, P1, P2), and then spectrally filtered (F1, F2). In the case of co-propagating pump and signal beams, the beams are combined using a beamsplitter cube (BS1) and a lens (L5) subsequently focuses the beams into the zero-index waveguide (ZI). Optical fibers (F1, F2) on either side collect the forward- and backward-propagating generated light exiting the waveguide, and send it to the OSA for further analysis. For counter-propagating beams, the flip mirror (FM) is flipped into position, and the signal light is focused into the zero-index waveguide via the lens L6. Mirrors are represented by M.

the longest integration time, the OSA is capable of measuring light of -90 dBm (i.e., 1 pW) in power and above. When this longest integration time is subsequently averaged 30 times or more, this lower limit can be further reduced to -95 dBm. Under this value, any light is obscured by the ambient noise in the background.

The pump wave's spectrum tends to drift by a few nanometers over time. Therefore, when the pump wave is measured and then the idler wave is measured some time later, the pump wave's measured spectrum may not correspond to that of the idler. We take this into account by measuring the peak power of the idler wave several times and determining its

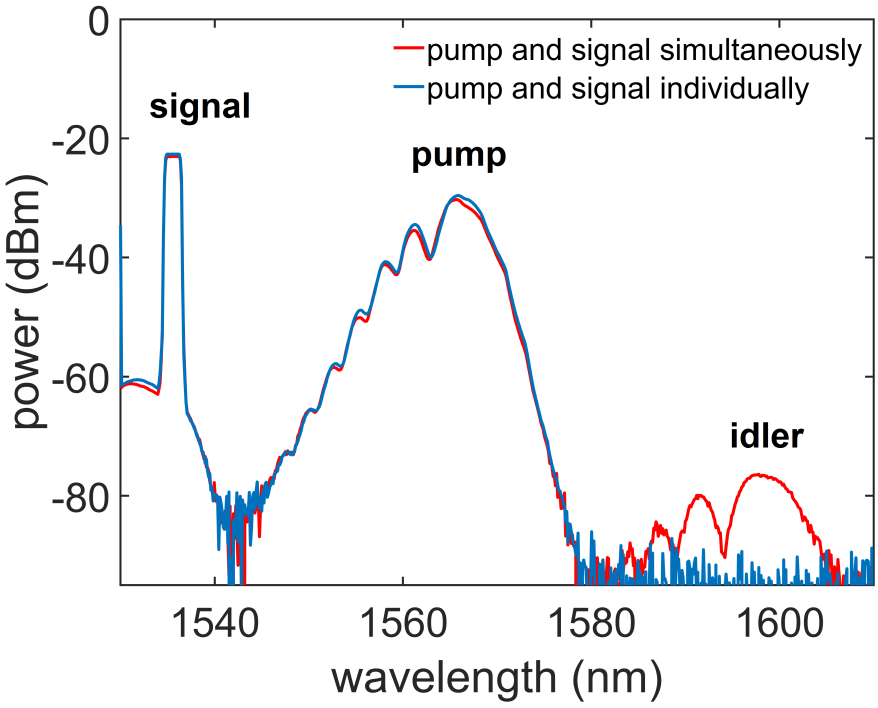

Figure 5.2 Example spectra of a FWM process collected from the OSA. The blue curve consists of the pump and signal waves measured separately. The red curve is the spectrum produced when the pump and signal beams are simultaneously applied, producing an idler wave at $\omega_i = 2\omega_p - \omega_s$, as expected. As the idler wave spectrum is a convolution of the signal and pump wave spectra, and since the signal spectrum is a narrow peak, the convolution spectrum closely resembles the pump spectrum. While in reality, the signal wave's spectrum is a 0.1 pm wide line, it appears to be 2 nm wide due to the collection settings of the OSA.

uncertainty for the given pump and signal waves.

In the case of counter-propagating beams, a beam cube is also placed on the side of the zero-index waveguide opposite to the pump beam. This allows the signal beam to be coupled into this side while maintaining the functionality of both detectors. To introduce the signal beam into the zero-index waveguide from outside the plane of the device layer, we bring the signal beam outside of the beam plane, and then focus it onto the device from above, using a lens.

5.3 Preliminary measurements

To first verify whether or not the generated idler wave is the product of a FWM interaction, we plot the peak power of the idler wave as a function of the peak power of the pump wave for both the forward- and backward-propagating light. If the generated idler wave is the result of a FWM interaction, the idler wave's power will vary quadratically with that of the pump wave. In dB scale, a quadratic dependence is indicated by a slope of 2. The results of this

measurement can be seen in Fig. 5.3. For the forward-propagating light, we observe a slope of 2.2 ± 0.3, while for the backward-propagating light, we observe a slope of 1.8 ± 0.3. Both of these values approach 2, confirming the prediction of a quadratic relationship between pump and idler power. Deviations from 2 likely occur due to the background noise of the OSA, and fluctuations in the pump spectrum (both of these factors are discussed in Section 5.2). It can summarily be concluded that the idler wave is produced by a FWM process.

To determine the amount of error in all of our results, we perform a measurement where we calculate the same data point several times. From these repeated measurements, we can determine the amount of variability from repeated measurements. We can then assume that the uncertainty for this data point is identical to the uncertainty for all of our data points. We selected this method of determining the uncertainty of our data due to the impracticality of performing all of our measurements several times (one high-resolution OSA sweep requires approximately half an hour). In this measurement, we took 7 data points for the peak power of both the forward- and backward-propagating idler waves, and then determined the standard deviation σ, given by

$$\sigma = \sqrt{\frac{\sum_{n=1}^{N}(x_n - \bar{x})^2}{N-1}}, \tag{5.1}$$

where the sum is taken over every data point x_n. Here, N is the number of data points, and $\bar{x}$ is the mean. The standard deviation is then converted to the dB scale by dividing it by the mean to obtain the coefficient of variation and then converting this dimensionless quantity to the logarithmic scale. We obtain an uncertainty of [2.17 dB, -2.77 dB] for the forward-propagating idler wave, and an uncertainty of [1.83 dB, -2.24 dB] for the backward-propagating idler wave. This quantity is uneven due to the nature of the logarithmic scale. While we will note this uncertainty explicitly only for the power measurement, it can be applied to the peak power of the idler wave for all data in this chapter.

5.4 Co-propagating pump and signal beams

Now that we know that the generated idler wave is the product of a FWM interaction, we can proceed with the main experiment. In Chapter 4, we saw that for co-propagating pump and signal beams in a lossless FWM interaction, a forward-propagating idler wave will always be well phase-matched, while a backward-propagating idler wave will be well phase-matched when the idler wave is located at the zero-index wavelength. To verify this prediction, we vary the pump wavelength in increments of 5 nm from 1555 nm to 1600 nm. While the pump wave is varied, we maintain a constant spectral separation between the pump and signal waves

$$\Delta f = c/\lambda_p - c/\lambda_s = 2.4\text{THz}. \tag{5.2}$$

This corresponds to the signal wave being approximately 20 nm shorter than the pump wave at any given time. A constant spectral separation ensures that any change in the power of the idler wave cannot be attributed to dispersion. By varying the pump and signal beams in this manner, the idler wave, which is simultaneously generated propagating in both the forward

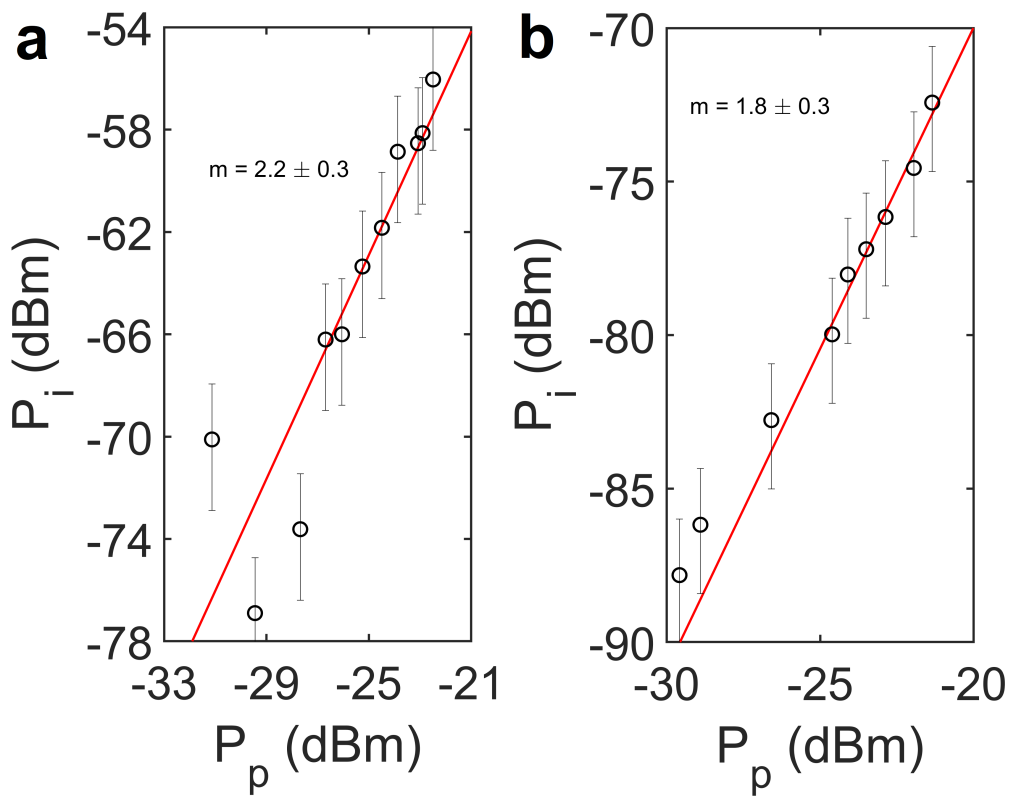

Figure 5.3 Peak power of the idler wave P_i as a function of the peak power of the pump wave P_p. In a), we plot the powers for forward-propagating light, while in b), we plot the powers for backward-propagating light. The uncertainties listed are taken from the uncertainty measurement (see the second paragraph of this subsection). As the slope of P_i as a function of the peak power of the pump wave P_p is nearly 2, it can be concluded that the idler wave's power varies quadratically with that of the pump wave in both the forward- and backward-propagating cases, as expected for FWM.

and backward directions, is generated over a large range of wavelengths. Critically, it passes through the zero-index wavelength. If our theory is correct, the backward-propagating idler wave should peak at the zero-index wavelength. The forward-propagating idler wave, on the other hand, should only vary in power through the effect of loss and impedance variations on the interaction. We plot our results in Fig. 5.4, and using Eqs. (4.26), (4.32), and (2.43), we plot our theoretical predictions alongside our experimental results for comparison. We use $n = 3.4757$ for the surrounding silicon waveguide and $\chi^{(3)} = 2.45 \times 10^{-19}$ V^2/m^2 for the third-order nonlinear susceptibility [65, 66].

Before conducting a thorough analysis of the result, it must first be stated that the features expressed by the forward-propagating idler wave peaks differ from those expressed by the simultaneously generated backward-propagating idler wave peaks. This difference in behavior is critical, as it demonstrates that the backward-propagating idler wave is not simply a reflection of the forward-propagating idler wave. As a result, it proves both waves

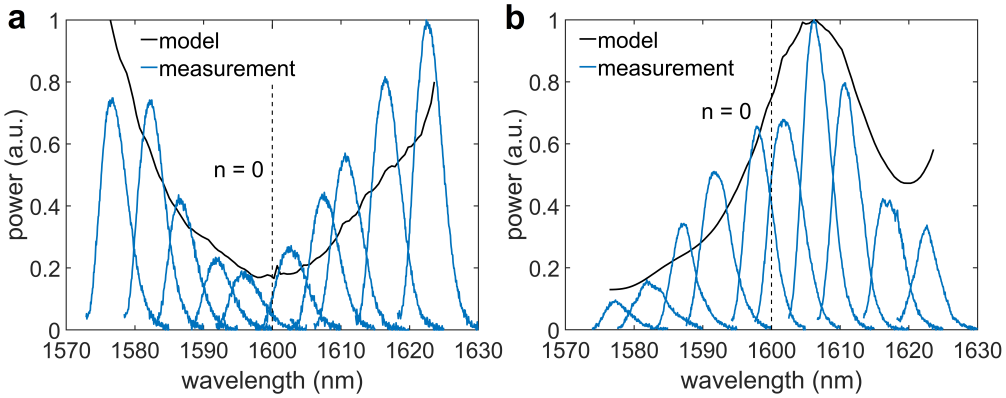

Figure 5.4 Generated idler wave spectra for a FWM process with co-propagating pump and signal beams, as a function of the idler wavelength. In a), the results for a forward-propagating idler wave are plotted, while in b), we plot the results for a forward-propagating idler wave. The blue peaks consist of the individual idler waves measured by varying the pump and signal beams with a constant spectral separation, and are normalized to unity with the peak value of the most powerful pulse. The black curves show the normalized value for the peak power of each measured idler pulse, as the wavelengths of the pump and signal beams are varied in accordance with the experiment. This value is predicted by Eqs. (4.26), (4.32), and (2.43). The code used to generate these curves is included in Appendix A.3.

are independently generated and subject to their own phase-matching and loss conditions.

In the forward-propagating case, the peaks exhibit a dip in power at the zero index wavelength, as predicted by the wavelength-varying losses and permeability. In the backward-propagating case, the idler wave peaks in power shortly after the zero-index wavelength, as predicted by the phase-matching condition. The theoretical predictions overall agree very well with the generated idler peaks. In the case of the forward-propagating idler wave, the theoretical model displays almost perfect agreement with the experimental data. In the case of the backward-propagating idler wave, the theoretical prediction agrees very well with nearly every idler peak, but slightly deviates in accuracy for the peak at the longest wavelength. This increase in the model's predicted power is caused by the rising permeability. The discrepancy between the model and the experimental results can likely be explained by the fact that the refractive index and impedance data is simulated, while the loss data is adapted from that of another similar waveguide, as stated in Chapter 3.

While our theoretical prediction based purely on phase-matching constraints states that the forward-propagating idler wave should have equal magnitudes at every wavelength. However, our results indicate that this is not the case. This discrepancy can be explained by incorporating a dispersive loss and impedance into the model. In Fig. 5.5a, we isolate the effects of these two quantities on the output idler power by superimposing two curves over the measurement results: a constant permeability and therefore a constant impedance with a variable loss (red curve); and a variable permeability and a constant loss (green curve). Plotting these two curves in this manner shows that when the impedance is held constant, the forward-propagating idler is attenuated for wavelengths longer than 1600 nm. When

the loss is held constant, the forward-propagating idler is attenuated for wavelengths shorter than 1600 nm, and the resulting spectrum appears almost identical to the shape of the impedance profile shown in Fig. 3.7d. When both model curves are compared, it is clear that the spectrum of the forward-propagating idler is a result of the combination of these two factors. In Fig. 5.5b, we plot our theoretical prediction when all wavelength-varying terms, bar the phase-matching constraint, are held constant. In this case, we can see that the phase-matching constraint predicts a nearly flat curve. As a result, we can conclude that the spectrum of the forward-propagating idler peaks is caused by wavelength-variable impedance and loss factors, while the spectrum of the backward-propagating idler peaks is primarily the result of the phase-matching condition.

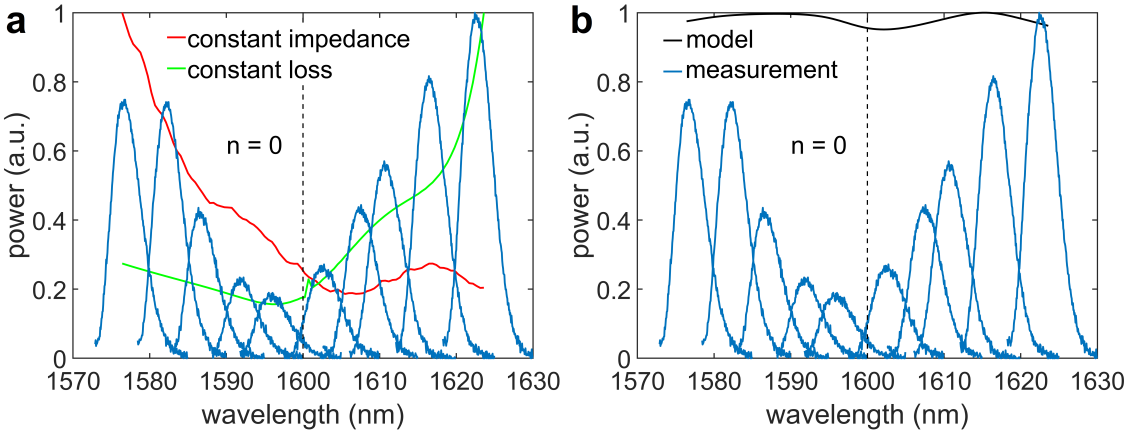

Figure 5.5 Variations in the predictive model for a forward-propagating idler wave. a) Generated idler wave spectra in the forward-propagating direction for a FWM process with co-propagating pump and signal beams, compared to two theoretical predictions for the peak power of each measured idler pulse. All results are normalized to unity. For the red curve, the impedance is made wavelength-invariable, allowing us to isolate the effects of loss. For the green curve, the loss is made wavelength-invariable, allowing us to isolate the effects of impedance. While the red curve predicts an attenuation beyond the dip in the forward-propagating idler peaks, the green curve predicts an attenuation before the dip in the forward-propagating idler peaks. b) The same experimental data plotted against the theoretical prediction for the peak power of each measured idler pulse (black curve) when all wavelength-dependant quantities, bar the phase-matching constraint, are held constant.

In summary, the fact that the simultaneously generated forward- and backward-propagating idler peaks respond so differently to passing through the zero-index wavelength is overall strong proof that the idler wave both shows directional independence, and that each direction is subject to its own phase-matching requirement.

5.5 Counter-propagating pump and signal beams

Now that we have demonstrated that forward- and backward-propagating idler waves perfectly match our theoretical predictions when the pump and signal beams are co-propagating, we can move on to counter-propagating pump and signal beams. In Chapter 4, we saw that for counter-propagating pump and signal beams in a FWM interaction, a forward-propagating idler wave will be well phase-matched when the signal wave is located at the zero-index wavelength. On the other hand, a backward-propagating idler wave will be well phase-matched when the pump wave is located at the zero-index wavelength.

In Chapter 4, we also determined that a counter-propagating pump and signal beam arrangement is extremely sensitive to loss. As the waveguide used in the co-propagating pump and signal beam experiment is 14.8 µm in length, and the loss in this waveguide can be as high as 1 dB/µm, loss would cause an extreme attenuation of any idler wave generated with counter-propagating beams. This attenuation is so high that when this waveguide is used, the generated idler wave is nearly vanishing. However, given that the loss and length of this zero-index waveguide greatly suppress the generation of an idler wave, it can be deduced that were an idler wave to be observed whatsoever, that such an interaction would have to be extremely well phase-matched. Therefore, any detected idler wave would be a testament to the phase-matching potential of zero-index media. In Fig. 5.6, we show generated forward- and backward-propagating idler waves in our 14.8 µm waveguide.

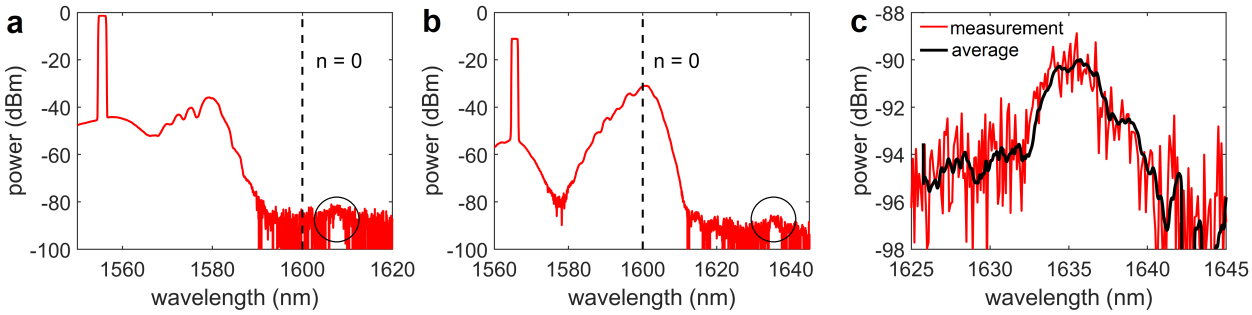

Figure 5.6 Generated idler wave spectra for counter-propagating pump and signal beams. a) Spectrum showing FWM for counter-propagating pump and signal beams for a forward-propagating idler wave. The signal and pump beams are at 1555 nm and 1580 nm, respectively, while the idler wave appears at 1605 nm. b) Spectrum showing FWM for counter-propagating pump and signal beams for a backward-propagating idler wave. The signal and pump beams are at 1565 nm and 1600 nm, respectively, while the idler wave appears at 1635 nm. In a) and b), due to high losses in the very long 14.8 µm waveguide, the generated idler waves are only barely visible. In c), we show the idler peak generated in b) in red, subsequently remeasured 100 times, and then averaged. Here, the idler peak is evident when compared to the background, which has been reduced to the OSA's measurement limit of -95 dBm. The black curve consists of the filtered data, which makes the presence of a peak more evident.

To generate a stronger idler wave, we can use our second waveguide, which is 11.1 µm in

length and has a zero-index wavelength of 1625 nm, as described in Chapter 3. In Fig. 5.7, we show generated forward- and backward-propagating idler waves in this waveguide. These waves are comparably more evident than the other two are, and are simultaneously generated.

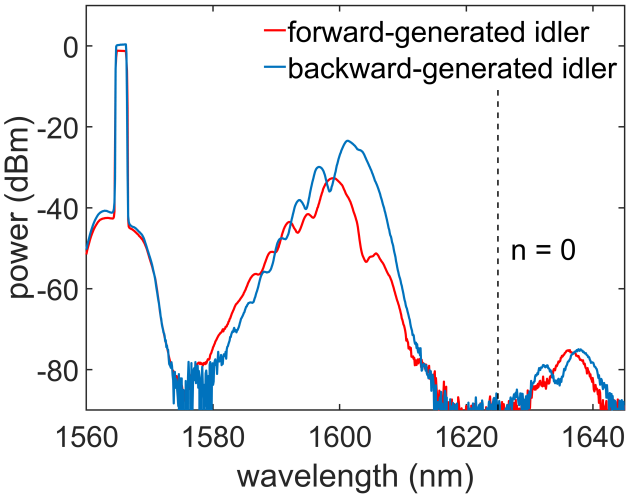

Figure 5.7 Simultaneous generation of idler waves with counter-propagating beams. When the pump and signal beams are counter-propagating, an idler wave is simultaneously generated in the forward (co-propagating with pump wave, red) and backward (co-propagating with signal wave, blue) directions. The signal and pump beams are located at 1565 nm and 1600 nm, respectively, while the generated idler waves appear at 1635 nm.

5.6 Out-of-plane signal beam

By testing the co-propagating and counter-propagating pump and signal beam cases, we have verified that every collinear beam arrangement for the pump, signal, and idler waves may be phase-matched. To further validate our theory, we now position the signal beam such that it couples into the zero-index waveguide from above the plane of the device layer, orthogonal to the pump beam. To generate an idler wave resulting from a signal wave orthogonal to the pump wave, we use an EDFA capable of amplifying the signal beam up to 2.25 W in power. This is done to optimize the probability of detecting an idler wave due to the increased power. As the maximum wavelength that this EDFA is capable of amplifying is 1565 nm, we use this wavelength for the signal beam. Being required to choose this wavelength for the signal beam, we decide to choose a wavelength of 1585 nm for the pump wave, for three reasons: 1) Beyond this wavelength, the loss of the waveguide markedly increases. 2) This allows all three components of the FWM interaction to be near the zero-index point, and 3) A minimum distance of roughly 20 nm is required between the pump and signal waves to clearly differentiate the idler wave from the pump wave in the OSA due to the pump wave's larger spectrum.

At 1565 nm, the refractive index is slightly positive ($n \approx 0.17$). As a result, to satisfy

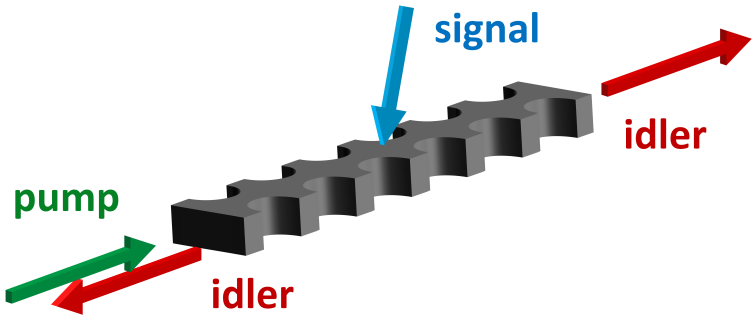

Figure 5.8 Beam configuration for the out-of-plane signal beam setup. The pump beam is traditionally coupled into the waveguide, while the signal beam couples into the light guide at a small angle relative to normal incidence. From this configuration, forward- and backward-propagating idler waves are generated.

Snell's law, the signal beam must assume a slight angle (9.8°) with respect to normal incidence to couple into the waveguide (See Fig. 5.8). To determine whether or not we are adequately coupled into the waveguide, we aim the signal beam so that it is incident onto the chip in roughly the correct position. We then note the amount of light coupled into the waveguide by using detectors on either side. However, as there are two detectors, there are two ways to align the signal beam — by maximizing the light transmitted to the backward-propagating detector, or to the forward-propagating detector (Shown in Fig. 5.9). When the signal beam is aligned according to a specific detector, the signal light will always have a larger proportion of its power concentrated on the side of the zero-index waveguide to which that detector is nearest. This means that we can try to generate an idler wave under the two conditions for which we can couple the signal beam: on the side of the waveguide nearest to the pump beam, or on the side of the waveguide furthest from the pump beam.

When coupling the signal beam such that the signal light is maximized on the side furthest from the pump beam, there is no detectable idler wave when measured from either side of the waveguide. However, when coupling the signal beam such that the signal light is maximized on the side nearest to the pump beam, a backward-generated idler wave can be detected and is shown in Fig. 5.10.

In the case of a signal beam angled towards the facet of the waveguide on which the pump wave is incident (Fig. 5.10), the phase-matching condition outlined in Subsection 4.3.2 yields the plots shown in Fig. 5.11. While our practical constraints prevent us from accessing the yellow region in these figures, we can get as close as possible to these requirements with the wavelengths used in our experiment. For a pump wavelength of 1585 nm and a signal wavelength of 1565 nm, we obtain coherence lengths of 1.86 µm for a forward-propagating idler wave, and 1.91 µm for a backward-propagating idler wave. While this is quite low, for an appropriately placed signal wave (i.e., very close to either side such that the effective length is much smaller), this coherence length should be large enough for an idler wave to be visible. This is because, in a lossy medium, most of the light is produced at the start of an interaction, where the light is most powerful. However, such a small coherence length would make our interaction less efficient.

This configuration was unable to generate any measurable idler wave in the forward-

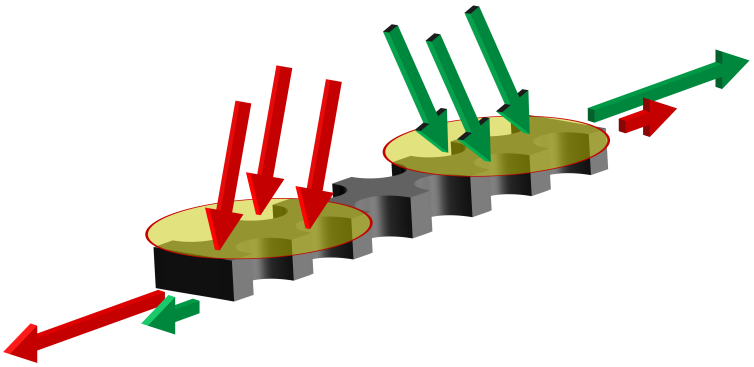

Figure 5.9 Alignment of the out-of-plane signal beam. The out-of-plane signal beam can be aligned by maximizing the input of either of the two detectors on both sides of the waveguide. These detectors can be maximized by shining the signal beam on the same side of the waveguide as the detector. Here, both situations are shown with the red and green arrows respectively. When the signal beam is incident on the left side of the waveguide, the output on that facet of the waveguide is strongest, while it is weaker on the right side. When the signal beam is incident on the right side, the output is strongest on the right side and weaker on the left side.

propagating direction. However, this is not entirely unexpected, as analogously to the co-propagating case, the forward-generated idler wave must propagate much further in the waveguide. The additional propagation, and therefore additional loss, is most likely the reason why no forward-propagating idler wave could be seen, despite the more lenient phase-matching condition for that type of interaction. However, a backward-propagating idler wave was measured. Recall that in Chapter 4, we discovered that a backward-propagating idler wave with this configuration has the very stringent phase-matching condition of all beams needing to be near the zero-index wavelength. We also discovered that the reason for this stringent phase-matching condition was the fact that in that case, all three constituent beams are traveling in different directions. It is accordingly a testament to the potential of zero-index materials that such a beam configuration could still generate an idler wave like the backward-propagating idler wave in this case.

The observation of the idler wave generated in the waveguide when excited from outside the device layer could be explained in two ways: 1) The signal beam, which is incident on the waveguide from outside the device and at an incident direction very different to the guided modes of the waveguide, can generate a measurable idler wave because the phase-matching condition has been so relaxed by the wave vectors vanishing at the zero-index wavelength, as we claim; 2) The signal beam can couple from free space into the guiding mode of the waveguide, and subsequently generate FWM because of the wave vectors vanishing at the zero-index wavelength. The present experiment cannot distinguish between these two explanations for the observed idler wave. However, it is clear that the vanishing k-vector, and therefore, a near-zero refractive index, is the cause of FWM in the waveguide when excited from outside the device layer, as it is the reason behind both of these explanations being able to generate any idler wave whatsoever.

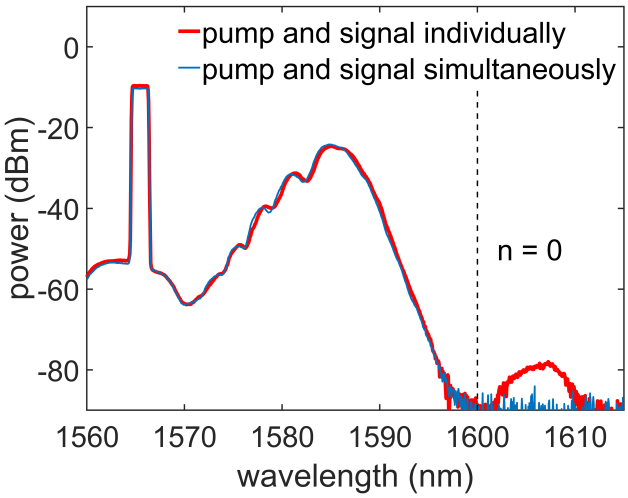

Figure 5.10 Idler wave resulting from an out-of-plane signal beam. Generated spectra obtained in the backward-propagating direction when a signal beam couples from out-of-plane. An idler wave is generated only when the pump and signal beams are simultaneously applied (red curve compared to the blue curve).

While ideally, we would be able to further analyze the generated backward-propagating idler wave, unfortunately, there are experimental inconveniences that make this very difficult to do in practice. 1) While all incident angles are phase-matched, the wavelength-dependant refractive index of the waveguide dictates which incident angle can couple to the guided modes. Therefore, the signal beam must be realigned whenever its wavelength is adjusted. 2) The alignment is very sensitive, which means the error on the measurement is very large. This means that, unlike the co-propagating case, it is not feasible to do a wavelength sweep here. However, similarly to the counter-propagating case, simply a demonstration of this phenomenon is enough to assert that this configuration is well phase-matched in zero-index materials.

To conclude, in this chapter, we have successfully demonstrated phase matching in a FWM interaction for co-propagating pump and signal beams, for counter-propagating pump and signal beams, and for a signal beam coupling into the waveguide from outside the beam plane. In doing so, we have demonstrated phase matching for five separate configurations of the pump and signal beams. Combined, these results provide strong proof that zero-index materials exhibit an omnidirectional phase-matching condition.

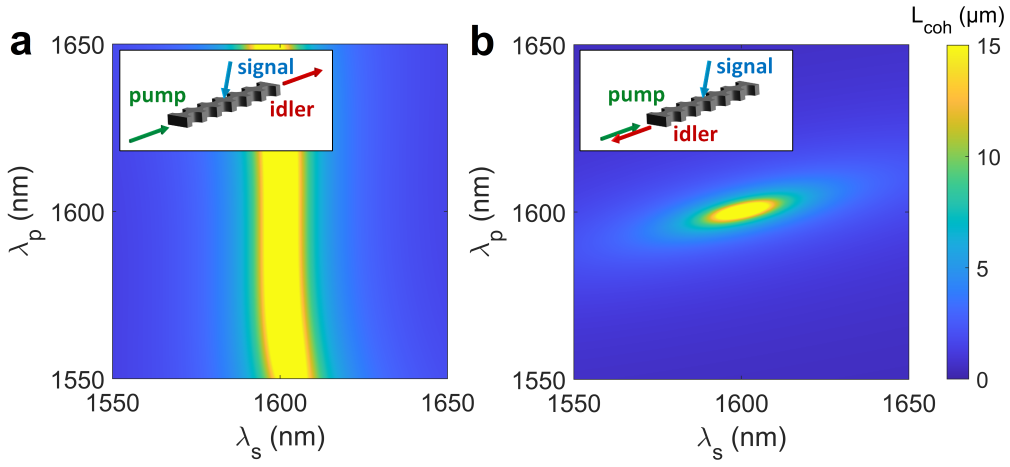

Figure 5.11 Predicted coherence lengths for an out-of-plane signal beam. Coherence length for an a) forward-propagating (relative to the pump beam) and b) backward-propagating idler wave. The phase-matching conditions are practically identical to those of Fig. 4.7. L_{coh} is plotted from 0 µm up to a maximum value of 15 µm.

Chapter Six
Conclusion

Nonlinear optics is a field that has had a wide variety of applications since its inception. Phase matching requirements are a fundamental constraint that limits the efficiency of all parametric nonlinear optical processes. To address this constraint, we utilized a Dirac-cone zero-index ridged silicon waveguide fabricated at Harvard University that is 14.8 µm in length. This waveguide functioned by using photonic crystals to achieve the simultaneous zero-crossing and the permittivity and permeability values. It exhibited a zero-index at a wavelength of 1600 nm and a near-zero-index region in the 100 nm range in the surrounding bandwidth. Before performing our experiment, we derived a model capable of predicting the generated idler wave power as a function of the pump and signal wavelengths for a given refractive index profile. For the refractive index profile of our zero-index waveguide, we observed that a FWM process is always phase-matched under some condition for all orientations of pump, signal, and idler waves. This constituted a theoretical demonstration of the existence of omnidirectional phase matching. To experimentally verify our theory, we investigated three different configurations of the pump and signal lasers when coupling into the waveguide: co-propagating, counter-propagating, and with an out-of-plane signal beam.

We realized our FWM interaction by using a strong pulsed laser as the pump laser, and a CW laser as our signal laser to seed the interaction. When the pump and signal beams were co-propagating, we observed forward- and backward-propagating idler waves. We furthermore verified that the relative powers of these idler waves were those predicted by our phase-matching theory. When the pump and signal beams were counter-propagating, we again showed that forward- and backward-propagating idler waves could be generated. We additionally demonstrated that phase matching could even occur with non-collinear beams by showing that a backward-generated idler wave could be generated from a signal beam coupling in from outside the beam plane, orthogonal to the pump beam. In total, five different configurations of the pump, signal, and idler waves were investigated. By sampling these five configurations of the pump, signal, and idler waves, we have therefore demonstrated sharply reduced dimensional restriction in a nonlinear optical interaction's components present when using a zero-index material (Fig. 6.1). Furthermore, by showing that one of the core restrictions in applying nonlinear optics may be thereby bypassed, our results in circumventing this restriction will facilitate nonlinear optics applications and make them more accessible to broader scientific research.

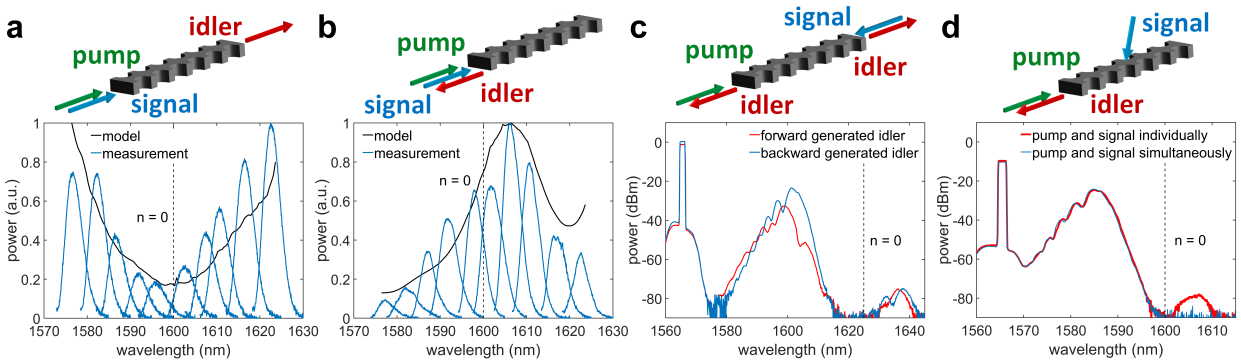

Figure 6.1 Most significant results presented in this thesis. Generated idler wave spectra in the a) forward and b) backward directions in a FWM process with co-propagating pump and signal beams, compared to theoretical predictions. c) Spectra showing FWM for counter-propagating pump and signal beams. An idler wave is simultaneously generated in the forward and backward directions. d) Generated idler wave spectrum obtained in the backward-propagating direction resulting from a signal beam coupling from outside the beam plane.

6.1 Scope for future work

For all of our experimental demonstrations of phase matching when using different beam orientations, the loss of the waveguide has posed some type of challenge. While in this thesis, we have made use of a waveguide operating above the light line, which has heavy intrinsic losses as a result, there have been two promising methods proposed to reduce such losses. The first method consists of using a special symmetry for the device such that the modes are unable to couple into free space [67, 68], while the second method consists of increasing the thickness of the waveguide such that a resonance occurs and escaping light interferes destructively with itself [67, 69]. While the current results are certainly already conclusive, with a lower-loss waveguide, experimental demonstrations of omnidirectional phase matching could be carried out more cleanly and could demonstrate our effect with even less ambiguity. To resolve the question posed of the out-of-plane measurement outlined in Section 5.6, an additional possibility would be to use a 3-dimensional photonic crystal featuring Dirac cones [70, 71]. In such a structure, there would be no doubt as to the origin of the generated idler wave. Assuming this particular structure was also lossless, it would also be able to show evidence of a forward-propagating idler wave.

Another potential improvement would be improving the spectrum of accessible wavelengths for strong pump and signal beams near the zero-index region. In this thesis, we have mostly investigated zero-index effects for pump and signal beams that lie below the zero-index region, due to limitations in the lasers being used. This was not of great consequence for the co-propagating measurement, which required that the idler wave be at the zero-index wavelength. However, in cases that required that the pump and signal beams be at the zero-index wavelength, this requirement was more difficult to satisfy. This was additionally compounded by the fact that the loss was highest in the zero-index region. The ability to more freely choose certain pump and signal wavelengths would allow us to further

demonstrate omnidirectional phase matching by generating an idler wave in the areas that are best phase-matched, as opposed to demonstrating omnidirectional phase matching by showing phase matching in the outskirts of that region.

The last potential improvement would be finding ways to increase the efficiency of the FWM processes observed in this experiment [72]. In this thesis, we strived and succeeded in executing a proof of concept. However, once we managed to generate an idler wave, we did not overly concern ourselves with trying to further improve the efficiency of our four-wave mixing processes. Achieving efficient omnidirectional phase matching in zero-index materials would greatly increase the applicability of our results. Reducing loss would be the first step in such an endeavor. Another possible way to increase the efficiency would be to use another material with a larger nonlinear response than silicon [65]. Here, we use silicon because it is easy to fabricate. However, our Dirac-cone waveguides can be constructed using any desired base material. The length of the waveguides could also be increased once loss is no longer a concern - in a longer waveguide, the generated idler wave could accrue over a longer length. We leave it up to future leaders in this field to discover more methods to increase the efficiency of these interactions.

Omnidirectional phase matching is an extremely interesting phenomenon that has the potential to make nonlinear optics more accessible and convenient in all research and applications where it is used. It also has the potential to increase the commercial viability of nonlinear optical interactions as a whole by allowing for the miniaturization of nonlinear optical devices, and due to this property could even be used for devices such as all-optical transistors [7, 8, 9]. We have seen how zero-index materials allow for this omnidirectional phase-matching condition, and we have explored the potential to facilitate the alignment and realization of all parametric nonlinear interactions. I look forward to seeing future work aimed at maximizing the efficiency and applicability of this exciting concept in the future, and laying the foundation for broad use of this exciting concept in both a laboratory setting and in industry.

APPENDIX

Appendix

Lower-bound estimate and MATLAB code

A.1 Lower-bound estimate on the coherence length

Here, we define the lower bound on the coherence length as the shortest length for which the factor $\mathrm{sinc}^2(L/L_{\mathrm{coh}})$ in Eq. (2.51) yields a pulse at a quarter of the peak power.

The solution to $\mathrm{sinc}^2(x) = 0.25$ is $x = 1.895$. Therefore, for a 14.8 µm waveguide, the lower bound on the coherence length is given by $L_{\mathrm{coh}} = 14.8$ µm / $1.895 = 7.81$ µm. If we instead use a lower power to define our lower bound, the lower bound on the coherence length is longer, while if we use a higher power to define our lower bound, the lower bound on the coherence length is shorter.

A.2 Code for omnidirectional phase matching

In this section we present the MATLAB code for generating plots for a large variety of angles. This code can be rather simply modified to only yield a coherence length plot for a specific set of angles by using the code located in the three for loops and setting the desired angles. Here, we make use of a .mat file containing refractive index data for the zero-index waveguide. While this file is not contained here, it can be substituted with any desired refractive index profile.

```
% Load the file containing the refractive index data
f1 = load('refractive_index.mat');

%% Calculate parameters

% Load refractive index data.
lambda = real(f1.n_retrieval.lambda);
n = real(squeeze(f1.n_retrieval.index));

% Keep only data between 1401 and 1751 nm.
lambda_min = 1399e-9;
lambda_max = 1751e-9;

% Generates a string of 1s and 0s specifying what to keep.
points_to_keep = logical((lambda >= lambda_min) .* (lambda <=
    lambda_max));
```

```
16
17 % Keeps the lambda, n values where points_to_keep is 1.
18 lambda = lambda(points_to_keep);
19 n = n(points_to_keep);
20
21 number_of_points = 1001; % Set how fine lambda_fine is.
22 lambda_fine = linspace(min(lambda), max(lambda), number_of_points)
       ;
23
24 % Fit n to a polynomial for lambda.
25 poly_order = 5; % Order of the polyfit polynomial
26 p = polyfit(lambda, n, poly_order);
27 n_poly = polyval(p, lambda_fine);
28
29 % Define lambda_p and lambda_s. Calculate resulting lambda_i.
30 lambda_p = linspace(1550, 1650, number_of_points)' * 1e-9; % 1001
       x 1 matrix
31 lambda_s = linspace(1550, 1650, number_of_points) * 1e-9; % 1 x
       1001 matrix
32 lambda_i = (2./lambda_p-1./lambda_s).^-1; % 1001 x 1001 matrix
33
34 % Find fitted refractive index of the pump, signal, and idler
       waves.
35 n_p = polyval(p, lambda_p);
36 n_s = polyval(p, lambda_s);
37 n_i = polyval(p, lambda_i);
38
39
40 %% Generate omnidirectional phase matching plots
41
42 % Determine how finely you want to probe the coherence length. f.x
       .
43 % angledivisions = 4 calculates at every pi / 2.
44 angledivisions = 4;
45 anglesize = pi/(angledivisions/2);
46
47 % Generate angledivisions^3 plots, for all angle combinations.
48 for k = 1:angledivisions
49
50     fig = figure;
51     set(fig,'DefaultLineLineWidth', 2, 'defaultAxesFontSize',7)
52     phi_i = (k-1)*anglesize;
53
54     for i = 1:angledivisions
```

```
55
56          theta_s = (i-1)*anglesize;
57
58          for j = 1:angledivisions
59
60              theta_i = (j-1)*anglesize;
61
62              kx = 2*pi*(2*n_p./lambda_p - n_s./lambda_s*cos(theta_s
                    ) - n_i./lambda_i*cos(theta_i)*cos(phi_i));
63              ky = 2*pi*(n_s./lambda_s*sin(theta_s) + n_i./lambda_i*
                    sin(theta_i)*cos(phi_i));
64              kz = 2*pi*n_i./lambda_i*sin(phi_i);
65
66              delta_k = sqrt(kx.^2+ky.^2+kz.^2);
67              L_coh = 2 ./ delta_k;
68
69              subplot(angledivisions, angledivisions, angledivisions
                    *(i-1) + j)
70              imagesc(lambda_s*10^9, lambda_p*10^9, L_coh * 10^6) %
                    Multiply L_coh so it's in um.
71              if j == angledivisions
72                  hcb = colorbar; % Only include a colorbar for the
                        furthest right graphs.
73                  title(hcb,'L_{coh} (\mum)')
74              end
75              caxis([0 15])
76              xlabel('\lambda_s (nm)')
77              xlim([1550 1650])
78              axis square
79              ylabel('\lambda_p (nm)')
80              ylim([1550 1650])
81              set(gca,'YDir','normal')
82
83          end
84      end
85  end
```

A.3 Generation of the theoretical predictions in Fig. 5.4

In this section we present the MATLAB code used to generate the theoretical predictions in Fig. 5.4. Here, we make use of two .mat files containing refractive index, permeability, and loss data respectively for the zero-index waveguide. While these files are not contained here, they can be substituted with any desired refractive index and loss profile. In this code, the

value of $\chi^{(3)}$ for silicon is obtained from [65] and the value of n for silicon is taken from [66].

```
% Load the file containing the refractive index and loss data
f1 = load('constitutive_parameters_a_734nm_r_224nm.mat');
F8 = load('loss.mat');

%% Parameters

% Load loss data
lambda_loss = F8.wavelength_save;
loss = F8.loss_save;

% Load refractive index data
lambda = real(f1.n_retrieval.lambda);
n = real(squeeze(f1.n_retrieval.index));

% Load permeability data
lambda_mu = real(f1.permeability.lambda);
mu = real(squeeze(f1.permeability.permeability));

% Find delta omega
pump_wl = 1600 * 10^-9; % m
signal_wl = 1580 * 10^-9; % m
c0 = 299792458; % m/s
deltaOmega = 2*pi*c0*((pump_wl - signal_wl)/(signal_wl*pump_wl));
    % rad/s

%% Iterate over some points:

lambda_p_number = 100;
lambda_start = 1557 * 10^-9; % m
lambda_end = 1603 * 10^-9; % m
L = 14.8 * 10^-6; % m
n_Si = 3.4757;
eps_zero = 8.854 * 10^-12; % F/m
X3 = 2.45 * 10^-19; % V^2/m^2

% Define pump, signal, and idler wavelengths
lambda_p = linspace(lambda_start, lambda_end, lambda_p_number); %
    1001 x 1 matrix
lambda_s = (2*pi*c0*lambda_p)./(2*pi*c0 + deltaOmega*lambda_p); %
    1001 x 1 matrix
lambda_i = (2*pi*c0*lambda_p)./(2*pi*c0 - deltaOmega*lambda_p); %
    1001 x 1 matrix

```

```
% Find refractive indices
n_p = interp1(lambda, n, lambda_p);
n_s = interp1(lambda, n, lambda_s);
n_i = interp1(lambda, n, lambda_i);

% Find loss values
a_p = 10^6 * log(10)* interp1(lambda_loss, loss, lambda_p) / 20;
a_s = 10^6 * log(10)* interp1(lambda_loss, loss, lambda_s) / 20;
a_i = 10^6 * log(10)* interp1(lambda_loss, loss, lambda_i) / 20;

% Define mu
mu_i = interp1(lambda_mu, mu, lambda_i);

% Calculate wave vectors
k_p = 2*pi*n_p ./ lambda_p;
k_s = 2*pi*n_s ./ lambda_s;
k_i = 2*pi*n_i ./ lambda_i;

% Calculate delta_k and delta_a
delta_k_fw = 2*k_p - k_s - k_i;
delta_k_bw = 2*k_p - k_s + k_i;
delta_a = 2*a_p + a_s;

% Calculate constants Omega
w_i = 2*pi*c0 ./ lambda_i;
Omega_fw = 3/2 * X3 * w_i .* mu_i ./ (n_i * c0);
Omega_bw = 3/2 * X3 * w_i .* exp(-(2*a_p + a_s)*L) .* mu_i ./ (n_i
    * c0);

% Calculate and normalize theoretical amplitude and power curves
idler_amp_fw = 1i * Omega_fw .* (exp((1i*delta_k_fw - delta_a)*L)
   - exp(-a_i*L)) ./ (1i * delta_k_fw + a_i - delta_a);
intensity_fw = 2 * n_Si * eps_zero * c0 * abs(idler_amp_fw).^2;

idler_amp_bw = 1i * Omega_bw .* (exp((-1i*delta_k_bw + delta_a)*L)
    - exp(-a_i*L)) ./ (-1i * delta_k_bw + a_i + delta_a);
intensity_bw = 2 * n_Si * eps_zero * c0 * abs(idler_amp_bw).^2;

% Define the figure, and plot the curves
fig = figure;
set(fig,'DefaultLineLineWidth', 3, 'defaultAxesFontSize', 40)

intensity_fw = intensity_fw / max(intensity_fw);
plot(10^9 * lambda_i, intensity_fw, 'red')
```

```
81 hold on
82
83 intensity_bw = intensity_bw / max(intensity_bw);
84 plot(10^9 * lambda_i, intensity_bw, 'black')
85
86 % Draw the zero-index line
87 line(linspace(1600,1600,100),linspace(0,1,100),'LineWidth',2,'
       Color','black','LineStyle','--');
88
89 % Format table
90 xlim([1570 1630])
91 ylim([0 1])
92 xlabel('wavelength (nm)')
93 ylabel('power (a.u.)')
94 pbaspect([360 270 1])
95 box = gca;
96 box.LineWidth = 2;
97 legend('Forward-propagating','Backward-propagating','FontSize',40)
       ;
```

References

[1] Justin R. Gagnon et al. *Relaxed phase-matching constraints in zero-index waveguides*. 2021.

[2] T.H. Maiman. "Stimulated Optical Radiation in Ruby". In: *Nature* 187.4736 (Aug. 1960), pp. 493–494.

[3] Elsa Garmire. "Nonlinear optics in daily life". In: *Opt. Express* 21.25 (Dec. 2013), pp. 30532–30544.

[4] Alan E. Willner et al. "All-Optical Signal Processing". In: *J. Lightwave Technol.* 32.4 (Feb. 2014), pp. 660–680.

[5] Shaul Mukamel. *Principles of Nonlinear Optical Spectroscopy*. New York City, NY: Oxford University Press, 1999.

[6] Lothar Schermelleh, Rainer Heintzmann, and Heinrich Leonhardt. "A guide to super-resolution fluorescence microscopy". In: *Journal of Cell Biology* 190.2 (July 2010), pp. 165–175. ISSN: 0021-9525.

[7] M. Asobe, T. Kanamori, and K. Kubodera. "Ultrafast all-optical switching using highly nonlinear chalcogenide glass fiber". In: *IEEE Photonics Technology Letters* 4.4 (1992), pp. 362–365.

[8] Vilson R. Almeida et al. "All-optical control of light on a silicon chip". In: *Nature* 431 (Oct. 2004), pp. 1081–1084.

[9] D. Cotter et al. "Nonlinear Optics for High-Speed Digital Information Processing". In: *Science* 286.5444 (1999), pp. 1523–1528. ISSN: 00368075, 10959203.

[10] J. A. Armstrong et al. "Interactions between Light Waves in a Nonlinear Dielectric". In: *Phys. Rev.* 127 (6 Sept. 1962), pp. 1918–1939.

[11] M. Yamada et al. "First-order quasi-phase matched LiNbO3 waveguide periodically poled by applying an external field for efficient blue second-harmonic generation". In: *Applied Physics Letters* 62 (1993), pp. 435–436.

[12] J E Midwinter and J Warner. "The effects of phase matching method and of uniaxial crystal symmetry on the polar distribution of second-order non-linear optical polarization". In: *British Journal of Applied Physics* 16.8 (Aug. 1965), pp. 1135–1142.

[13] Christopher C. Evans et al. "Multimode phase-matched third-harmonic generation in sub-micrometer-wide anatase TiO2 waveguides". In: *Opt. Express* 23.6 (Mar. 2015), pp. 7832–7841.

[14] Michael G. Moebius et al. "Efficient photon triplet generation in integrated nanophotonic waveguides". In: *Opt. Express* 24.9 (May 2016), pp. 9932–9954.

[15] Haim Suchowski et al. "Phase mismatch-free nonlinear propagation in optical zero-index materials". In: *Science* 342 (Dec. 2013), pp. 1223–1226.

[16] Shoufeng Lan et al. "Backward phase-matching for nonlinear optical generation in negative-index materials". In: *Nature Mater.* 14.8 (June 2015), pp. 807–811.

[17] Liangliang Liu et al. "Backward Phase Matching for Second Harmonic Generation in Negative-Index Conformal Surface Plasmonic Metamaterials". In: *Advanced Science* 5.11 (Aug. 2018), p. 1800661.

[18] Ilya V. Shadrivov, Alexander A. Zharov, and Yuri S. Kivshar. "Second-harmonic generation in nonlinear left-handed metamaterials". In: *J. Opt. Soc. Am. B* 23.3 (Mar. 2006), pp. 529–534.

[19] A. Popov and Vladimir Shalaev. "Negative-Index Metamaterials: Second-Harmonic Generation, Manley-Rowe Relations and Parametric Amplification". In: *Applied Physics B* 84 (Jan. 2006).

[20] M. Kauranen and A. Zayats. "Nonlinear plasmonics". In: *Nat. Photonics* 6 (2012), pp. 737–748.

[21] Orad Reshef et al. "Direct observation of phase-free propagation in a silicon waveguide". In: *ACS Photonics* 4.6163 (Oct. 2017), pp. 2385–2389.

[22] Nathaniel Kinsey et al. "Near-zero-index materials for photonics". In: *Nat. Rev. Mat.* 4.12 (Dec. 2019), pp. 742–760.

[23] Robert W. Boyd. *Nonlinear Optics*. 4th ed. San Diego, California: Academic Press, 2020.

[24] Yuen R. Shen. *The Principles of Nonlinear Optics*. 1st ed. New York City, NY: Wiley-Interscience, 2002.

[25] P. A. Franken et al. "Generation of Optical Harmonics". In: *Phys. Rev. Lett.* 7 (4 Aug. 1961), pp. 118–119.

[26] R.W. Boyd. "Near-zero-index materials for photonics". In: *J. Mod. Opt.* 46.3 (July 1999), pp. 367–378.

[27] Mark A. Foster et al. "Broad-band optical parametric gain on a silicon photonic chip". In: *Nature* 441.7096 (2006), pp. 960–963.

[28] R. L. Carman, R. Y. Chiao, and P. L. Kelley. "Observation of Degenerate Stimulated Four-Photon Interaction and Four-Wave Parametric Amplification". In: *Phys. Rev. Lett.* 17 (26 Dec. 1966), pp. 1281–1283.

[29] R. Stolen and J. Bjorkholm. "Parametric amplification and frequency conversion in optical fibers". In: *IEEE Journal of Quantum Electronics* 18.7 (July 1982), pp. 1062–1072.

[30] Hiroki Takesue and Kyo Inoue. "Generation of polarization-entangled photon pairs and violation of Bell's inequality using spontaneous four-wave mixing in a fiber loop". In: *Phys. Rev. A* 70 (3 Sept. 2004), p. 031802.

[31] Kai-Hong Luo et al. "Counter-propagating photon pair generation in a nonlinear waveguide". In: *Opt. Express* 28.3 (Feb. 2020), pp. 3215–3225.

[32] F. Arecchi and R. Bonifacio. "Theory of optical maser amplifiers". In: *IEEE Journal of Quantum Electronics* 1.4 (1965), pp. 169–178.

[33] Nadia Mattiucci et al. "Coherence length for second-harmonic generation in nonlinear, one-dimensional, finite, multilayered structures". In: *J. Opt. Soc. Am. B* 24.4 (May 2007), pp. 877–886.

[34] R. A. Shelby, D. R. Smith, and S. Schultz. "Experimental Verification of a Negative Index of Refraction". In: *Science* 292.5514 (2001), pp. 77–79.

[35] Mark Stockman. "Does Nature Allow Negative Refraction with Low Losses in Optical Region?" In: (Dec. 2006), pp. 1–4.

[36] Jason Valentine et al. "Three-dimensional optical metamaterial with a negative refractive index". In: *Nature* 455.7211 (Sept. 2008), pp. 376–379.

[37] Henri J. Lezec, Jennifer A. Dionne, and Harry A. Atwater. "Negative Refraction at Visible Frequencies". In: *Science* 316.5823 (2007), pp. 430–432. ISSN: 0036-8075.

[38] J. B. Pendry et al. "Extremely Low Frequency Plasmons in Metallic Mesostructures". In: *Phys. Rev. Lett.* 76 (25 June 1996), pp. 4773–4776.

[39] Gururaj V. Naik, Jongbum Kim, and Alexandra Boltasseva. "Oxides and nitrides as alternative plasmonic materials in the optical range". In: *Opt. Mater. Express* 1.6 (Oct. 2011), pp. 1090–1099.

[40] Iñigo Liberal and Nader Engheta. "Near-zero refractive index photonics". In: *Nature* 11.3 (Mar. 2017), pp. 149–158.

[41] Mário Silveirinha and Nader Engheta. "Tunneling of Electromagnetic Energy through Subwavelength Channels and Bends using ϵ-Near-Zero Materials". In: *Phys. Rev. Lett.* 97 (15 Oct. 2006), p. 157403.

[42] Giuseppe D'Aguanno et al. "Field localization and enhancement near the Dirac point of a finite defectless photonic crystal". In: *Phys. Rev. B* 87 (8 Feb. 2013), p. 085135.

[43] Mohammad H. Javani and Mark I. Stockman. "Real and Imaginary Properties of Epsilon-Near-Zero Materials". In: *Phys. Rev. Lett.* 117 (10 Sept. 2016), p. 107404.

[44] Philip Camayd-Muñoz et al. "Long-range phase-free propagation in a dielectric metasurface". In: *Conference on Lasers and Electro-Optics*. Optical Society of America, 2017, JTu5A.39.

[45] Daryl I Vulis et al. "Manipulating the flow of light using Dirac-cone zero-index metamaterials". In: *Rep. Prog. Phys.* 82.1 (Nov. 2018), p. 012001.

[46] Orad Reshef et al. "Phase-Matching in Dirac-Cone-Based Zero-Index Metamaterials". In: *Conference on Lasers and Electro-Optics*. Optical Society of America, 2016.

[47] Orad Reshef et al. "Nonlinear optical effects in epsilon-near-zero media". In: *Nat. Rev. Mat.* 4 (8 2019), pp. 535–551.

[48] M. Zahirul Alam, Israel De Leon, and Robert W. Boyd. "Large optical nonlinearity of indium tin oxide in its epsilon-near-zero region". In: *Science* 352.6287 (May 2016), pp. 795–797.

[49] Sisira Suresh et al. "Enhanced Nonlinear Optical Responses of Layered Epsilon-Near-Zero Metamaterials at Visible Frequencies". In: (May 2020).

[50] M. Mazilu and K. Dholakia. "Optical impedance of metallic nano-structures". In: *Opt. Express* 14.17 (Sept. 2006), pp. 7709–7722.

[51] Xueqin Huang et al. "Dirac cones induced by accidental degeneracy in photonic crystals and zero-refractive-index materials". In: *Nature Materials* 10 (8 Aug. 2011).

[52] Parikshit Moitra et al. "Realization of an all-dielectric zero-index optical metamaterial". In: *Nat. Photonics* 7.10 (Oct. 2013), pp. 791–795.

[53] C. Enkrich et al. "Magnetic Metamaterials at Telecommunication and Visible Frequencies". In: *Phys. Rev. Lett.* 95 (20 Nov. 2005), p. 203901.

[54] John D. Joannopoulos et al. *Photonic crystals — Molding the Flow of Light*. 2nd ed. Princeton, New Jersey: Princeton University Press, 2007.

[55] Sajeev John. "Strong localization of photons in certain disordered dielectric superlattices". In: *Phys. Rev. Lett.* 58 (23 June 1987), pp. 2486–2489.

[56] Eli Yablonovitch. "Inhibited Spontaneous Emission in Solid-State Physics and Electronics". In: *Phys. Rev. Lett.* 58 (20 May 1987), pp. 2059–2062.

[57] Kazuaki Sakoda. "Universality of mode symmetries in creating photonic Dirac cones". In: *J. Opt. Soc. Am. B* 29.10 (Oct. 2012), pp. 2770–2778.

[58] Kazuaki Sakoda. "Dirac cone in two- and three-dimensional metamaterials". In: *Opt. Express* 20.4 (Feb. 2012), pp. 3898–3917.

[59] Shota Kita et al. "On-chip all-dielectric fabrication-tolerant zero-index metamaterials". In: *Opt. Express* 25.7 (Apr. 2017), pp. 8326–8334.

[60] Ying Wu et al. "Effective medium theory for magnetodielectric composites: Beyond the long-wavelength limit". In: *Phys. Rev. B* 74 (8 Sept. 2006), p. 085111.

[61] Orad Reshef. "Integrated metamaterials and nanophotonics in CMOS-compatible materials". PhD thesis. Harvard University, Aug. 2016.

[62] Daryl I. Vulis et al. "Monolithic CMOS-compatible zero-index metamaterials". In: *Opt. Express* 25.11 (May 2017), pp. 12381–12399.

[63] Govind P. Agrawal. *Nonlinear Fiber Optics*. 4th ed. Boston, MA: Academic Press, 2007.

[64] P. F. Moulton. "Spectroscopic and laser characteristics of Ti:Al2O3". In: *J. Opt. Soc. Am. B* 3.1 (Jan. 1986), pp. 125–133.

[65] N. K. Hon, R. Soref, and B. Jalali. "The third-order nonlinear optical coefficients of Si, Ge, and Si1-xGex in the midwave and longwave infrared". In: *Journal of Applied Physics* 110 (2011), p. 011301.

[66] H. H. Li. "Refractive index of silicon and germanium and its wavelength and temperature derivatives". In: *Journal of Physical and Chemical Reference Data* 9.3 (1980), pp. 561–658.

[67] Tian Dong et al. "Ultra-low-loss on-chip zero-index materials". In: *Light: Science and Applications* 10 (1 2021).

[68] Momchil Minkov et al. "Zero-Index Bound States in the Continuum". In: *Phys. Rev. Lett.* 121 (26 Dec. 2018), p. 263901.

[69] Haoning Tang et al. "Low-Loss Zero-Index Materials". In: *Nano Lett.* 21 (2 2021).

[70] Xueqin Huang, Fengming Liu, and C. T. Chan. *Three dimensional Dirac point at k=0 in photonic and phononic systems*. 2012.

[71] Jorge Bravo-Abad, John D. Joannopoulos, and Marin Soljacic. "Enabling single-mode behavior over large areas with photonic Dirac cones". In: *Proceedings of the National Academy of Sciences* 109.25 (2012), pp. 9761–9765. ISSN: 0027-8424.

[72] Minhao Pu et al. "Ultra-Efficient and Broadband Nonlinear AlGaAs-on-Insulator Chip for Low-Power Optical Signal Processing". In: *Laser and Photonics Reviews* 12.12 (2018). ISSN: 1863-8880.